CHARACTERIZATION OF WALL SHEAR STRESS IN ABDOMINAL AORTIC ANEURYSM PHANTOM USING PARTICLE IMAGE VELOCIMETRY

A THESIS SUBMITTED TO
THE GRADUATE SCHOOL OF NATURAL AND APPLIED SCIENCES
OF
MIDDLE EAST TECHNICAL UNIVERSITY

BY

SEMİH TÜRK

IN PARTIAL FULFILLMENT OF THE REQUIREMENTS
FOR
THE DEGREE OF MASTER OF SCIENCE
IN
MECHANICAL ENGINEERING

SEPTEMBER 2021

Approval of the thesis:

CHARACTERIZATION OF WALL SHEAR STRESS IN ABDOMINAL AORTIC ANEURYSM PHANTOM USING PARTICLE IMAGE VELOCIMETRY

submitted by **SEMİH TÜRK** in partial fulfillment of the requirements for the degree of **Master of Science in Mechanical Engineering, Middle East Technical University** by,

Prof. Dr. Halil Kalıpçılar
Dean, Graduate School of **Natural and Applied Sciences**   _____

Prof. Dr. M. A. Sahir Arıkan
Head of the Department, **Mechanical Engineering**   _____

Prof. Dr. M. Metin Yavuz
Supervisor, **Mechanical Engineering, METU**   _____

Examining Committee Members:

Assoc. Prof. Dr. Cüneyt Sert
Mechanical Eng., METU   _____

Prof. Dr. M. Metin Yavuz
Mechanical Eng., METU   _____

Assist. Prof. Dr. Ö. Uğraş Baran
Mechanical Eng., METU   _____

Assist. Prof. Dr. Ali Karakuş
Mechanical Eng., METU   _____

Prof. Dr. Murat Kadri Aktaş
Mechanical Eng., TOBB ETU   _____

Date: 01.09.2021

I hereby declare that all information in this document has been obtained and presented in accordance with academic rules and ethical conduct. I also declare that, as required by these rules and conduct, I have fully cited and referenced all material and results that are not original to this work.

Name Last name : Semih Türk

Signature :

ABSTRACT

CHARACTERIZATION OF WALL SHEAR STRESS IN ABDOMINAL AORTIC ANEURYSM PHANTOM USING PARTICLE IMAGE VELOCIMETRY

Türk, Semih
Master of Science, Mechanical Engineering
Supervisor: Prof. M. Metin Yavuz

September 2021, 120 pages

Abdominal Aortic Aneurysm (AAA) is defined as the enlargement of the largest artery in the abdominal cavity, the abdominal aorta. The vascular rupture begins to pose a risk after a certain enlargement, and the rupture is described as one of the most critical emergencies in medicine. The disease is labeled as the 14th disease with the highest mortality rate. Thus, predicting the progression of the disease is vitally important. Hence, researchers are trying to identify and standardize all biological and mechanical factors on growth and rupture. Wall shear stress and the wall shear stress metrics have a significant impact on vascular dilation and rupture. Recently, researches focused on understanding the relationship between the wall shear stress and the rupture correlated occurrences such as calcification and fat deposits with numerical and experimental studies. Due to the difficulties encountered with the near-wall measurements in experimental methods, most studies are conducted by numerical methods.

The present study aims to characterize the flow structure in abdominal aortic aneurysm and analyze the distribution of the wall shear stress of the AAA by using Particle Image Velocimetry (PIV.) The study compares the accuracy of PIV data in

terms of proximity to the wall and velocity profile fits in terms of WSS prediction. For that purpose, simple and axisymmetric aneurysm geometry and Newtonian blood mimicking fluid are used. The experiments are conducted in two steady (Re =300 and Re=900) and one physiological (Re$_{mean}$ ≈ 300 and α=7.17) case. Close-up studies are conducted in order to see the effect of spatial resolution increase for the steady cases.

The results indicate that the first PIV data closest to the wall overestimates the velocities for the whole field experiment approach. On the other hand, close-up studies overestimate multiple data point closest to the wall. However, results of close-up studies are obtained by using closer data points to the wall compared to the whole field since the spatial resolution of the close-up approach is more superior than the whole field. For obtaining accurate WSS estimation, different near-wall profiles are investigated, such as second-order polynomial, third order polynomial, cubic spline, etc. 3rd order polynomial and cubic spline fits are the two methods that give expected results. Using cubic spline fits for the wall shear stress calculation is convenient since the spline fit method gives robust results in the case of complex flows. Regions with low wall shear stress and high oscillatory shear index are considered hazardous for growth and rupture. For the current aneurysm model, this combination and high risk are observed at distal/proximal edges and regions with secondary vortices in case of physiological flow.

Keywords: Abdominal Aortic Aneurysm, Wall Shear Stress, Blood Flow, Hemodynamics, Particle Image Velocimetry

ÖZ

ABDOMİNAL AORT ANEVRİZMA MODELİNDE DUVAR KESME GERİLİMİNİN PARTİKÜL GÖRÜNTÜ VELOSİMETRİSİ KULLANILARAK KARAKTERİZASYONU

Türk, Semih
Yüksek Lisans, Makina Mühendisliği
Tez Yöneticisi: Prof. Dr. M. Metin Yavuz

Eylül 2021, 120 sayfa

Abdominal Aort Anevrizması (AAA), karın boşluğundaki en büyük arter olan abdominal aortun genişlemesi olarak tanımlanır. Bir miktar genişlemeden sonra damar, tıpta en kritik vakalardan biri olarak tanımlanan yırtılma riskini taşır. Ayrıca, hastalık, en yüksek 14. ölüm oranına sahip olan hastalık olarak belirlenmiştir. Bu nedenle, hastalığın ilerleyişini tahmin etmek hasta için hayati önem taşımaktadır.

Bu alanda yapılan araştırmalar damarın genişlemesi ve yırtılması üzerindeki tüm biyolojik ve mekanik faktörleri tanımlamaya ve standartlaştırmaya çalışmaktadır. Duvar kesme gerilimi ve onunla ilgili metrikler, damar genişlemesi ve yırtılması üzerinde etkin bir faktör olarak öne çıkmaktadır. Son zamanlardaki araştırmalar, nümerik ve deneysel methodlar kullanarak duvar kesme gerilmesi ile kireçlenme ve yağ birikintileri gibi yırtılmayla bağlantılı olaylar arasındaki ilişkiyi anlamaya odaklanmıştır. Ancak deneysel yöntemlerde duvara yakın ölçüm alınırken karşılaşılan zorluklar nedeniyle çalışmaların çoğu nümerik methodla yürütülmüştür.

Bu çalışma, Partikül Görüntü Velosimetrisi (PIV) kullanarak abdominal aort anevrizmasının içindeki akışkan mekanizmasını araştırmayı ve duvar kesme geriliminin bir dağılımını çıkarmayı amaçlamaktadır. Ek olarak, duvara yakınlıklarının PIV verilerini nasıl etkilediği ve hangi hız profil modelinin doğru kesme gerilim sonucu verdiği gözlenmektedir. Deneyde teorik ve eksenel simetrik

anevrizma geometrisi ve Newton tipi akışkan sıvı kullanılmıştır. Deneyler iki stabil (Re=300 ve Re=900) ve bir fizyolojik (Reort ≈ 300 ve α=7.17) akış tipi kullanılarak gerçekleştirilmiştir. Ayrıca durağan durumlar için uzamsal çözünürlük artışının etkisini görmek için yakın çekim çalışmaları yapılmıştır.

Sonuçlar, genellikle duvara en yakın olan ilk PIV verilerinin, duvara yakın hızları olduğundan yüksek tahmin ettiğini göstermektedir. Bu nedenle, duvara en yakın veri noktası yerine yakındaki diğer verilerin kullanılması daha güvenilir sonuçlar vermiştir. Duvar kesme gerilimi hesaplamasında duvara yakın verilerin elenmesini telafi edebildiği için ve kompleks akış yapılarında daha stabil sonuç verdiği için, kübik "spline" fit (4 noktalı) kullanılmıştır. Artan Reynolds sayısının damarın proksimal ve distal uçlarında hemodinamik instabiliteye sebep olabileceği gözlenmiştir. Düşük duvar kesme gerilimi ve yüksek salınımlı kesme indeksinin beraber görüldüğü bölgelerde genişleme yırtılma riski çok yüksektir. Bu çalışmada fizyolojik akış kullanıldığında damarın proksimal ve distal uçlarında, ve bunlara ek olarak ikincil girdapların görüldüğü yerlerde bu risklerin yüksek olduğu sonucuna varılmıştır.

Anahtar Kelimeler: Abdominal Aort Anevrizması, Duvar Kesme Gerilimi, Kan Akışı, Hemodinamik, Partikül Görüntü Velosimetrisi

To my family and my love

ACKNOWLEDGMENTS

First of all, I would like to express my special appreciation to my thesis supervisor, Prof. M. Metin Yavuz, for his support and guidance. I am grateful to him for including me in his research group, and I am honored to be a part of the group.

I would like to thank my family for their invaluable support not only for my thesis work but also throughout my life. My sincere thanks go to my life partner Ekin Okumuş. Like my family, for being in my life and her priceless support during the thesis process. In addition, I am grateful to Emin Alp Uyanık for his friendship and support during my thesis study.

I would like to thank my friends Kerem Tuğ Gökçek, Oğuzhan Yılmaz, Amirhossein Fathipour, Burcu Ramazanlı, Osman Ohtaroğlu, Cenk Çetin, Göktuğ Koçak in our lab group and also a former member Kayacan Kestel for sharing their experiences and friendships.

Lastly, I want to thank Mr. Mehmet Özçiftçi for his technical assistance.

TABLE OF CONTENTS

LIST OF TABLES

LIST OF FIGURES

FIGURES

LIST OF ABBREVIATIONS

ABBREVIATIONS

CMOS   : Complementary Metal Oxide Semiconductor

AAA   : Abdominal Aortic Aneurysm

PIV   : Particle Image Velocimetry

LDA   : Laser Doppler Anemometry

WSS   : Wall Shear Stress

TAWSS   : Time Average Wall Shear Stress

WSSG   : Wall Shear Stress Gradient

TAWSSG   : Time Average Wall Shear Stress Gradient

OSI   : Oscillatory Shear Index

TWSSG   : Temporal Wall Shear Stress Gradient

RI   : Refractive Index

PDMS   : Polydimethylsiloxane

LIST OF SYMBOLS

SYMBOLS

Re   : Reynolds number

Re_{mean} : Mean of the Reynolds number

α : Womersley number

μ : Dynamic Viscosity (Pa.s)

v : Kinematic viscosity (m^2/s)

ρ : Density of fluid (kg/m^3)

ω : Vorticity (1/s)

Δt : Time difference between the two successive PIV images (s)

CHAPTER 1

INTRODUCTION

Two main components exist in the human blood circulatory system: the heart and the blood vessel. Arteries are the vessel types that carry blood away from the heart. Aorta is the biggest artery in the human circulatory system with a standard diameter of around 2 – 3 cm and is located in the abdominal cavity. When the diameter of the abdominal aorta increases for a particular section, it is defined as a disease called Abdominal Aortic Aneurysm (AAA), as presented in Figure 1.1.
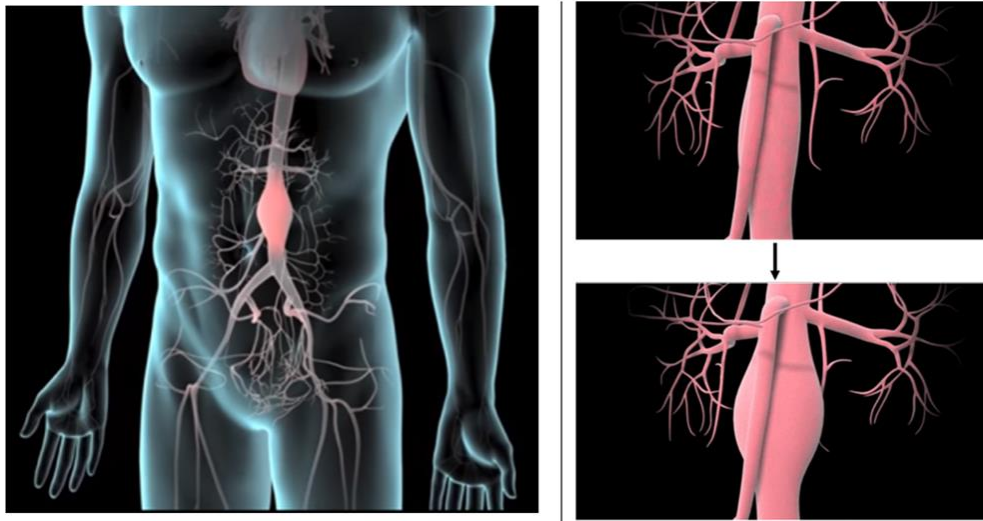
Figure 1.1: Abdominal Aortic Aneurysm (AAA) presentation

AAA disease is called the 14th disease that results in death; its occurrence is around 2-3% of the whole population [1]. AAA initiation reason is not certain, but some reported correlations exist like family background, old age, gender, etc. In particular, smoking is highly correlated with AAA disease. Only 15 % of the AAA disease

patients do not relate to smoking; that indicates a strong correlation [2]. The most dangerous part of the disease is being asymptomatic, which means that the patient cannot feel any pain or discomfort until it ruptures. Still, symptoms exist, such as pain in the back and abdomen, tenderness in the related area, weight loss, and elevated erythrocyte sedimentation rate. AAA that comes with the pain is highly risky for rupture. The ratios of the clinical findings observed in patients with the ruptured vessel are provided by the chart in Figure 1.2.

Sign and Symphoms Ratios of Patients with Ruptured AAA (413 Patients)
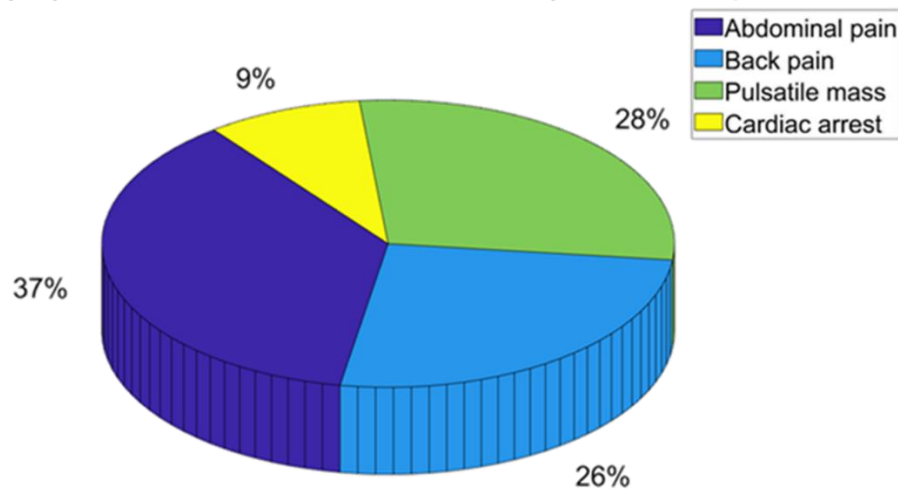
Figure 1.2: Sign and symptom ratios of patients with ruptured AAA (413 Patients) [3]

AAA mortality rate is around 78 – 94 % when it ruptures. AAA rupture is classified as one of the most critical emergencies in medicine [4]. Rupture is related to the diameter, but it is not the only correlation for this occasion. For example, not only the diameter but also the diameter growth rate is essential to predict the rupture. Also, it is reported that rupture risk is higher on average for hypertension patients [5]. Thus, vessel diameter, growth rate, mechanical conditions of the vessel, etc., should be considered as a whole. AAA can be repaired in two ways: endovascular repair and open surgical repair, the oldest method. There are advantages and disadvantages for both methods, yet none of the two methods is not superior to the other. Open repair is a more invasive method than the endovascular. For open surgery, blood loss and

post-processive pain are more than the endovascular. On the other hand, endovascular surgery is advantageous in the short term and for risky patients (old age, diabetic patients, etc.) Recrudescence seems more rarely in open surgery, but it should be noted that it becomes hard to track follow-ups for the long term. Considering all these factors, it is hard to decide which method is best for the patient. Vessel structure is of great importance in AAA disease. There are three main layers in the healthy abdominal aorta: tunica intima, tunica media, and adventitia [6]. In the case of the disease, these layers become disorganized, and as a result, wall stiffness increases with decreasing compliance and distensibility. Also, AAA disease and rupture correlated with calcification and fat deposits.

Conditions such as vortex structures in the aneurysm, pressure, and wall shear stress affect the rupture and the progression of the disease. As mentioned above, the risk of rupture is higher in patients with hypertension because the pressure on the wall is above normal. However, the most critical factor in rupture is wall shear stress because abnormal WSS disrupts the structure of the vessel, which leads to rupture physically. Wall shear stress results from the internal fluid characteristics inside the aneurysm, so the internal flow structure must be investigated to understand the WSS dynamics correctly. In addition, abnormal stress, caused by conditions such as calcification and fat deposits, also causes the progression of this disease. Not only the magnitude of the WSS but also the created metrics like Wall Shear Stress Gradient (WSSG), Oscillatory Shear Index (OSI), and Temporal Wall Shear Stress Gradient (TWSSG) are crucial to understand the progression of the disease. For example, sites with high OSI and low WSS are correlated with atherosclerotic plaque formation, and intimal hyperplasia or TWSS causes endothelial cell proliferation, as a result, disrupts vessel structure [7],[8]. All of these formations are important in understanding and predicting the rupture. Since these mechanisms are directly affected by blood flow inside the vessel, the characteristics of blood are essential. Blood shows non-newtonian behavior and, more specifically, shear-thinning characteristics due to the deformable behavior of the red blood cells inside the blood.

3

In other words, as the shear rate increases, the viscosity of the blood decreases. The shear rate - blood's viscosity relation is significant in small diameter vessels. When factors like the complex geometry of the aneurysm, the physiological pattern of the heart, the aforementioned features of the blood, and the compliance structure of the vessel are evaluated, it turns into a mechanism that is difficult to understand.

1.1 Motivation of the Study

Abdominal aortic aneurysm rupture is a disease with a high mortality rate. Predicting the time and probability of rupture is a crucial development that directly affects human life. For this reason, the physics of fluids affecting these biological structures is as essential as the biological factors related to the vascular structure.

Wall shear stress is of significant impact on the rupture of the Abdominal Aortic Aneurysm. In order to interpret the wall shear stress characteristic correctly, it is necessary to understand the internal flow characteristics. There are a number of studies, both experimental and numerical, examining the flow fields in the Abdominal Aortic Aneurysm. Still, especially the studies on wall shear stress are numeric rather than experimental. Most studies are numeric-based; because near-wall measurements have difficulties considering spatial resolution and optical constraints, including reflection and refraction during the experimental studies. There are also other obstacles exist that may be inherent in the experimental method. For this reason, experimental reporting is essential for wall shear stress measurement.

1.2 Aim of the Study

The aim of this study is to experimentally examine the simple and axisymmetric abdominal aortic aneurysm geometry in terms of both flow physics and wall shear stress characteristics. The primary purpose is to develop a method for WSS

calculation by using PIV. With this, correlate the regions in the aneurysm with biological occurrences considering both the WSS and the WSS-related parameters.

For this experimental study, Particle Image Velocimetry equipment is used mainly to extract the velocity field distribution, together with supporting equipment such as pressure transducer and flowmeter. Steady and physiological patterns are examined with both whole field and close-up studies. Different WSS prediction methods are developed and compared with known analytical WSS results for the circular pipe and results from the literature for the bulge portion. The methods include different velocity profiles and different initial data points. The comparison is also supported with close-up and whole field discussions. Reporting the measurement process is as important as the wall shear stress output in the experiment because experimental studies on PIV wall shear stress are few compared to numeric studies [9], [10]. Since wall shear stress output is not as accessible as in the CFD post-process of the experimental data, it is necessary to calculate wall shear stress from PIV velocity output. A MATLAB code is written and implemented to calculate WSS. It also has the advantage of gaining the freedom to try different velocity fit models for wall shear stress calculation in situations where non-biased data cannot be obtained near the wall.

This study determines which parameters (vel fit profile, wall location determination, etc.) give the best results and reports the abdominal aortic aneurysm WSS measurement process with PIV equipment. Moreover, the study documents how the WSS and WSS metric distribution is connected with the general flow field. The study also aims to predict the biological occurrences such as endothelial cell proliferation and localization of atherosclerotic that may occur with the WSS distribution.

1.3   The outline of the Thesis

The thesis consists of five main chapters.

Chapter one provides introductory information about the abdominal aortic aneurysm and clearly states the motivation and aim of the study.

Chapter two is composed of a detailed literature survey on the abdominal aortic aneurysm on a medical basis. Furthermore, the studies in the literature on the experimental set-up and obtained results are briefly summarized.

Chapter three presents the experimental set-up, including each experimental component such as blood mimicking fluid, phantom, etc. Moreover, details of the measurement techniques and data processing tools are discussed.

The fourth chapter is composed of a discussion on the finding, WSS distributions, and the WSS parameters for steady and physiological patterns together with the determined methodology for WSS measurement.

Chapter five provides a detailed summary of the conclusions, including recommendations for future work.

CHAPTER 2

LITERATURE REVIEW

The following chapter summarizes the studies in the literature regarding the Abdominal Aortic Aneurysm (AAA), Wall Shear Stress (WSS), and related studies comprehensively.

2.1 Abdominal Aortic Aneurysm (AAA)

The distribution of blood, nutrients, oxygen and other gases and hormones to and from the cells are the functions of the circulatory system. Two primary components function together in the circulatory system: the heart and the blood vessels [11].

The heart is located in the middle of the thoracic cavity, and it lies on the diaphragm. Its size can be roughly described as the size of a closed fist [12]. The heart is the running power source of the circulatory system, which acts as a pump for blood circulation in the vessels. This pump behavior can be considered as two different pump actions. One of which is pulmonary circulation, and the other is systemic circulation. Blood flow to the lungs in order to exchange gases between blood and the alveoli for cleaning the blood in terms of oxygen content is called the pulmonary circulation. Blood circulation, which contains all blood vessels, including inside and outside the organs except the lung, is called systemic circulation. A schematic of those circulations can be seen in Figure 2.1.
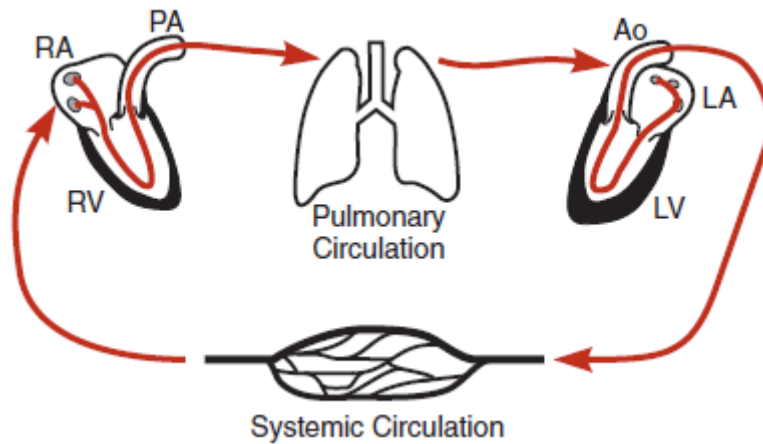
Figure 2.1: Schematic presentation of systemic circulation system [11]

The arteries, arterioles, capillaries, venules, and veins are the five primary blood vessels. Arteries carry blood from the heart to the other organs; on the contrary, veins return blood to the heart. Arterioles and venules are the smaller sizes of those arteries and veins that branch into various body parts. Capillaries are the final and smallest branches of the circulation system whose diameters are around $5 - 10$ μm [13]. Capillaries spread throughout the tissues, and their thin walls permit the interchanging of blood and body tissues. Aorta is the biggest artery of the human circulation system, with an inner diameter of $2 - 3$ cm. Its four main segments are ascending aorta, arch of the aorta, thoracic aorta, and abdominal aorta [12]. An abdominal aortic aneurysm is a disease in which the aorta vessel weakens. As a result, its diameter enlarges for a particular section; therefore, a bulge shape is formed in the abdominal aorta, shown in Figure 2.2. This condition is considered a disease because it has a number of symptoms and consequences that progress to death.
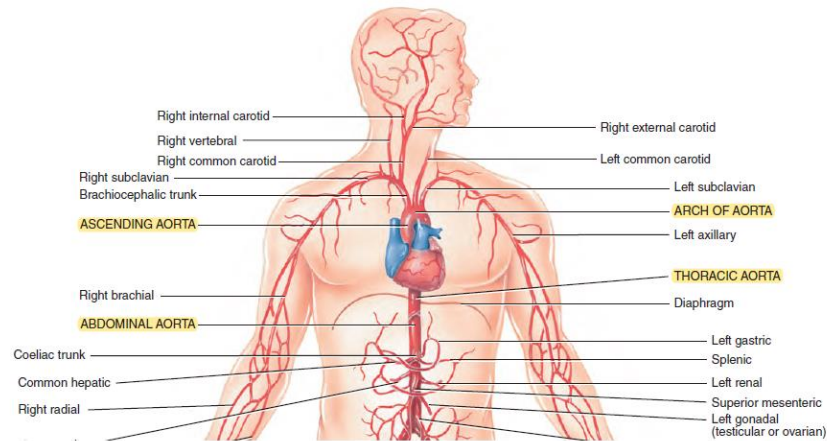
Figure 2.2: View of the principal branches of the aorta [12]

2.1.1 Statistics

Abdominal aortic aneurysm (AAA) disease results in 4500 deaths every year, with an additional 1400 death resulting from 45,000 rupture preventing operations conducted [14]. AAA disease occurrence is around 2–3 % of the whole population [15], [16]. According to Aggarwal et al. (2011), the disease has been identified as the 14th fatal disease. After the age of 60, AAA's occurrence is substantially increasing, so the condition is mostly characterized as a disease encountered at higher ages [17]. AAA presents 55 per 100,000 men aged 65-74, increasing 112 per 100,000 for age between 75 – 85 and 298 per 100,000 for 85 and higher age [18]. However, occurrence bias is not only related to age but also some other criteria like gender, race, hypertension condition, genetic predisposition, etc. For instance, women are less likely to get AAA 4 times than men; even if they get AAA, it happens approximately ten years on average later than men. As another example, it has been observed that in people with diabetes, AAA is less common [17]. These are mostly uncontrollable factors; besides, there is a significant factor that humans can control completely: "smoking" [19]. Smoking not only plays a role in the pathogenesis of AAA, but it also plays a role in the growth of bulges and rupture. Not as an example of a direct relationship, but as an example of correlation; only 15 percent of AAA

patients do not have a history of smoking [2]. Also, a recommendation exists that men aged 65 – 75 who have ever been a smoker should be check for AAA by The United States Preventive Services Task Force [14]. To sum up, AAA-related risk factors include advanced age, male gender, Caucasian origin, a positive family background, and smoking [6].

2.1.2   Rupture

Rupture is one of AAA's most frightening complications because the mortality rate of the rupture situation is reported between 78 – 94 % [4], [6]. In fact, it is described as one of the most critical emergencies in medicine, 4 – 5 % of the death in the United States is caused by the sudden rupture of AAA. Unfortunately, only 50 % of the ruptured AAA patients can reach the hospital alive, and only 50 % of those who make it to the hospital alive can survive the operation. That is the reason why factors determining rupture should be identified clearly to avoid those emergencies. Although many factors affect the rupture mechanism, one of the rupture's useful predictors is the diameter of the bulge. When the statistics are examined, it is not unreasonable to make the bulge diameter one of the main criteria. Below, there exists an evaluation of the annual risk of rupture according to the diameter of the AAA by The American Vascular Surgery Association and Vascular Surgery Society [20]:

• Less than 4.0 cm in diameter – 0%

• 4.0 cm to 4.9 cm in diameter – 0.5% to 5%

• 5.0 cm to 5.9 cm in diameter – 3% to 15%

• 6.0 cm to 6.9 cm in diameter – 10% to 20%

• 7.0 cm to 7.9 cm in diameter – 20% to 40%

• 8.0 cm in diameter or greater – 30% to 50%

As shown from the above statistics, there is a strong correlation between the bulge diameter and rupture. Yet, the diameter factor alone is not enough to thoroughly understand the rupture mechanism and foresee the rupture time; since some cases contradict these statistics. For example, there are many occasions where bulge diameter is 8 cm and did not rupture or its diameter of 4.5 cm, although it seems less likely but ruptured still. Furthermore, small diameter cases that enlarge more than 0.5 cm in six months are labeled as high-risk occasions and should be monitored regularly. It is also reported that this growth rate is rapid in smokers; on the other hand, it tends to be slower in patients with diabetes or peripheral vascular disease [17]. In addition to the size and growth rate of the aneurysm, ongoing smoking, unregulated hypertension, and increased wall stress are other conditions that enhance the risk of rupture [5]. To fully understand the rupture mechanism, the vessel diameter, growth rate, mechanical conditions of the vessel, blood properties, etc., and the vortex structure and wall shear stress on the bulge, which is discussed in detail in the upcoming sections, should be understood very well.

2.1.3 Repair

There are two repair types: open repair (OR) and endovascular repair (ER). Open repair is an application with a wide incision in the patient's abdomen, and the bulge is repaired directly with a synthetic graft. Besides, endovascular repair is the placement of a stent with the help of a catheter over the artery in the groin, shown in Figure 2.3.
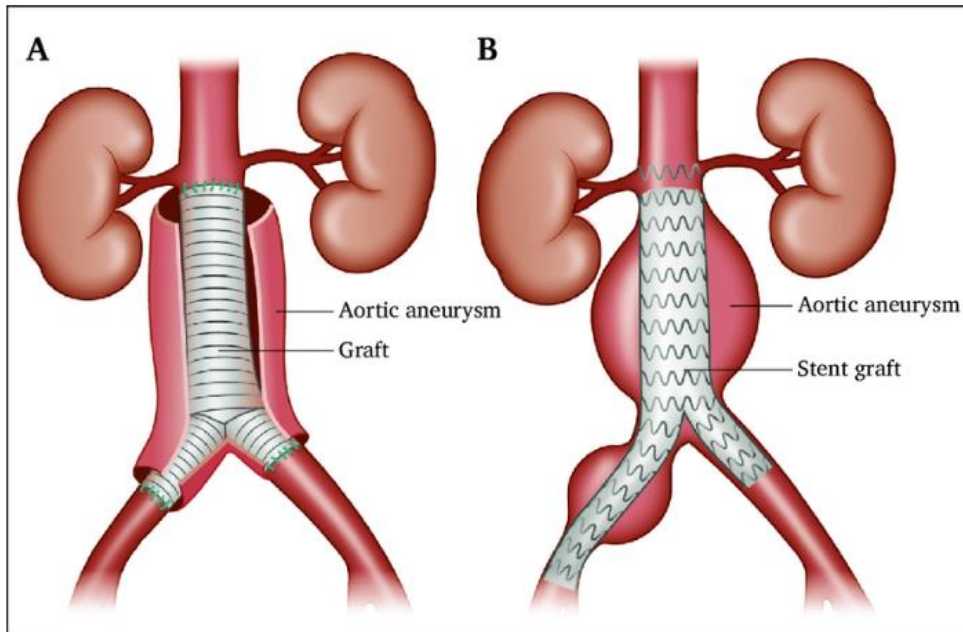
Figure 2.3: Illustration of repair types of AAA (Left: Open repair, Right: Endovascular repair) [21]

Open repair is an older method than closed repair. The open repair was first implemented in 1951, while the endovascular repair was first performed in 1986 [22]. As the advantages of endovascular repair are discovered, and technology is improved, the method has become more common.

Both methods have advantages and disadvantages. Open repair is a more invasive method, blood loss is more, and it requires the person to be operated on to be physically healthy and strong. Also, postoperative pain and prolonged recovery period are other drawbacks of open repair. On the other hand, endovascular repair is a new method that is more suitable for patients in the risky group, less time-consuming. It requires fewer hospital stays after the operations, but it is costly [22].

In terms of morbidity and mortality, endovascular surgery is considered very advantageous for the short term, which is one of the reasons why this method is increasingly common. Still, there are not many results on the long-term effects of the two methods because it is difficult to follow-up patients for a long time after the

operation. It is also difficult to distinguish between the two methods because the patient profile for which the two methods are generally applied is different in terms of the risk group.

Patel et al. (2016) explained the study includes data for the 15 years of follow-up for open and endovascular repair patients [23]. Aneurysm-related morbidity and mortality percentages for different times are included in Table 1. Fifteen years overall morbidity and mortality rates do not show any significant advantages or disadvantages for both sides. Short-term results agree with the general opinion that endovascular repair is more superior in terms of morbidity and mortality. On the other hand, as the postoperative time gets longer and longer, results shift the other way; open repair morbidity and mortality decrease significantly. This situation happens mostly because of the secondary rupture caused by endovascular repair-related occasions. 15% to 52% of the endovascular repairs, endoleaks, or mechanical failure of the device is experienced. As a result, most of the endovascular repairs require reintervention [15]. For this reason, open repair surgeries are considered as a more robust option than endovascular surgery.

Table 1 Percentages of aneurysm-related deaths over time for two different types of repairs [23]

Aneurysm-related mortality	**> 0 – 6 Months (%)**	**>6 months to 4 years (%)**	**> 4- 8 years (%)**	**> 8 years (%)**	**All Patients (%)**
Endovascular Repair	2	2	3	5	9
Open Repair	5	1	1	1	7

Considering all these factors described above, it is complicated to decide which type of operation is more suitable for each patient. It turns into a decision procedure in which all risks and results are optimized by considering the patient's age, gender, the anatomy of the aneurysm, the patient's life expectancy, estimated life span, and many other factors [24].

2.1.4   Symptom and Diagnosis

The abdominal aortic aneurysm (AAA) usually progresses as asymptomatic until it ruptures [17]. This factor makes this disease dangerous and critical to discover the rupture mechanism. AAA can be seen with pain in the back and abdomen, tenderness in the related area, weight loss, and elevated erythrocyte sedimentation rate [25]. Especially cases with pain and sensitivity on palpation are interpreted as high risk for explosion. AAAs can also present with complications because of thrombosis, embolization, etc. [17].

Thirty percent of vascular disease is accidentally discovered through the presence of a pulsatile mass during routine physical exams. Some of the cases are also found accidentally as a result of ultrasonography (USG), abdominal computed tomography (CT), and magnetic resonance imaging (MR) made for other reasons. In addition, some X-ray scans may determine calcification and indirectly show the aneurysm. Still, this detection method is not dependable since not all aneurysm cases result in an adequate calcification [17].

The sensitivity of physical examination varies between 22 - 96%. This range is high because physical examinations are highly dependent on obesity and abdominal distension. For example, while it is easy to identify a large aneurysm in a thin patient, it can be challenging to feel a small aneurysm in an overweight patient. Even the most experienced physician can miss the diagnosis of an aneurysm in these conditions [26].

USG is considered one of the primary methods for discovering aneurysms because it has a high accuracy of 95 - 100 % and is low cost and safe. The reasons for this probability decrease to 95% are similar to physical examination's misleading causes, but at a much higher rate, which is obesity and abdominal gas [17]. CT scan is less operator-dependent and screens the abdominal region in more detail than USG. Still, it is a more expensive method and considered less safe because of radiation exposure and contrast material application to the patient. MR scanning obtains higher quality images than the CT scan, but it is more expensive and difficult to access than CT [17],[27].

2.1.5   Vessel Structure

Due to the AAA, the geometry of the vessel alters. Therefore, structure within the vessel and flow properties inside change. A healthy abdominal artery consists of three layers: the inner layer (tunica intima), middle layer (tunica media), and outer layer (adventitia), which together form a thickness of around 0.2 cm [6]. When tissue samples taken from AAA patients are examined, layers can still be distinguished in some of them, but in most of them, these layers are disorganized, tortuous, and fragmented, which can be seen in Figure 2.4.
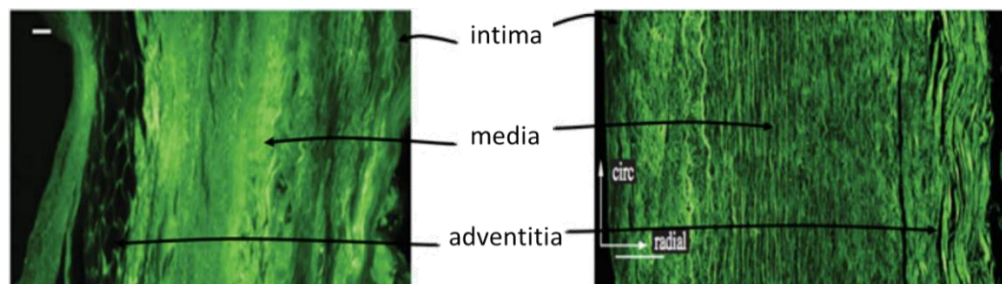
Figure 2.4: Presentative aorta wall structure imaged by second-harmonic generation microscopy (Left: Disrupted, Right: Healthy) [6]

As a result, this situation increases wall stiffness while decreasing compliance and distensibility. Thus, reducing the vessel's resistance to systolic pressure and deformation pulses creates the vessel's tendency to rupture. Moreover, AAA disease and rupture are associated with calcification and fat deposits, which are discussed in more detail in upcoming chapters and their relationship to flow structure [6],[28].

2.1.6 Rheology

Blood consists of solid particles such as platelets, red blood cells (erythrocytes), and white blood cells (leukocytes), which are suspended in the plasma [29]. It also includes proteins, minerals, organic materials, and water. That is why blood is called suspension fluid. Also, blood is known to be its non-Newtonian behavior. Non – Newtonian behavior is mainly caused by red blood cells' highly deformable behavior. At low shear rates, platelets merge into long structures result in increased viscosity. On the other hand, at high shear rates, platelets become an ellipsoid shape aligned with the flow lead to low viscosity [30],[31]. This behavior is called the shear-thinning characteristic. Hematocrit is the red blood cells amount in volume percent, and viscosity highly changes with hematocrit. Normal hematocrit value in human males is 42 to 45 % and slightly lower in females [29],[32]. In Figure 2.5, blood's non – Newtonian (shear thinning) characteristic and hematocrit dependence can be observed.
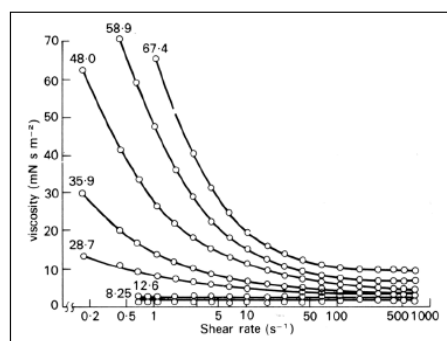
Figure 2.5: Blood viscosity plot as a function of shear rate (with different hematocrit values) [29]

In Figure 2.5, it can be said that blood shows a constant viscosity behavior after around 300 s⁻¹ shear rate. Blood's non-Newtonian behavior can be defined with the cross model, which equation can be seen in Equation (2.1):

$$\eta(\dot{\gamma}) = \eta_\infty + \frac{\eta_0 - \eta_\infty}{1 + \alpha\dot{\gamma}^{1-q}} \qquad (2.1)$$

Where:

η_∞ : viscosity for high shear rates

η_0 : viscosity for low shear rates

α and q : constant variables for the viscosity fit

Blood shows yield strength, which requires a specific stress value for starting to flow, and it shows viscoelastic behavior. It should be noted that the cross model does not present both of this behavior. When the circular tube flow is considered, the shear rate is not constant. Therefore, viscosity is not constant for the blood. That is why non – Newtonian characteristics have an effect, but some studies suggest that shear thinning on hemodynamics is small and Newtonian assumption is acceptable for the large arteries [31],[33],[34].

2.2 Experimental Set-up

2.2.1 Aneurysm Phantom

There are two fundamental approaches for phantom type in-vivo experiments: rigid wall and thin wall (compliant). The rigid wall is not affected by pressure changes; thus, it remains in constant geometry. Contrary to rigid wall, since the thin wall is elastic, inner pressure variations result in changes in the geometrical shape. Both approaches have advantages and disadvantages. For instance, although the rigid wall

model causes overestimations in parameters like Wall Shear Stress (WSS) and overall velocity, it is useful to discuss the theoretical side of flow physics. Since the overestimation of the parameters enables one to examine them easily and eliminate secondary effects caused by the changes in geometrical structure, it makes the examination process clearer [31],[35]. On the other hand, the compliance model is advantageous in being closer to real-life cases.

Yazdi et al. (2018) summarized and tabulated the researches on "rigid" and "compliant" models in literature in terms of materials used, production technique, refractive indices, etc. [36]. In the section below, the table and summaries of Yazdi et al. (2018) are used mostly. The most important parameter for the rigid walls is the refractive index (RI) since mechanical parameters like stiffness are not considerable for rigid structures. The refractive index of the phantom, which mimics the aneurysm, is crucial for determining the chemicals and their ratios that can be used in the blood mimicking fluid. In addition to the refractive index, the surface quality and the compatibility of the product with the desired model, in other words, tolerance, are also important in every production. There are three materials observed in the production of the rigid wall generally. These are Glass (RI =1.471), Silicone (RT601) (RI =1.403), Silicone (Sylgard184) (RI =1.4140) with their refractive indices. Due to its structure, glass is only observed in rigid wall production, while silicone materials are also observed in compliant models. The difference is caused by the production methods and the thickness of the model for the case of silicon materials. On the other hand, the glass materials are encountered in theoretical studies with simplified geometries mostly rather than patient-specific geometries due to the limits in the glass model's production techniques and its nature.

As mentioned above, silicone materials are generally used in compliant production models. Some materials can be listed as follows, Silicone polyurethane, Sylgard184, Silicone (T-2 Silastic), etc. And their refractive indices are 1.38, 1.414, and 1.43, respectively. The mechanical properties are highly dependent on the thickness of the phantom and the production techniques.

18

Since the vessel models have a curved structure mostly, although it is crucial to match the refractive indices of the phantom and the working fluid, it will be more appropriate to put the model into a box filled with the working fluid. In this way, a flat surface, where the camera lens is faced, is created, and the refraction problem is tried to be minimized [37]. Figure 2.6 and Figure 2.7 below show that this method is preferred for glass, but this is not needed for the rigid silicone models. The production method of rigid silicone is already creating a flat surface by casting it into a box.
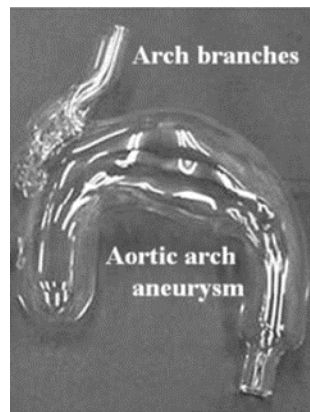
Figure 2.6: Image of a glass vessel model [38]

Figure 2.7: Casting box for PDMS with male mold [36]

2.2.2   Blood Mimicking Fluid

Blood is a fluid that includes various substances like platelets, proteins, and red-white blood cells. This property is considered as the reason behind the complex characteristics of the blood. Having a non-Newtonian structure is one of the complex characteristics of blood. Due to this structure, it shows changing viscosity behaviors for different shear rates. Simulating the blood real-like is important for in-vivo studies. In addition to properly stimulating blood, the refractive index is another important parameter for accurately determining the flow pattern for optical experimental in-vivo studies like PIV, LDA, etc.

One should avoid optical distortion at the wall since the working principle of optical flow measurement is illuminating the flow field and tracing the illuminated seeding particles. Thus, the refractive indices of blood mimicking fluid and the phantom material should be adjusted as close as possible to each other. The Refractive index effect can be observed in Figure 2.8.
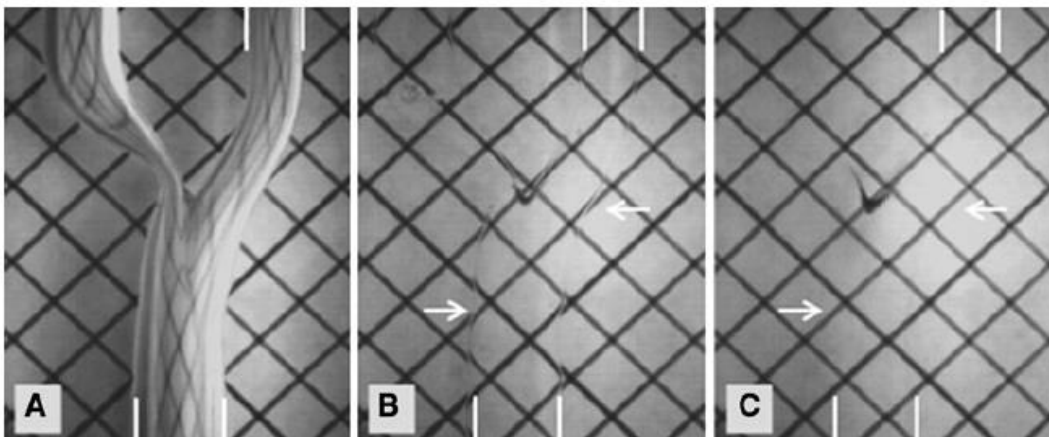
Figure 2.8: Presentation of the effect of the refractive index match between fluid and phantom model (Left to right filled with: Air – Nearly Matched RI – Optimally Matched RI) [39]

Using Newtonian blood mimicking fluid is preferred for large arteries in the literature because non-Newtonian fluid also shows behavior close to Newtonian in

large arteries where the observed shear rate is above 500 s^{-1} [40]. However, it is still controversial whether using Newtonian blood mimicking fluid is a good approach; thus, many studies in the literature uses non-Newtonian fluid.

Although using only distilled water and salts like NaI and KSCN increases the mixture's refractive index, most studies use distilled water and glycerin as a base mixture since glycerin increases both the fluid's refractive index and viscosity (for matching viscosity of blood). Even some studies use only water and glycerin mixture as blood mimicking fluid [41]. Matching the properties like refractive index and viscosity only with water and glycerin is challenging, especially with high refractive index requirements. It will require a high glycerin ratio in the mixture and result in higher viscosity than the blood's viscosity. This case makes it difficult to reach the high Reynolds numbers in experimental set-ups. Adding salts like NaI and NaSCN to the water - glycerin mixture is more suitable because salt addition makes it possible to increase the solution's refractive index with no or little change with kinematic viscosity [40].

There are some reported situations in salt usage that one should be careful about. In mixtures containing NaI salt, a color change that results in darkening, which prevents optical accessibility, can be observed and may be prevented by minimizing the interaction of the oxygen with the fluid. If a color change occurs, it has been reported that reheating helps to recover this unwanted situation [42]. Also, the darkening can be treated with an additional chemical compound called Sodium Thiosulfate (Na$_2$S$_2$O$_3$) [39]. NaSCN can also be used instead of NaI; similar to the NaI; it has been reported that mixed NaSCN salt mixture may change its color because it contains Thiocyanate ([SCN]$^-$) [43]. Since it can disrupt optical access after a certain level, it is necessary to be careful about this color change. Also, salt-containing mixtures are challenging in terms of safety. Mixtures containing salt are corrosive; they can be harmful to materials used in the experimental set-ups discussed in Aneurysm Model and Blood Mimicking Fluid section [44].

Non-Newtonian blood mimicking fluids are better at simulating real-cases, especially if the shear rate in the flow is low and pulsatile or oscillatory flow is being inspected [45]. In order to give the shear-thinning and viscoelastic characteristics and as a result non-Newtonian behavior to the mixture, two substances are generally considered; these are xanthan gum (XG) and polyacrylamide [40]. It is stated that the glycerin–xanthan gum–water solution has larger elasticity than blood, while their shear-thinning properties match. In addition, the elasticity is much greater for the polyacrylamide solutions than in blood, which creates considerable differences in fluid dynamics. Thus, to obtain non-Newtonian characteristics similar to the blood, XG can be considered the best substance [45],[46].

As a footnote for the non-Newtonian mixtures, Long et al. (2005) claims that NaI does not affect the viscoelastic properties created by the xanthan gum, but a study done by Najjari et al. (2016) claims the differ [47]. Najjari et al. (2016) realize that NaI changes viscoelasticity and reduces the shear-thinning property of the non-Newtonian mixture [40]. The same situation is also observed for NaSCN salt, which is an alternative for NaI. Therefore, one should be careful about salt usage for adjusting the RI of the mixture; non-Newtonian properties should be checked and measured if possible. Table 2 contains mixing ratios offered by Najjari et al. (2016) for three different refractive index levels with NaI and NaSCN. Also, in Figure 2.9, steady shear viscosity behaviors of the offered mixtures can be seen.

Table 2 Composition of non-Newtonian fluids shown in weight percentages equivalent to grams of materials in 100g of final fluid [40].

DIW	Gly	XG	NaI	NaSCN	RI	Density(kg/m³)
67.94	32	0.060	0	0	1.373	1050
49.69	23.4	0.044	26.87	0	1.417	1280
33.97	14	0.030	50.0	0	1.477	1657
30.26	14.25	0.028	55.46	0	1.495	1678
53.45	25.18	0.047	0	21.32	1.417	1165
37.5	17.66	0.033	0	44.81	1.470	1285
30.95	14.57	0.027	0	54.45	1.495	1351
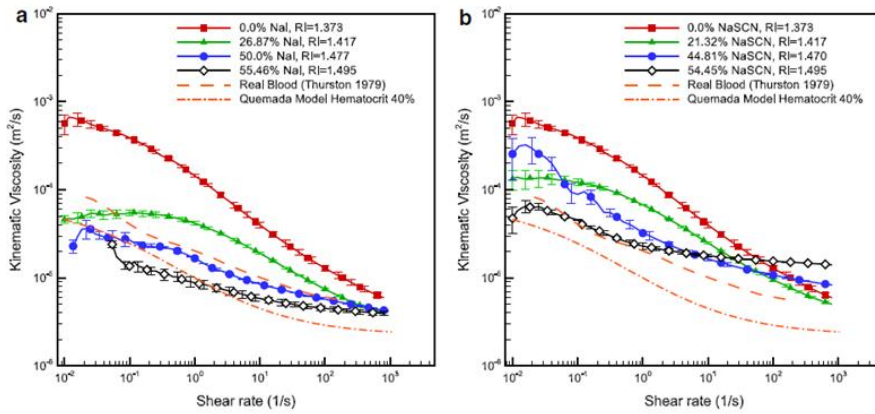
Figure 2.9: Xanthan Gum–Glycerin-Distilled Water - (NaI and NaSCN) mixture's steady shear viscosity properties for different refractive index adjustments (a: NaI, b: NaSCN) [40]

Recently for the vessel phantom, Polydimethylsiloxane (PDMS) material becomes more common, and as a result, a new mixture alternative emerges. A study done by Brindise et al. (2018) claims that instead of NaI salt usage, urea is a much more cheap, safe, and coloration-free alternative for PDMS refractive index levels. Also, urea has the advantage of not changing density compared to NaI; because, although NaI does not affect the kinematic viscosity of the mixture, it increases the density by about 6.0 kg/m3 per weight percent added, which result in a higher final density of

the mixture compared to the blood [44]. So, urea offers viscosity, density, and refractive index match simultaneously. For the non-Newtonian mixture, similar behaviors are observed with NaI.

2.3 Wall Shear Stress

2.3.1 Theory

In solid mechanics, materials deform to a certain extent under the applied shear stress. When the deformation reaches equilibrium with the shear stress, it stops. The material remains stable in static equilibrium unless it undergoes creep due to thermal or environmental reasons, as shown in Figure 2.10.
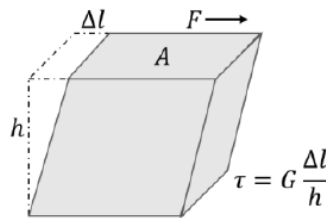
Figure 2.10: Shear stress applied to an elastic material [31]

On the other hand, fluids continue to deform as long as shear stress is applied, so fluids cannot compensate for the shear stress in terms of static equilibrium. For this reason, shear stress in fluids is related to the rate of deformation, not the deformation [48]. WSS vectors are calculated for each wall point using the equation:

$$\vec{\tau} = 2\mu(\dot{\varepsilon}.\vec{n})$$

Where $\dot{\varepsilon}$ is the rate of deformation tensor, $\vec{n}$ is the inward normal vector (for the specific wall point), and μ is the fluid's dynamic viscosity. As a result, the below matrix is constructed.

$$\vec{\tau} = 2\mu(\dot{\varepsilon}.\vec{n}) = 2\mu \begin{pmatrix} \dfrac{\partial u_x}{\partial x} & \dfrac{1}{2}\left(\dfrac{\partial u_x}{\partial y} + \dfrac{\partial u_y}{\partial x}\right) & \dfrac{1}{2}\left(\dfrac{\partial u_x}{\partial z} + \dfrac{\partial u_z}{\partial x}\right) \\ \dfrac{1}{2}\left(\dfrac{\partial u_y}{\partial x} + \dfrac{\partial u_x}{\partial y}\right) & \dfrac{\partial u_y}{\partial y} & \dfrac{1}{2}\left(\dfrac{\partial u_y}{\partial z} + \dfrac{\partial u_z}{\partial y}\right) \\ \dfrac{1}{2}\left(\dfrac{\partial u_z}{\partial x} + \dfrac{\partial u_x}{\partial z}\right) & \dfrac{1}{2}\left(\dfrac{\partial u_z}{\partial y} + \dfrac{\partial u_y}{\partial z}\right) & \dfrac{\partial u_z}{\partial z} \end{pmatrix}.\vec{n}$$

The diagonal elements of the deformation tensor present the deformation for normal stresses, and the remaining elements present shear stress deformations. For each point on the vessel, the selection of a local coordinate system by employing rotation $\mathcal{R}$ to the original coordinate is shown in Figure 2.11.

$$\mathcal{R}[x'\ y'\ z'] = [x\ y\ z]$$

$$\vec{n}(x, y, z) = [0\ 0\ 1]$$
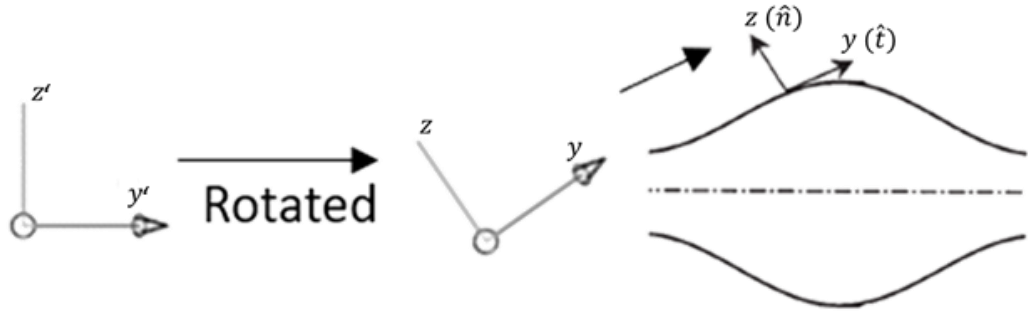
Figure 2.11: Illustration of the rotation of coordinate axis for aneurysm

With the assumption of no flow through the vessel wall, i.e., $\vec{n}.\vec{V} = 0$ at the vessel wall, which is valid for large, non-porous vessels [49]. The assumption reduces most terms in the equation to zero, and the WSS in the local coordinate system is defined by Equation (2.2):

$$\tau_w = \mu \left[\dfrac{\partial u_x}{\partial z}\ \dfrac{\partial u_y}{\partial z}\ 0\right] \tag{2.2}$$

For 2-D, it reduces to Equation (2.3):

$$\tau_w = \mu \left[\dfrac{\partial u_y}{\partial z}\ 0\right] \tag{2.3}$$

2.3.2   Velocity Fit Profiles

For the experimental wall shear stress studies, different kinds of velocity fit models are needed. It is caused by the technical characteristics of the measurement equipment. The first thing to consider is spatial resolution constraints, but even if the resolution is not high enough, it can be improved for the wall shear stress measurement. Still, some other reasons exist that cannot be dealt with efficiently because those reasons are related to the nature of the measurement technique. For example, in near-wall PIV, data near the wall are bias (overestimation mostly) [50] because of the cross-correlation algorithm of the PIV where high gradients exist [51]. Also, in most cases, seeding particle is inhomogeneous for the near wall, seeding particle accumulation can be seen, and light refraction of the wall caused by refractive index difference between model and working fluid occurs. These situations make it hard to get meaningful data near the wall, which is also valid for other optical measurement methods like Laser Doppler Anemometry. For this reason, it may be logical to start with the first non-biased data closest to the wall and create a velocity profile fit by using the information behind that first data because, until the first non-biased data, some distance from the wall can occur. Only the first data that can be taken close to the wall may not be sufficient for wall shear stress calculations.

Petersson et al. (2012) investigate three techniques that depend on near-wall velocity for calculating WSS. While the first method utilizes linear interpolation together with the wall position (Vel-Wall method), the second method uses linear extrapolation (Vel-LE method). Moreover, the third method utilizes parabolic fitting together with the wall's position (Vel-Parabolic). The schematic presentation of the aforementioned methods can be seen in Figure 2.12 [52].
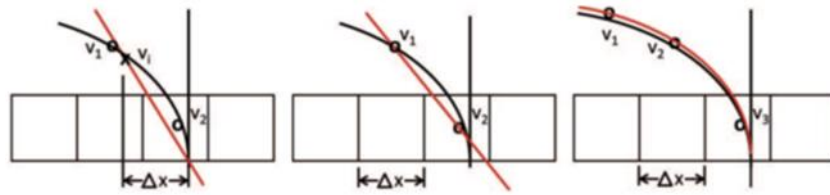
Figure 2.12: Overview schematics of the WSS estimation profiles (Left to right: Vel-Wall method, Vel-LE method, Vel-Parabolic) [52]

Since the Vel-LE method is linear extrapolation-based, it has the advantage of being independent of the wall location. This method can be considered for cases where wall location is not certain, but it should be noted that it becomes less accurate for cases where grids are not aligned with the wall-normal. The other two methods are wall location dependent. Petersson et al. (2012) concluded that parabolic (2nd order) fit is more accurate than other options [52].

Fatemi and Rittgers et al. (1994) stated that the most accurate shear-rate estimation could be obtained by four points provided with a third-degree polynomial curve fit for a study conducted on wall shear rates, measured by laser doppler anemometry with various curve-fitting methods [53]. In the literature, it is observed that parabolic velocity fit methods have been used up to the 5th order [49].

Apart from the linear and polynomial velocity fitting methods mentioned above, the spline velocity fitting method is used. A spline is, by definition, a set of piecewise polynomials, so it does not force all fitting points into a single order equation. This structure offers a more robust fitting, especially in complex flows [54],[55].

DiCarlo et al. (2018) use cubic spline fit for the WSS calculations for the in-vivo PIV study because physiological flows are far more complicated, with changing boundary layer thickness and flow regimes spatially [31]. Four points are used for the cubic spline fit and the "zero" velocity point on the wall with 0.3 mm intervals on the wall-normal. "0.3 mm" is not a universal rule for this kind of study; it is

determined with grid size, ensuring that interpolation points fall in unique and neighboring grids where possible.

2.3.3 WSS Parameters

Hemodynamics plays an important role in the physiology of healthy vessels and the development of vascular wall diseases. For the vascular wall diseases case, hemodynamics is especially important in regions like bulges, curvatures, and arterial bifurcations where the flow becomes complicated. It is a common idea that, in large arteries, the location of atherosclerosis (plaque builds up inside arteries) is strongly related to where flow gets disturbed, which correlates with rupture and vessel growth mechanisms [56].

There are 5 WSS - based metrics defined in the literature that quantitatively describe the interaction between vessel structure and blood flow, that is, the sensitivity of local hemodynamics to inflow and outflow boundary conditions, and are used in this study. Those basic parameters are Time Average Wall Shear Stress (TAWSS), Time Average Wall Shear Stress Gradient (TAWSSG), Wall Shear Stress Gradient (WSSG), Oscillatory Shear Index (OSI), and Temporal Wall Shear Stress Gradient (TWSSG). Although none of these metrics' impact on the vessel structure is certain, and some conflicting opinions exist on this subject, there are detected correlations between those parameters and the state of the vessel. Several other variables have been suggested, such as the peak WSS temporal gradient, dominant harmonic, etc. [57],[58],[59],[60].

➢ TAWSS and OSI

TAWSS is calculated to present the time average of all the time-varying patterns for examinations. It is a convenient indicator since the vessel is constantly subjected to the averaged physiological pattern. Yet, if WSS is desired to examine in terms of time separately, spatial WSS distributions of each time can be extracted. Low TAWSS magnitude is known to stimulate endothelial corruption. On the other hand,

high TAWSS can lead to endothelial trauma and hemolysis (destruction of red blood cells) [56]. The equation of the TAWSS metric is shown in Equation (2.4) below.

$$TAWSS = \frac{1}{T} \int_0^T |\tau_w|\, dt \qquad (2.4)$$

The oscillatory shear index (OSI) is a metric first developed by Ku et al. (1985). OSI defines ensemble-averaged local wall shear stress variation, especially for pulsatile flow, and is commonly used in numeric and experimental studies [61]. It identifies the internal flow's oscillatory impact on the wall during the cardiac cycle.

OSI values range from 0 to 0.5, presenting the deviation of WSS from the direction of the main flow. In other words, in regions with minimal flow disruptions, low OSI values occur. High OSI values are encountered in case of rapid WSS changes (in a directional manner) from the main flow for a cardiac cycle. Furthermore, a correlation between the high OSI values and perturbed endothelial alignment is observed [62]. Such areas are generally related to bifurcating flows and vortex formation. They are linked to atherosclerotic plaque formation and intimal hyperplasia (thickening of intimal cells of the vessel) [63]. The equation of the OSI metric is shown in Equation (2.5).

$$OSI = \frac{1}{2}\left[1 - \left(\frac{\left|\int_0^T \tau_w\, dt\right|}{\int_0^T |\tau_w|\, dt}\right)\right] = \frac{1}{2}\left[1 - \left(\frac{\tau_{mean}}{TAWSS}\right)\right] \qquad (2.5)$$

Several studies indicate that particularly low WSS and high OSI correlated spatially with the localization of atherosclerotic (thickening or hardening of the arteries) disease, which is highly correlated with the rupture [60]. Also, these metrics are strongly related to intimal hyperplasia [56]. Some of the studies mentioned are for human carotid, but similar conditions can be seen and valid for other vascular segments such as the Abdominal Aortic Aneurysm (AAA) [60]. However, plaque

sensitivity may be connected to excessive wall shear stress (WSS), which is commonly present on the proximal side of existing plaques [10].

As a footnote, although low WSS - high OSI theory is the generally accepted connection for atherosclerotic disease, some researchers such as Steinman et al. (2002), Gijsen et al. (2007), and Peiffer et al. (2012) could not find any evidence to confirm that. The researchers conducted point-to-point comparisons of WSS distribution with disease progression, but generally accepted relation (Low WSS/High OSI) could not be supported [60]. However, since general acceptance is built on low WSS -high OSI theory, results are interpreted by referring to this theory in this study.

➢ WSSG and TAWSSG

WSSG is used to present the spatial variation of the WSS distribution. The TAWSSG metric is also calculated to see the general spatial variation characteristic in cases with time-varying patterns. WSSG is first proposed by Lei et al. (1995) as a hemodynamic indicator [57],[60]. It measures the spatial changes in surface forces/unit area, which has a high impact on the endothelial cells [64].

Lei et al. (1995) state that regions with high WSSG magnitudes are also where the fat and minerals accumulated. Furthermore, Lei et al. (1995) also mentioned that high WSSG is correlated with intimal thickening. In addition to the intimal thickening, cell dysfunction, excessive release of growth factors, smooth muscle cell proliferation (rapid increase), platelet aggregation is also correlated with the high WSSG. These conditions are related to the onset and progression of vascular diseases. Lei et al. (1995) and Buchanan et al. (1999) denote that the places where the abnormal (non-uniform) hemodynamic is most experienced on a vessel are associated with the places where the spatial gradient is high [57],[64]. The equations of WSSG and TAWSSG are provided in Equation (2.6) and Equation (2.7) below.

$$WSSG = \frac{\partial \tau_w}{\partial \hat{t}} \qquad (2.6)$$

$$TAWSSG = \frac{1}{T} \int_0^T \left(\frac{\partial \tau_w}{\partial \hat{t}} \right) dt \qquad (2.7)$$

➤ TWSSG

Temporal Wall Shear Stress Gradient (TWSSG) allows the WSS gradient to be examined as time variation rather than spatially. According to White et al. (2001), it is observed that temporal changes stimulate endothelial cell proliferation and disrupt its structure [8]. This situation causes the vessel to be prone to possible vascular enlargement or rupture. The equation of the TWSSG metric is shown in Equation (2.8) below.

$$TWSSG = \frac{\partial \tau_w}{\partial t} \qquad (2.8)$$

Metrics that are calculated in this study and their formulas can be seen in Table 3 below.

Table 3 Table of the WSS parameters calculated in the present study together with abbreviations and formulas

Metric	Abbreviation	Formulae
Time Average Wall Shear Stress	$TAWSS$	$\dfrac{1}{T}\displaystyle\int_0^T |\tau_w|\, dt$
Oscillatory Shear Index	OSI	$\dfrac{1}{2}\left[1-\left(\dfrac{\left|\int_0^T \tau_w\, dt\right|}{\int_0^T |\tau_w|\, dt}\right)\right]=\dfrac{1}{2}\left[1-\left(\dfrac{\tau_{mean}}{TAWSS}\right)\right]$
Wall Shear Stress Gradient	$WSSG$	$\dfrac{\partial \tau_w}{\partial \hat{t}}$
Time Average Wall Shear Stress Gradient	TAWSSG	$\dfrac{1}{T}\displaystyle\int_0^T \left(\dfrac{\partial \tau_w}{\partial \hat{t}}\right) dt$
Temporal Wall Shear Stress Gradient	TWSSG	$\dfrac{\partial \tau_w}{\partial t}$

2.4   Previous Studies

This section summarizes studies that characterize the flow field and wall shear stress of the aneurysm. These studies include both numerical and experimental methods such as PIV and LDA.

Finol et al. (2002) – Part 1 [65] and Finol et al. (2002) - Part2 [66] are two-part numeric studies that include steady (Part 1) and physiological approaches (Part 2). An axisymmetric, double aneurysm geometry is used, which can be seen in Figure 2.13. Finol et al. (2002) compare the steady numerical results for the range 10<Re<2265. Below, in Figure 2.13, streamlines for different Re numbers can be observed. After the "b" part of Figure 2.13, characteristics behavior for the bulges starts that is mainstream flow below and low velocity and recirculating zones above.

32
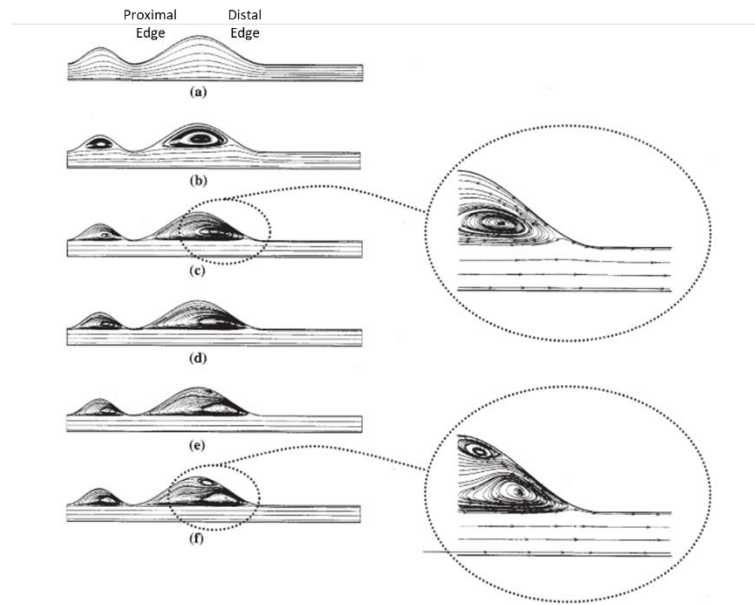
Figure 2.13: Laminar steady flow streamlines (a: Re=10, b: Re=100, c: Re=500, d: Re=1000, e: Re=1750, f: Re=2265) [65]

Figure 2.14 shows WSS and WSSG distribution for the abovementioned steady Re patterns. At the middle of the bulge, smaller negative WSS is observed because of the counter-clockwise recirculating zones (low velocity region) compared to peak values. At the proximal edge, where boundary layer separation appears, changes in the sign of the WSS (stagnation point) can be encountered. A similar pattern also happens in the distal neck.
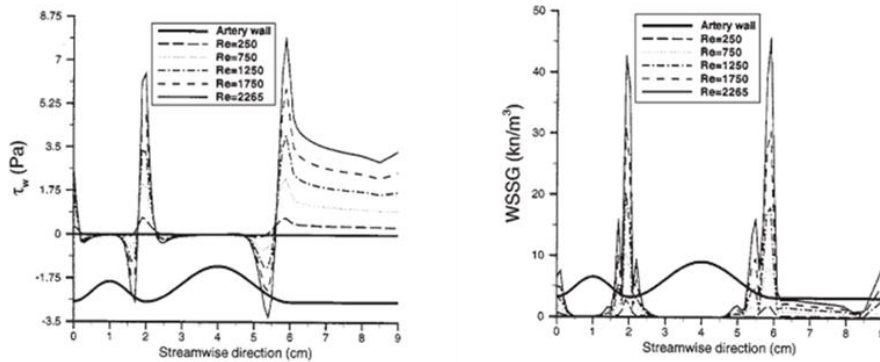
Figure 2.14: WSS and WSSG distribution for steady, selected Reynolds numbers [65]

33
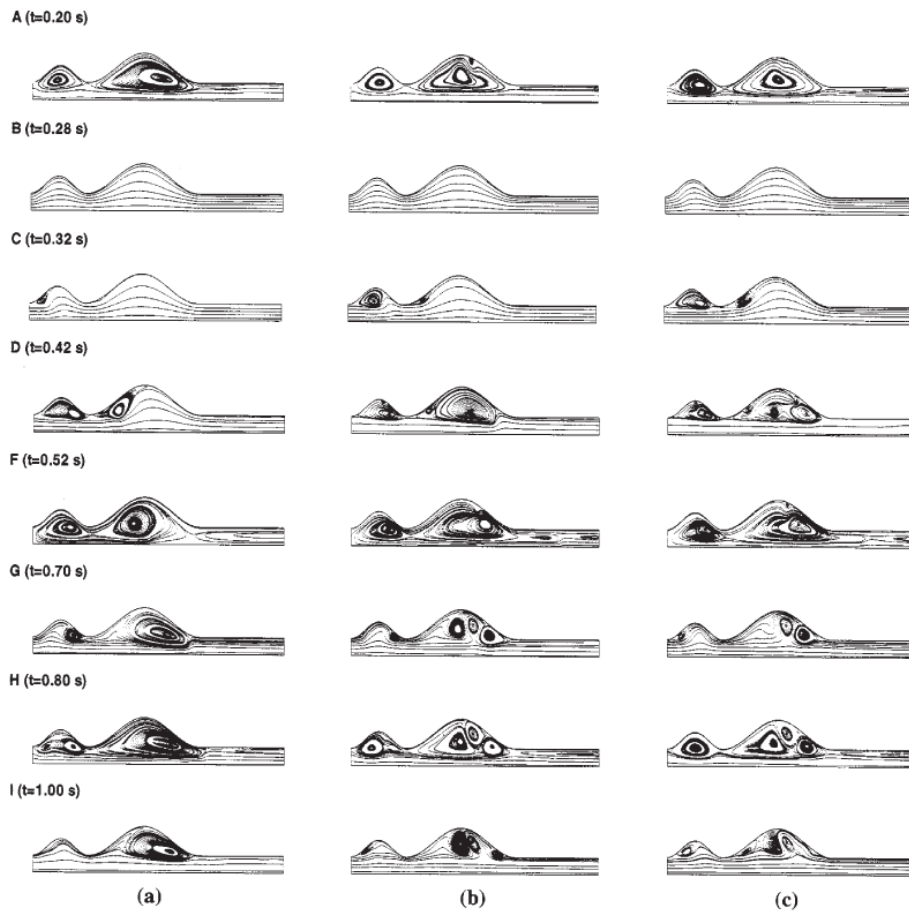
Figure 2.15: Pulsatile flow streamlines (a: $Re_{mean} = 100$, b: $Re_{mean} = 200$, c: $Re_{mean} = 300$) [66]

In the second part, Finol et al. (2002) investigated the same aneurysm geometry for three different physiological flows with different average Reynolds numbers. The notable points explained in these flow patterns are visualized in Figure 2.15 above and WSS variations presented in Figure 2.16 below.

Growth is observed in the recirculating regions at the beginning of the physiological pattern due to the negative velocity gradient. Between $0.2 \, sec < t \leq 0.31$ seconds, the flow attaches to the wall, and the regions recirculating with low velocity are ejaculated due to the high velocity. Because the deceleration rate is higher at high Reynolds values, larger recirculating regions and smaller attached flows are observed. In the second acceleration realized in $0.52 < t \leq 0.7$ seconds, it is observed

that the small vortex structures partially disappeared. Three vortex structures start to be observed with the adverse pressure gradient caused by the deceleration observed in 0.7 sec < t ≤ 0.8 seconds. A slight contraction in the vortex structures with a slight acceleration and straightening of streamlines are observed with the stabilized flow in the rest of the cycle. In general, the WSS and WSSG distribution are similar to the steady pattern, with a negative peak at the distal end, followed by a sharp rise and a positive peak. Besides, in the center, low WSS distribution is observed.
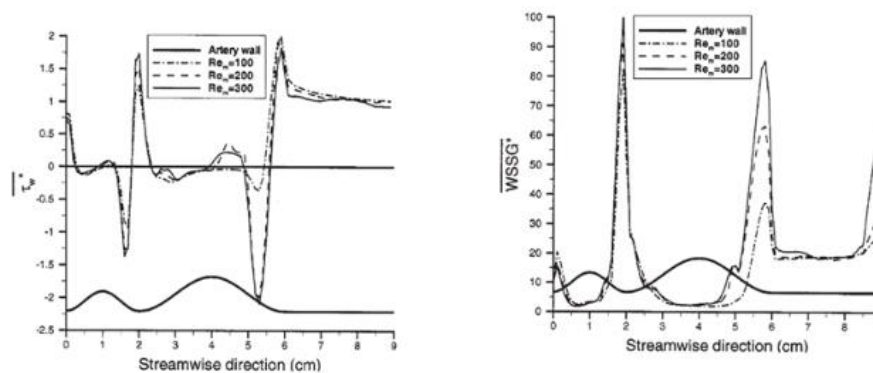
Figure 2.16: Time average WSS and time average WSSG distribution for physiological, selected mean Reynolds numbers [66]

Bauer et al. (2019) use Magnetic Resonance Velocimetry (MRV), Laser Doppler Anemometry (LDA), and numerical simulations in order to calculate Wall Shear Stress on the aneurysm wall since measuring the wall shear stress in the best way is an open and contentious topic [67]. In this study, the MRV results are compared with the result coming from LDV and numeric results. Also, for circular pipe (typical human aorta) pulsatile flows where analytical solutions exist compared with the experimental results. Experimental and numeric studies are also conducted for aneurysm geometry in steady flow conditions, including turbulent Re numbers. As an aneurysm model, geometry is taken from the studies of Budwig et al. (1993), Peattie et al. (2004), and Salsac et al. (2006) with d=26 mm, L=104 mm, and D=65 mm corresponding L/d = 4 and D/d = 2.5 [9],[68],[69].

When the LDA measurement volume intersects with the wall partially, resultant data give an overestimated velocity information [70]. For the WSS calculation, the first velocity data closest to and fully isolated from the wall is used for the LDV measurements. On the other hand, for MRV calculations, the second data point closest to the wall is used because the partial volume effects can cause misleading data for the first data. But for both measurement techniques, the linear fit between used velocity data and wall location (zero velocity, no-slip boundary conditions) is used in order to calculate the wall shear stress (WSS). In Figure 2.17, the WSS result includes all the techniques used in this study for the steady (Re = 1998) case with Budwig et al. 1993 result for the same case and geometry. Although there seems to be a difference between the results of Budwig et al. (1993) for peak locations, it is explained with the geometry differences. LDV measurements seem in agreement with the literature and numerical results, but MRV results underestimate the high wall shear stresses due to the spatial resolution.
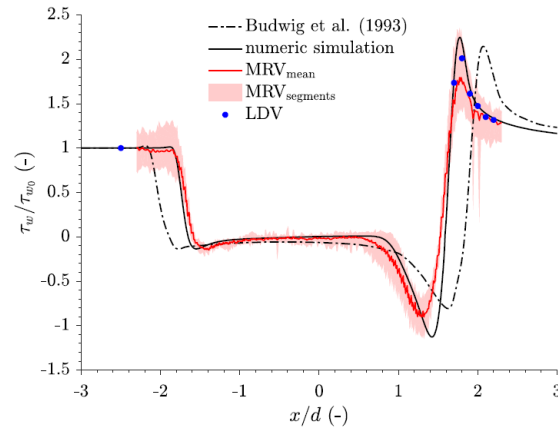
Figure 2.17: Experimental and numerical normalized WSS results with Budwig et al. (1993) comparison [67]

Bauer et al. (2019) also study turbulent flows. Vicinity of the wall there is a typical velocity profile shape when made dimensionless in every turbulent flow. Near the wall where viscous forces dominate, the velocity profile is linear. Further away from the wall, a logarithmic velocity profile is observed. There is also the buffer region

between the linear and logarithmic layers, softly connecting the two regions [71]. Four different turbulent velocity profile approaches tried written below:

- Manuel Estimation

In this method, velocity gradient is determined by visual inspection, and the highest gradient is generally preferred. It proceeds independently of the general turbulence velocity profiles mentioned above.

- Musker

For the second method, velocity data are fitted to a velocity profile written below in Equation (2.9) created by Musker (1979). "Musker" method relies on velocity profiles mentioned above, and it is valid for viscous sublayer to the logarithmic region [72].

$$\frac{du^+}{dy^+} = \frac{\frac{(y^+)^2}{\kappa} + \frac{1}{s}}{(y^+)^3 + \frac{(y^+)^2}{\kappa} + \frac{1}{s}} \tag{2.9}$$

where:

$$\kappa = 0.41 \quad s = 0.001093$$

- DNS Fit

The third method relies on the velocity profile model extracted from the DNS of a numerical pipe flow (Re = 5300) done by El Khoury et al. (2013) [73].

- Durst

In the last method, an equation to be fitted to measurement data, Equation (2.10) created by Durst et al. (1996b), is used [74].

$$u = \frac{u_\tau^2}{v}(y - y_0) + C_2(y - y_0)^2 + C_4(y - y_0)^4 + C_5(y - y_0)^5 \tag{2.10}$$

Where:

C_2, C_4, C_5, u_τ and y_0 are free. The equation is available for $y^+ < 12$

Bauer et al. (2020) [75] used a similar experimental set-up and methods in the 2020 study with Bauer et al. (2019), but as a difference, the physiological pattern is used for aneurysm geometry. Vector fields and WSS results together with the time instances in which data is taken, shown in Figure 2.18. Flow characteristics and WSS results found in this study are similar to the Finol et al. (2002) study discussions; flow fields findings are not detailed again. Instead, measurement method result differences are discussed.
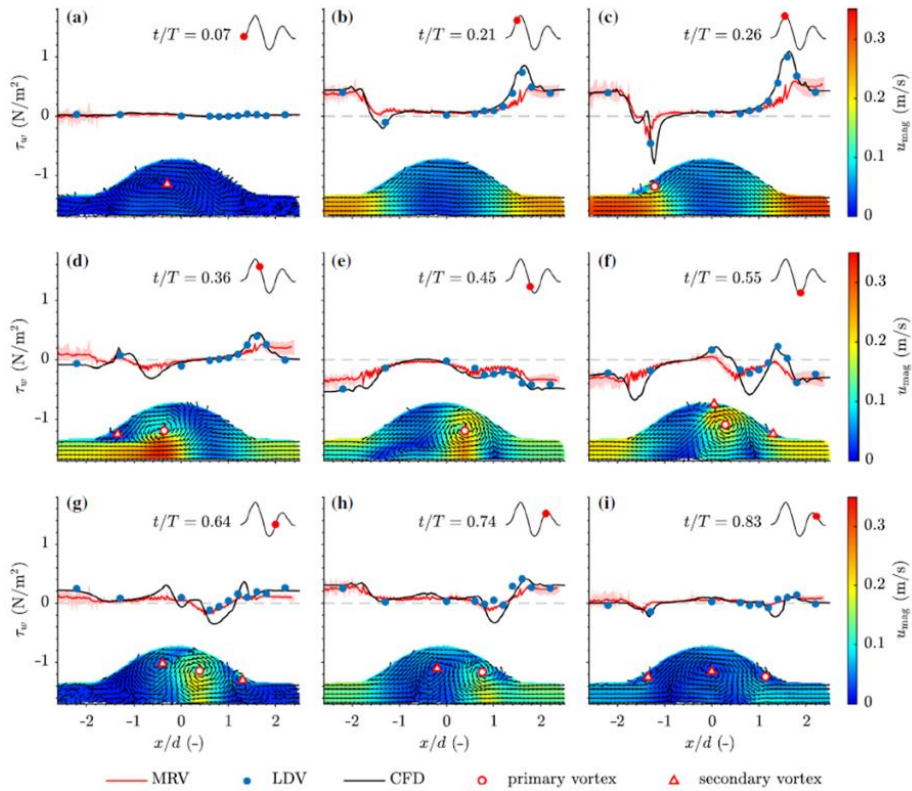
Figure 2.18: WSS variation for different time points with MRV, LDV, and CFD results [75]

Figure 2.18 shows WSS results containing the data taken from MRV, LDV, and CFD studies. MRV result seems to underestimate the WSS values, especially for the vortex formation region where high temporal changes are observed (x/d = -1.3.) Below Figure 2.19, LDV, CFD, and MRV results are taken at the x/d = -1.3 region.

As shown in Figure 2.19, MRV results underestimate the peak values because of the spatial and temporal resolution inefficiency.
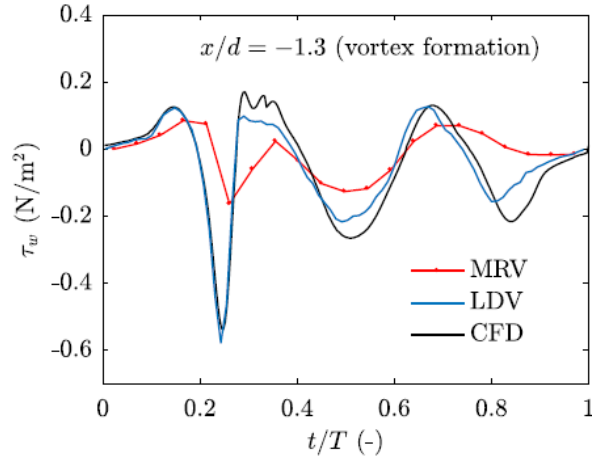
Figure 2.19: WSS variation at x/d= -1.3 with MRV, LDV and CFD results [75]

DiCarlo et al. (2018) investigate the WSS and some related parameters' distribution (OSI, TAWSS, etc.) on the carotid bifurcation using Particle Image Velocimetry [10]. Both Newtonian and Non – Newtonian working fluids are used to spot the difference between the two mimicking fluid approaches.

For the processing, the Fast-Fourier transform cross-correlation algorithm is used. Interrogation area is chosen 64x64 to 16x16 pixel with 50% overlap. As a result, 0.3 mm grid spacing is obtained. For the velocity fit model, 3 data points at 0.3 mm distance from each other are used with "0" velocity data on the wall (no-slip boundary condition). These velocity points are aligned on the wall-normal, and between these points, the cubic spline fit is applied to calculate the gradient near the wall.

Figure 2.20 below shows that WSS and OSI contours of the carotid bifurcation can be seen for both Newtonian and non – Newtonian blood mimicking fluid experiments using WSS calculation methods explained above.
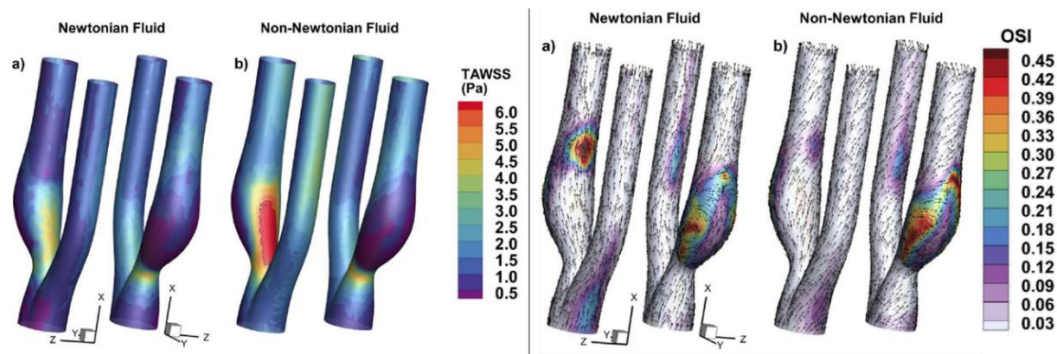
Figure 2.20 Comparison of Newtonian and non-Newtonian approaches for TAWSS and OSI distributions [10]

Considering these results and the experiments performed in other branching ratios, it is observed that the Newtonian approach underestimates the WSS value in general and overestimates some low WSS regions. Also, in general, Newtonian fluid predicts higher OSI than non - Newtonian fluid. In other words, the Newtonian viscosity approach detects low WSS – high OSI regions with higher area coverage.

CHAPTER 3

EXPERIMENTAL SET-UP AND MEASUREMENT TECHNIQUES

This chapter of the thesis covers the details of the experimental set-up and measurement techniques.

3.1   Blood Circulatory System

The experiments are conducted in a flow circulatory system placed in the Fluid Mechanics Laboratory of the Mechanical Engineering Department of Middle East Technical University. The circulatory mock loop model used in the study can be seen in Figure 3.1. The images of the experimental set-up are provided in Figure 3.2, Figure 3.3, and Figure 3.4 from different perspectives.
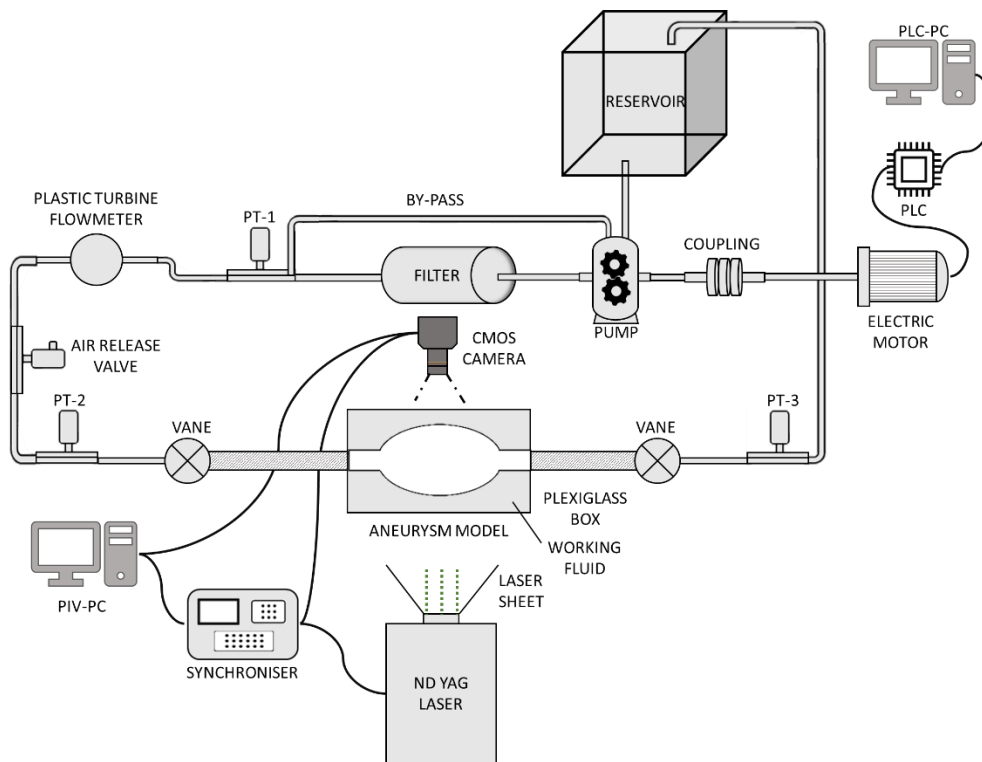
Figure 3.1: Schematics of the experimental set-up used in the present study

Figure 3.2: Picture of the data processing section of the experimental set-up

Figure 3.3: Picture of the circulatory system with flowrate and pressure measurement equipment
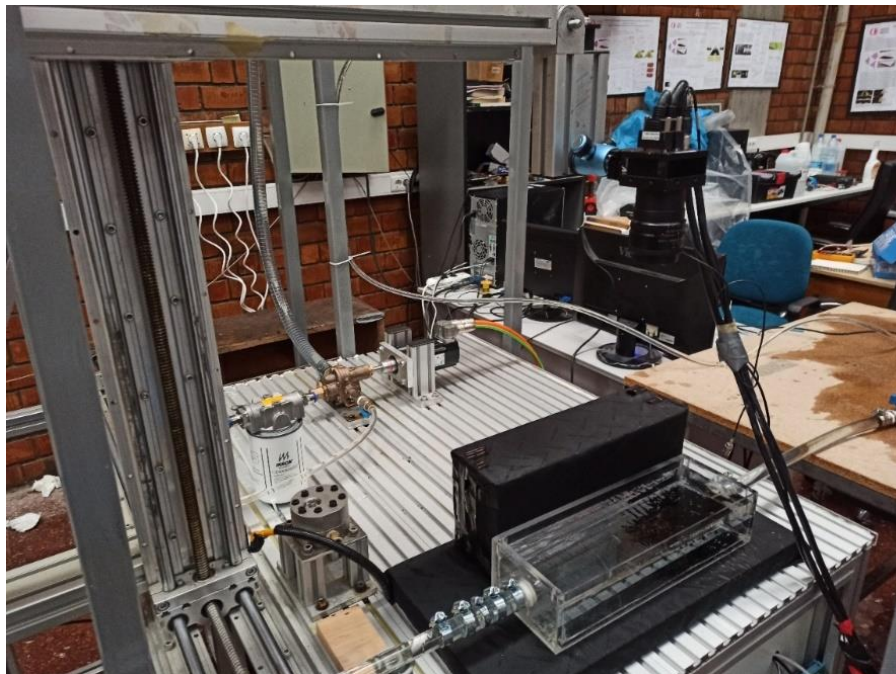
Figure 3.4: Picture of the pump, filter, and the aneurysm model

After the working fluid is drawn from the tank with the help of the gear pump, which is driven by an electrical motor, the fluid passes through the filter. Using a filter keeps the aneurysm region where the camera is focused, and some optical concerns are present clean. To achieve this, the IKRON / HE K45-20.135-AS-SP 025 filter is used. The filter is removed from the system after ten minutes of filtration due to the reactivity of the working fluid. Furthermore, as observed from the pressure measurements, the filter creates a disturbance in the physiological flow pattern. For this reason, after the system is filtered and isolated from the environment, the filter is bypassed during the experiment process.

As shown in Figure 3.1, the fluid passes through three different pressure transducers, turbine flowmeter, air release valve, and the aneurysm model. The aim of implementing the air release valve is to prohibit bubble occurrence in the system. The purpose of utilizing the flowmeter, which is explained in detail in Flow Rate Measurement section, is to check the system's calibration regularly. Yet, the measurement is valid only for steady flows. Figure 3.1 shows the locations of three different pressure transducers; near the pump, aneurysm inlet, and aneurysm outlet. In this order of settlement, the aim of the pressure measurement at the pump outlet is to observe the flow pattern created by the pump. Additionally, the pressure transducer placed in the aneurysm entrance aims to monitor whether the flow pattern near the PIV data field is preserved. Finally, monitoring pressure at the outlet of aneurysm is for observing the pressure changes before and after the phantom. The details of the pressure measurement device are discussed in the Pressure Measurement section.

All the materials used in the experimental system have been selected, considering that they do not react with the working fluid. Unplasticized Polyvinyl Chloride (UH – PVC) is preferred for the connections of pressure transducers, while connections made of brass material are utilized when smaller and rigid connections are required.

The circulation in the system is driven by a computer-controlled gear pump combined with a servomotor, which is designed to imitate the pressure waveforms and physiological flow. The gear pump utilized to carry out the experiments (Dayton 4KHH8, Grainger, Inc., Lake Forest, IL) has 400 ml/s maximum continuous output flow rate capacity. Similar to the above discussion, all materials used in the pump are selected to avoid reactions with working fluid. The effect of downstream pressure on the output flow is minimal due to the positive displacement property of the gear pump. A triple-phase servo motor (Schneider electric BMH0702P16A2A) is implemented for driving the gear pump. A servo motor coupling is combined with pump shafts to prevent backlash while letting small angular and parallel misalignments.

An "offset" value is entered into the electric motor with the help of the PLC control system. The offset value presents the power input provided to the electric motor. For the "offset" value, calibration is done in two steps. The density of the working fluid is measured in ambient temperature, then flowrate is calculated from the weight of the filled bucket by keeping the time. The results of the aforementioned calibration process are presented in tabulated form in Table 5.

3.2   Aneurysm Model and Blood Mimicking Fluid

The experiments are conducted on the glass AAA model that is transparent, axisymmetric and has an elliptic structure in a streamwise direction. The pyrex glass model is produced by the glass molding technique, and it has "D/d = 2.5" dilation ratio, "L/d=4" elongation ratio, and "d=18.4 mm " inner diameter. The schematic of the model is provided in Figure 3.5. The ratios are determined by considering the studies of Salsac et al. (2006) and Bauer et al. (2019) [9],[67].
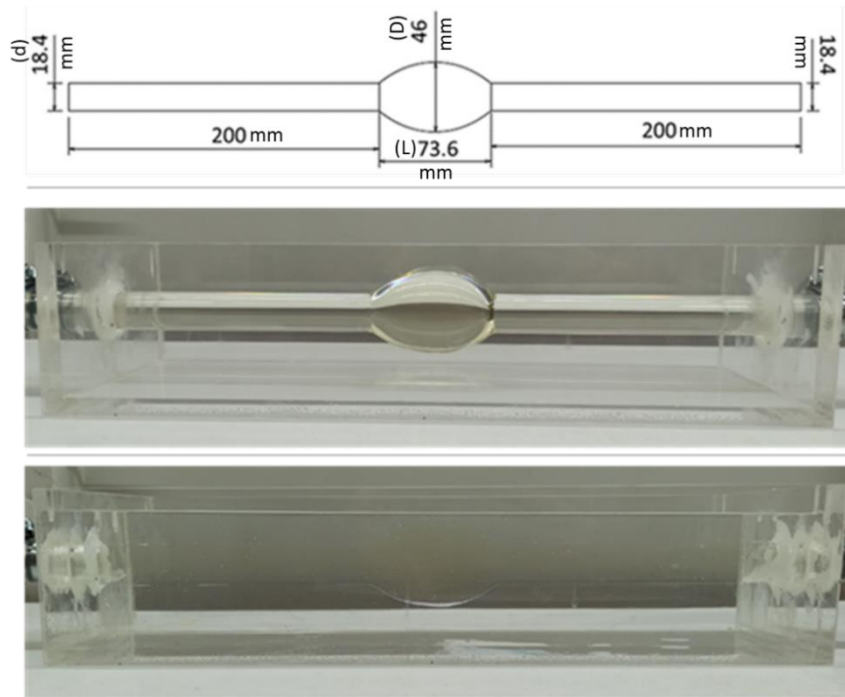
Figure 3.5: Aneurysm model - Above: Schematic of the model, Middle: Image of the model (Empty box), Below: Image of the model (The box full of working fluid)

Figure 3.5 includes the picture of the aneurysm model used in the laboratory. The glass aneurysm is used by placing it into a plexiglass box filled with working fluid to obtain optical advantages. To match the refractive index of glass and the working fluid, NaI and NaSCN are generally considered. Sample mixtures are created in the laboratory to observe the effects of both salts. Firstly, as can be seen in Figure 3.6 NaI mixture exhibits reddish coloring problems. Sodium Thiosulfate ($Na_2S_2O_3$) is also added to cure the mixture to overcome this problem [39]. Secondly, similar to the NaI, NaSCN also causes color change problems which results in yellowish color. However, the primary concern of NaSCN arises in contact with iron-based metals. When it comes into contact with iron-based metals, it damages the metal and turns the mixture color into a dark red. These NaSCN effects are undesirable for an experiment fluid whose optical properties are crucially important. Although the NaSCN does not give desired results with iron-based metals, it is observed that the materials such as aluminum, plastic, glass, brass are not affected. Additionally, the

46

fluid itself remains its transparent structure and does not experience coloration. Thus, the NaSCN is preferred as blood mimicking fluid since it is more available than NaI, and non-reactive materials are present in the experimental set-up.
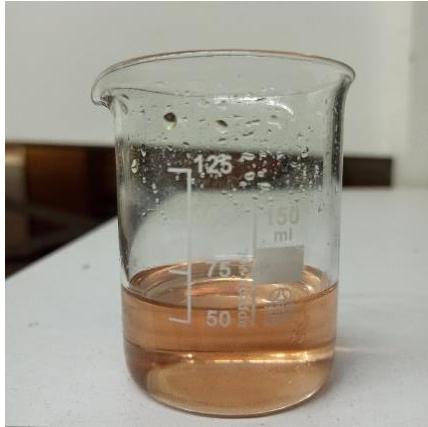
Figure 3.6: Colorization of NaI mixture

The mixture ratios used in the experiment are adjusted according to the non-Newtonian mixture, including NaSCN, suggested in Najjari et al. (2016) [40]. Since a Newtonian fluid is used in the current study, the mixture mentioned above is prepared without xanthan gum. The viscosity values that change with varying shear rates are provided in Figure 2.9 (plot 'b') from Najjari et al. 2016 [40]. Since the fluid used is Newtonian, it can be seen in Figure 2.9 (plot 'b') that the viscosity value is approximately equal to the value that the non-Newtonian viscosity curve is converged at high shear rates. The viscosity value of the fluid is also measured in the experimental set-up by using pressure transducers. Hagen-Poiseuille flow simulation is performed while staying in the laminar flow range. The pressure drop is measured with two pressure transducers at a distance of 5 meters from each other with the known fluid density (measured, $1310 \, \text{kg/m}^3$), pipe diameter, and flow velocity. Thus, the viscosity of the fluid is calculated. The fluid's dynamic and kinematic viscosity is measured as 0.012314 Pa.s and $9.4 \times 10^{-6} \, \text{m}^2/\text{s}$, respectively. Thus, it is observed that the measurement result gives the same output as in Figure 2.9 (plot 'b.')

3.3 Particle Image Velocimetry (PIV)

In this study, in order to obtain the velocity field, Particle Image Velocimetry is used. It is a non-intrusive, quantitative, optical flow measuring technique. Depending on the PIV type, the method provides a velocity field vector in two-dimensional or three-dimensional domains. In this study, planar PIV is utilized to obtain "u" and "v" velocity components in the mid-plane of AAA. The basic working principle of PIV is taking consecutive camera images of the flow field to trace the seeding particles, which are illuminated by a laser sheet. Obtained images are split into small pieces, which are coined as interrogation areas (IA). Hence, the output of PIV is the estimation of displacement vectors for each interrogation area (IA) by comparing the positions of the seeding particles in successive images. The entire flow field can be obtained by calculating the average velocity vectors. During the calculation process, an input taken from the user, Δt, which is the time gap between consecutive images, is used. By dividing the average displacements of particles by Δt, the average velocity vectors can be calculated for each interrogation area (IA).

TSI PIV is used as hardware to conduct the experiments on flow measurement, and Insight4G is utilized as software to collect the data for upcoming processes. The technical properties of the laser can be summarized as dual-pulsed, 15 Hz., Q-switched Litron Nano L200-15 200mJ Nd: YAG. The laser beam is transformed into a laser sheet with the cylindrical lens whose radius is -15 mm and the spherical lens whose focal point is 1000 mm. The lens combination is selected by taking the maximum possible velocity in the flow field into consideration. The reason behind the selection is to illuminate the particles properly and guarantee that the maximum seeding particles' displacement is within the laser sheet. Images are taken by a 4-megapixel (2032 x 2048) high-speed Complementary Metal Oxide Semiconductor (CMOS) camera, and the lens attached to the camera is Nikon AF NIKKOR 50mm f1.8. To synchronize the laser and camera according to the user-defined inputs TSI LaserPulseTM 610036 synchronizer is used.

The focus plane of the camera is adjusted to face the laser sheet passing the center of the aneurysm at a full 90-degree angle. The hit of the laser in the middle of the aneurysm is checked by both inspection and PIV camera image. In other words, since the largest cross-sectional area is obtained when the laser hits the midplane, checking the image for the largest cross-section is also a control method. The experimental set-up is explicitly shown in Figure 3.7.
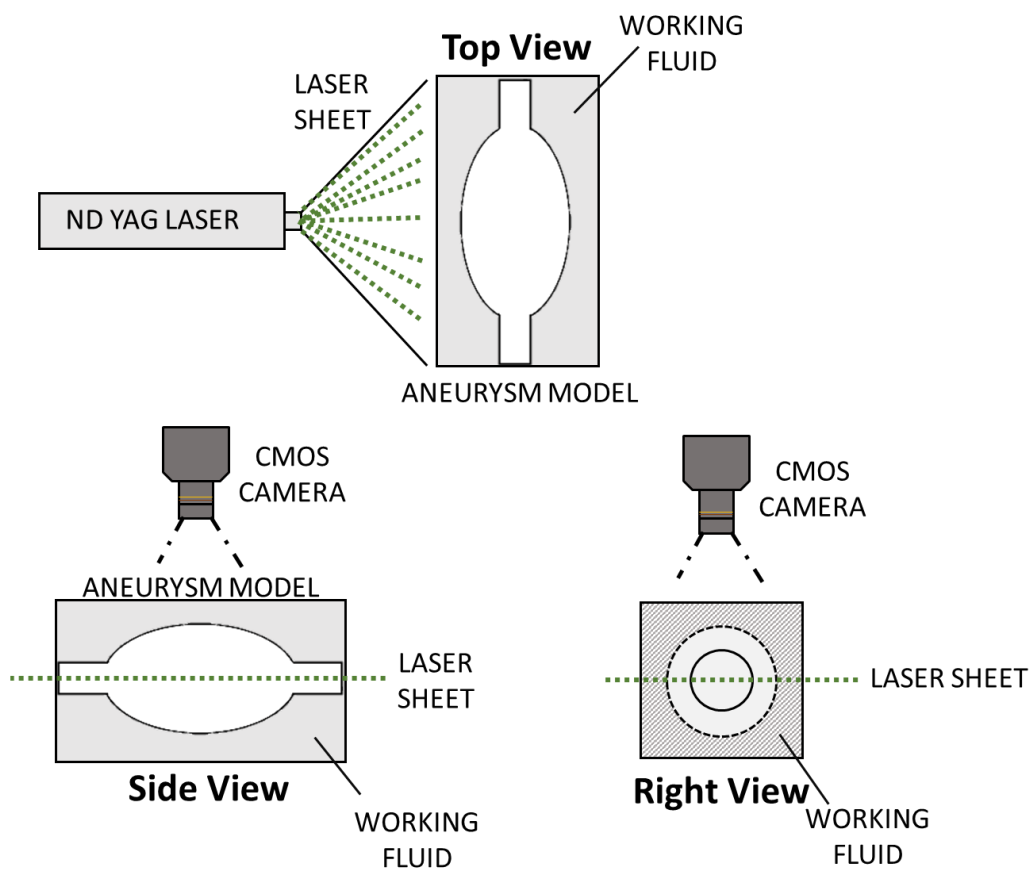
Figure 3.7: Schematics of laser and camera configuration

In this study, Dantec Dynamics Silver Coated Hollow Glass Spheres type 10 microns seeding particle is used. For each case, 100 pairs of images are taken and averaged; then, these raw images are processed by splitting the region of interest into the 32 x 32 square pixel interrogation area for whole field images and 64 x 64 square pixels for close-up images 50% overlap for both. This difference in interrogation area is because particles appear larger as they get closer to the image. In addition, close-up measurements give better results if the laser light is weaker due to the small diameters in terms of particle reflection. To accomplish the time-average velocity field, cross-correlation is carried out by utilizing Fast Fourier Transform (FFT) correlator for each pair of images.

After that, the velocity field data is subtracted from the Tecplot Focus as an ASCII format and then is post-processed for the streamlines, velocity contours, and vorticity contours with Paraview 5.9.0. For the wall shear stress calculation, MATLAB 2021a is used, which is explained in detail in the upcoming WSS Calculation from measured data (MATLAB) section.

Additional to the whole-field study, close-up PIV studies are also conducted. Two additional pieces of equipment are used together with the camera to conduct the close-up experiments: macro extension tubes and close-up filters (diopters.) An extension tube, basically a tube that is placed between the camera and the lens. As a result, additional distance is gained between the lens and the camera sensor. The additional distance allows the camera to get closer to the subject resulting in greater magnification.

On the other hand, diopters are special optical gadgets placed in front of the camera. They are simply magnifying glass that is placed between the subject and the lens. With the diopters, focal length decreases; as a result, the spatial resolution of the camera increases. The image of both macro-extension tube and diopter can be seen in Figure 3.8.

Figure 3.8: Image of the diopter (left) and macro extension tube (right)

3.3.1   WSS Calculation from measured data (MATLAB)

In the wall shear stress (WSS) calculation, the first thing to consider is the wall location. The wall location is extracted by visual inspection from the PIV image that is shown in Figure 3.9. Wall seems as a stratum instead of a single line due to the reflection, seeding particle accumulation, and laser thickness. Hence, taking the middle of the apparent wall area can be counted as one of the best approaches because the area appearing in PIV contains all the infinitesimal planes in this wall cloud [76].
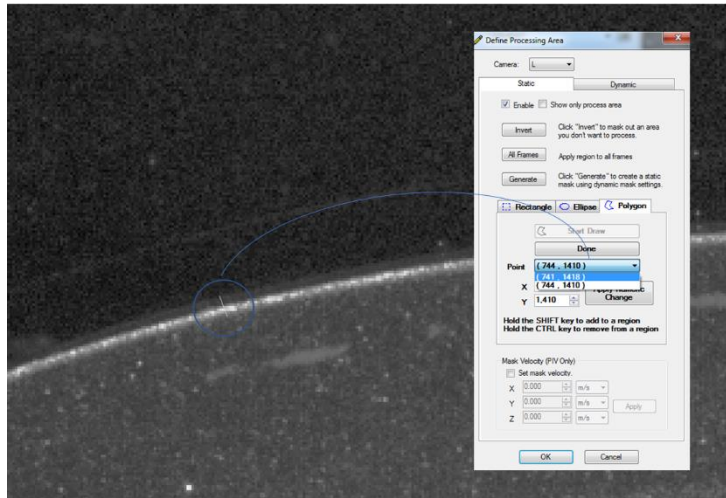
Figure 3.9: Wall location extraction from INSIGHT 4G Software

In the MATLAB code, after extracting the wall location as a pixel value, it is transformed to the location by using the spatial calibration value of the camera. The number of extracted data from PIV by visual inspection ranges from 30 to 40 points. However, for WSS estimation, more points are needed for accurate calculation. Even though it varies according to aneurysm geometry, approximately 10000 ± 1000 points are used. Using the code, the cubic spline fit is applied to the extracted points of the wall, then 10000 points are extracted with equal intervals on the x-axis over the spline. After the wall points are prepared, null and masked-out data in the region of interest are eliminated. Figure 3.10 presents the elimination process of data points for both close-up and whole field approaches.

The points in the remaining data pools are matched with the wall points on the wall-normal. Matched data can be the first discrete closest data point on the wall-normal, or it can be taken up to the 5th point, according to the parameters explained in the next section. Schematics of the match between the wall and data points can be seen in Figure 3.10 for both close-up and whole field.
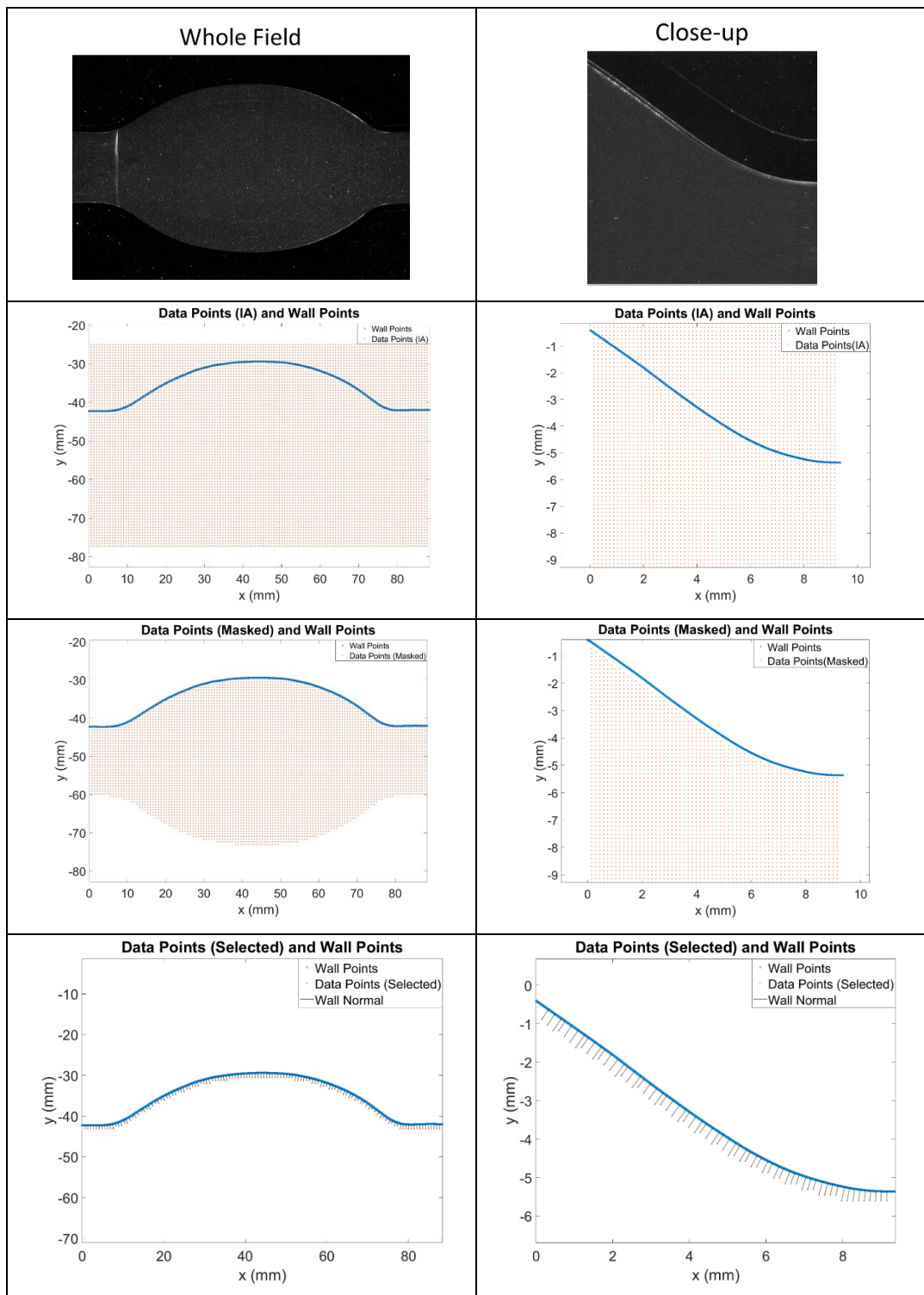
Figure 3.10: Data point and initial wall point matching process for both close-up and whole field studies

Up to this point, the discussion continued over the discrete data. If the linear fit is not preferred (single data approach), the discussion continues over the velocity vectors behind the initial data points selected for high-order velocity fits. Since the subjected geometry is not flat, that is, the discrete data order is not always aligned with the normal of the wall; data needs to be converted to a continuous form. The "scatteredInterpolant" command of the MATLAB2021a is used to achieve this. After the initial data point is selected, PIV grid size movements are made on the normal of the wall for each new data point, as shown in Figure 3.11. For every initial point and data behind it, different velocity profile fits are applied, which is detailed in the next section.
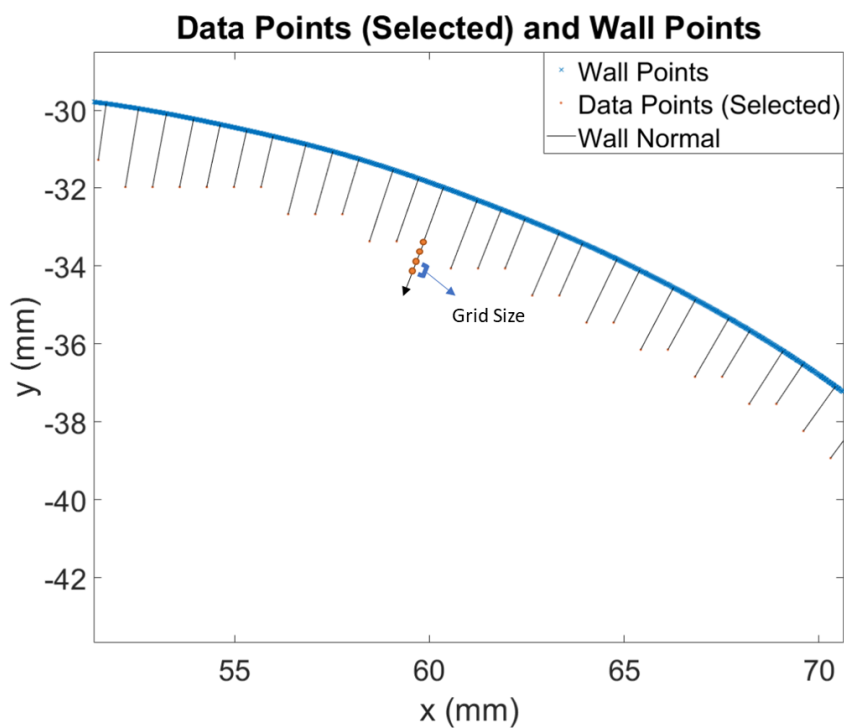
Figure 3.11: Schematic of multiple point usage for velocity fit profile

3.3.2   Calculation Parameters

In order to calculate wall shear stress properly, four different parameters are considered, which are listed below:

- Velocity Profile Fit Selection
- Grid Size Selection
- Wall Location Selection
- Initial Data Point Selection

1) Velocity Profile Fit Selection

There are five different velocity profile fit approaches are considered. These are linear, second-order polynomial, third-order polynomial, point-to-point (wall independent), and cubic spline fit velocity profile.

a) Linear velocity profile:

The linear fit is the simplest approach that can be implemented, but underestimation can be observed as moving away from the wall. A schematic of the linear velocity profile fit can be seen in Figure 3.12.

➢ V (y) = ay + b

- 1.Point → Wall Point ("0" Velocity)
- 2.Point → 1.data point
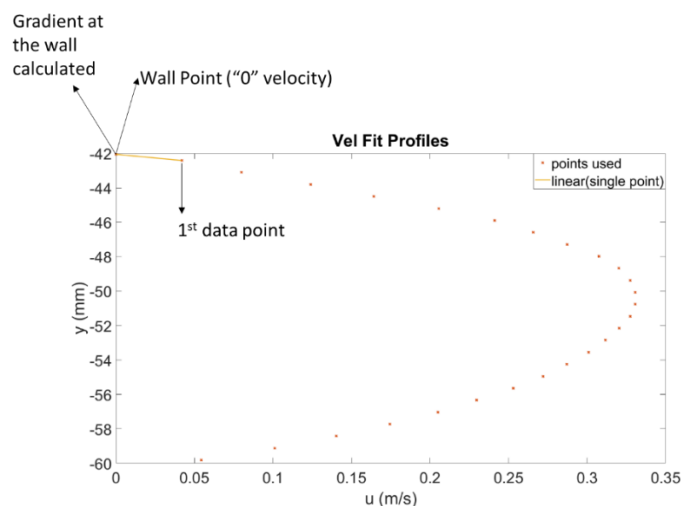
Figure 3.12: Schematic of the linear velocity profile

b) Second-order polynomial velocity profile:

Schematic of the second-order polynomial velocity profile can be seen in Figure 3.13.

➤ $\underline{V\,(y) = ay^2 + by + c}$

- 1.Point → Wall Point ("0" Velocity)
- 2.Point → 1.data point
- 3.Point → 2.data point
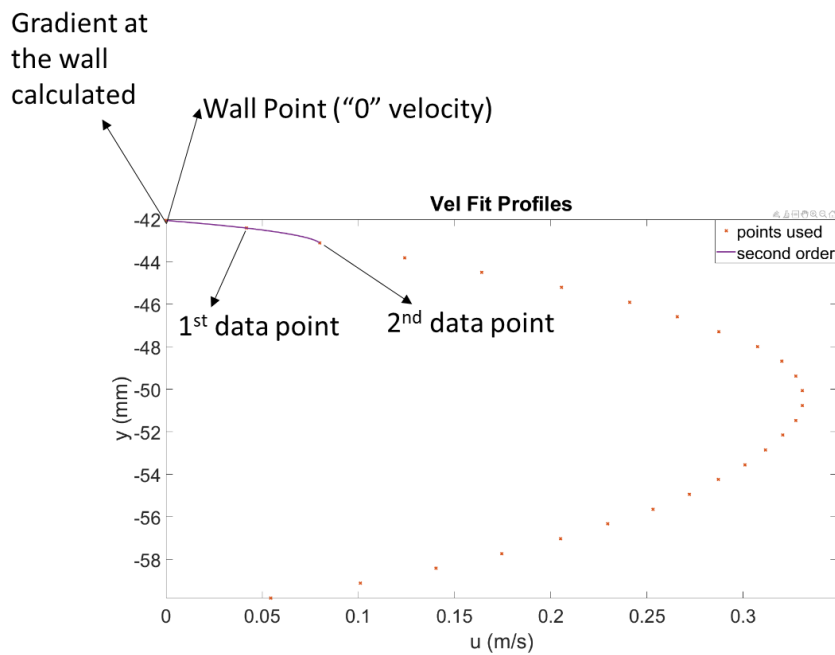
Figure 3.13: Schematic of the second-order polynomial velocity profile

c) Third-order polynomial velocity profile:

Schematic of the third-order polynomial velocity profile can be seen in Figure 3.14.

➤ $\underline{V\,(y) = ay^3 + by^2 + cy + d}$

- 1.Point → Wall Point ("0" Velocity)
- 2.Point → 1.data point
- 3.Point → 2.data point
- 4.Point → 3.data point

56
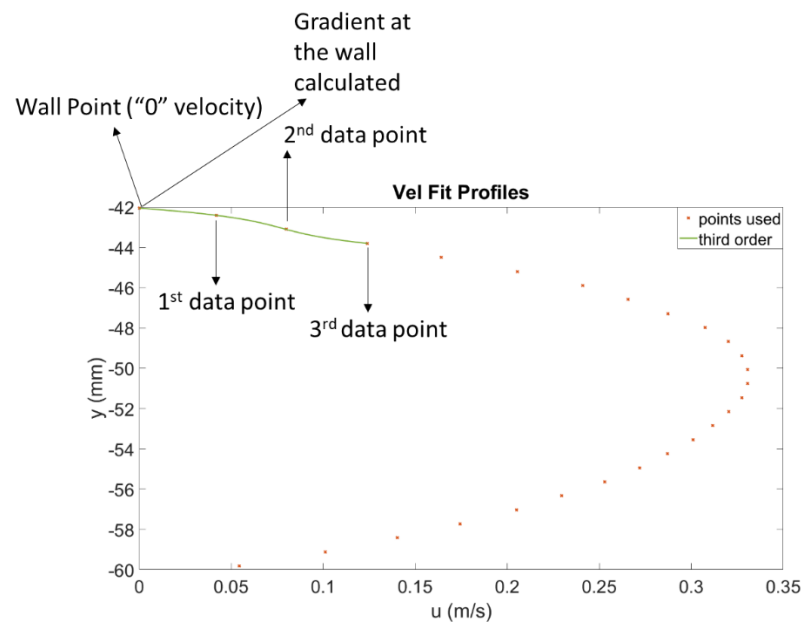
Figure 3.14: Schematic of the third-order polynomial velocity profile

d) Point-to-point (wall independent):

This method is linear extrapolation based, which means that the wall location information is not needed. Although the method is advantageous for wall location errors, it gives inaccurate results, especially when wall-normal is not aligned with the scattered data points or grids [52]. A schematic of the point-to-point velocity profile fit can be seen in Figure 3.15.

➢ V (y) = ay + b

- 1.Point → 1.data point
- 2.Point → 2.data point
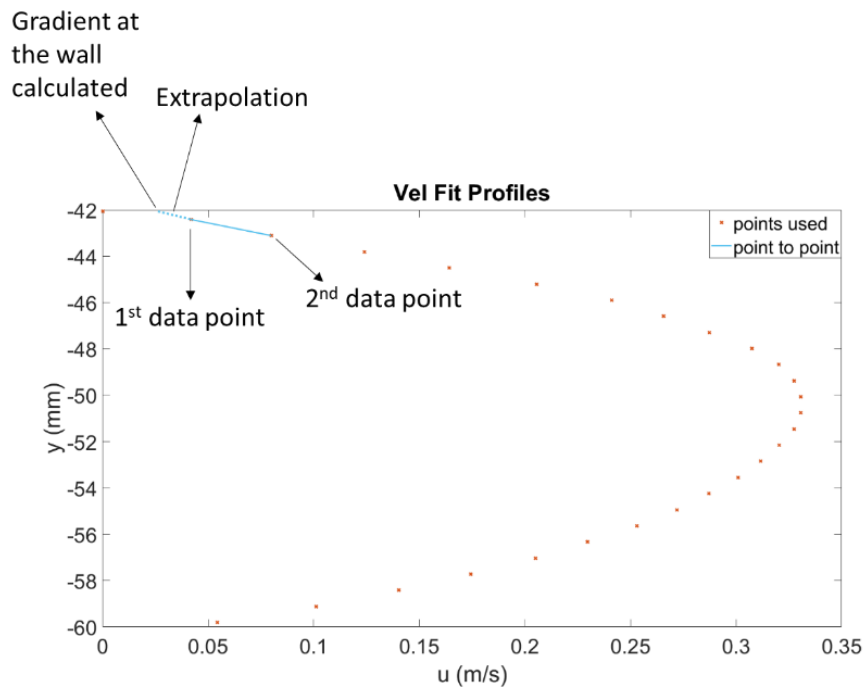
Figure 3.15: Schematic of the point-to-point velocity profile

e) Cubic spline velocity profile:

The cubic spline is a piecewise third-order polynomial; this structure offers more robust fitting, especially for the complex flows [54],[55]. A schematic of the cubic spline velocity profile can be seen in Figure 3.16.

➢ V (y) = piecewise third-order polynomials

- 1.Point → Wall Point ("0" Velocity)
- 2.Point → 1.data point
- 3.Point → 2.data point
- 4.Point → 3.data point
- 5.Point → 4.data point
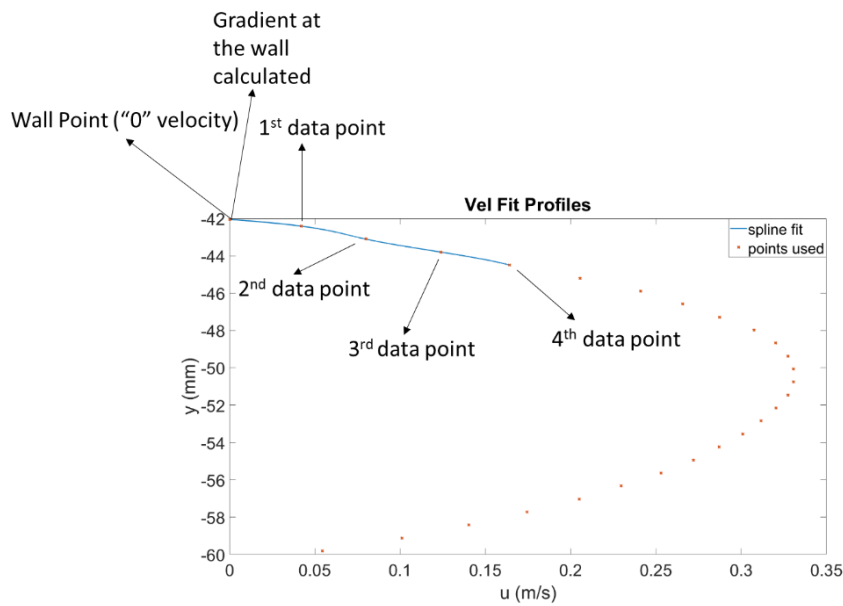
Figure 3.16: Schematic of the cubic spline velocity profile

2) Grid Size Selection

The distance between data points is already PIV grid size for straight, circular pipe calculation because discrete data points are used. The grid size is around 0.15 mm for close-up studies and 0.7 mm for whole field studies. There is no interpolated data usage for the circular pipe calculation because data points are aligned with the wall-normal, as shown in Figure 3.17; there is no need for interpolated data.
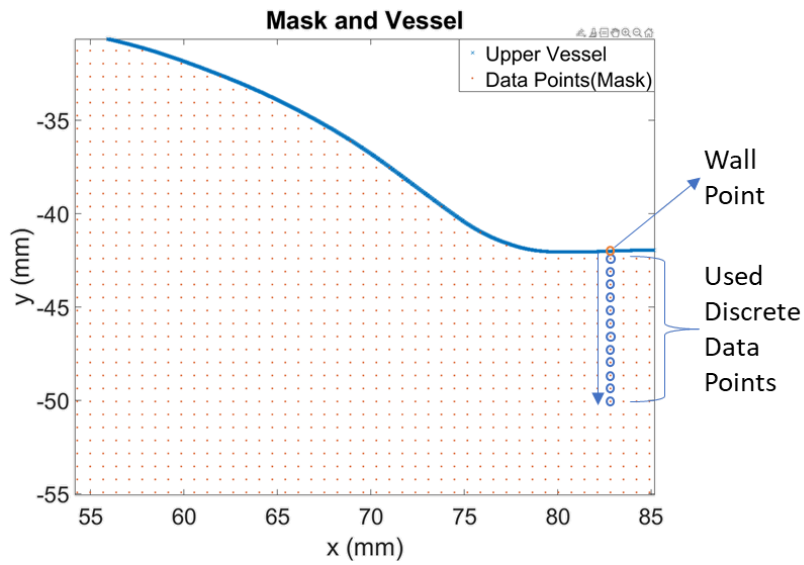
Figure 3.17: Schematic of the discrete data usage

For the bulge portion, since the PIV data is not aligned with the wall-normal in general, interpolated data is needed. Distance between data points is chosen as PIV grid size. As explained in the previous section, scattered data points are interpolated using the "scatteredInterpolant" command in MATLAB. Only the first data is discrete PIV data; after points are selected from the interpolated region. The presentation of data selection can be seen in Figure 3.18.
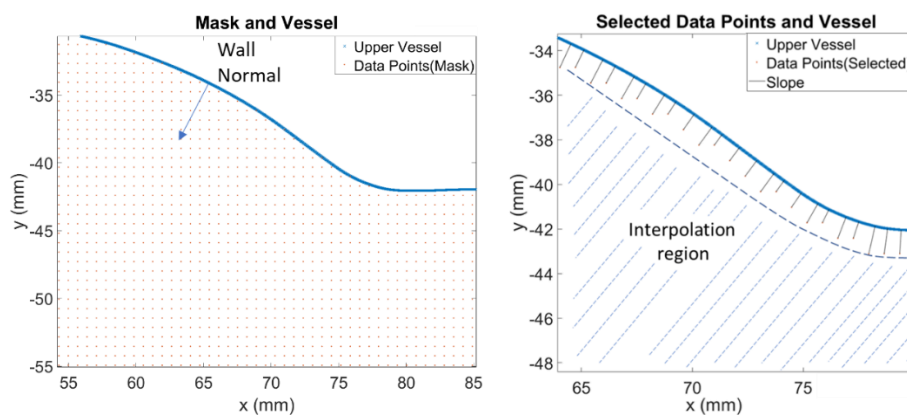
Figure 3.18: Schematic of the interpolated data usage

60

3) Wall Location Selection

The Wall location is selected as the middle of the wall beam, as shown in Figure 3.19. The same approach is followed in Nguyen et al. (2010) study [76].
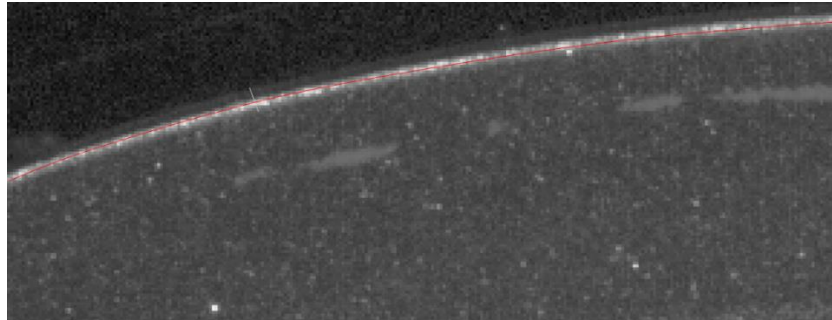
Figure 3.19: Schematic of the wall location

4) Initial Data Point Selection

Because of the reasons like overestimation of the velocity and data quality, some points close to the wall are disregarded. Below there is a presentation of the data usage for different options on the spline fit approach. It can be the first, second, third, fourth, and fifth point closest to the wall. Schematics of 1st and 3rd initial point selection are shown in Figure 3.20.
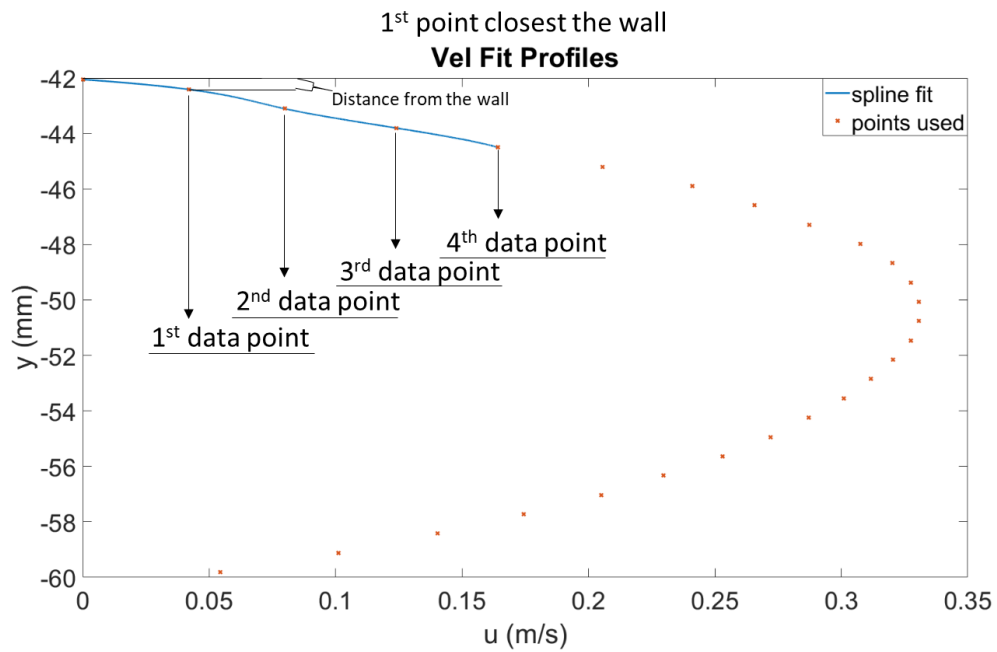
Figure 3.20: Schematics of the initial data point (1st and 3rd)

After calculating the WSS distributions with the methods mentioned above, the WSS-related metrics detailed in the WSS Parameters section are calculated. These are Time Average Wall Shear Stress (TAWSS), Oscillatory Shear Index (OSI), Wall Shear Stress Gradient (WSSG), Time Average Wall Shear Stress Gradient (TAWSSG), and Temporal Wall Shear Stress Gradient (TWSSG). "TAWSS" presents the time average of the WSS value in time-varying patterns. The "OSI" metric shows the direction change of WSS. Low WSS - High OSI regions are associated with intimal hyperplasia and disruption of vascular structure. "WSSG" presents the spatial change of the WSS value over the aneurysm. "TAWSSG" shows the mean (in terms of time) of the spatial variation in time-varying patterns. The spatial gradient is responsible for the thickening and hardening of the vascular cells and fat and mineral deposition. These occasions are indicative of the vessel rupture location. Finally, "TWSSG" allows WSS to be examined in terms of time change instead of a spatial gradient in time-varying patterns. The metric changes result in endothelial cell proliferation (rapid increase in the number of cells.) Equations of the metrics are shown in Table 3.

3.4   Pressure Measurement

The pressure measurements are conducted using two Mesens MPS.420 and a WIKA ECO-1 brand pressure transducer. The whole acquisition system consists of four components: pressure transducer, power supply, the connection between power supply and data acquisition (daq) card, and the connection between the pressure transducer and daq card. A 24V external electric source feeds the electronic system integrated into the power supply 'MCH – 305D – II'. A 12-bit NI PIC-6024E - 16 channel DAQ card is employed to digitize the raw data. WIKA brand Eco-1 has a maximum pressure measurement limit of 2.5 bar, and its accuracy value is defined as $\pm 1\%$. Additionally, the accuracy value of the Mesens MPS.420 device is $\pm 0.5\%$, and its maximum pressure measurement limit is recorded as 4 bar. Consequently, ± 25 mbar and ± 20 mbar span values are observed for WIKA ECO-1 and Mesens

MPS.420, respectively. Both devices are counted as two-wire type pressure transducers with 4-20 mA output current. For increasing the measurement accuracy, a resistor of 470 ohms is placed to the connections. The pressure transducers are calibrated according to the pressure values read by bourdon gage for specific offset values (flow rates) on the same T connection. Table 4 presents the calibration values of the pressure measurement tools.

Table 4 Calibration table of pressure transducers

Offset	Flowrate (ml/s)	Bourdon Gage (bar)	PT1 (MPS.420_1) (ampere)	PT2 (MPS.420_1) (ampere)	PT3 (WIKA ECO-1) (ampere)
0	0.00	0.12	4.40	4.44	4.63
10	5.67	0.17	4.42	4.45	4.64
20	19.64	0.21	4.71	4.74	5.13
30	33.61	0.32	5.15	5.18	5.83
40	47.58	0.45	5.68	5.71	6.68
50	61.55	0.60	6.29	6.31	7.68
60	75.52	0.77	6.95	6.97	8.70
70	89.48	0.95	7.68	7.68	9.84
80	103.45	1.48	8.47	8.46	11.08
90	117.42	1.90	9.32	9.28	12.38
100	131.39	2.43	10.22	10.18	13.83

3.5 Flow Rate Measurement

Flowrate measurement is carried out using Sea YF-S201 plastic turbine flow meter. A plastic turbine meter is a pulse-type measurement tool, the turbine inside it has a magnet. The faster the turbine rotates; the more total pulse values are read in a certain

period. For turbine-type flowmeters, the number of pulses received per a certain volume is coined as "k-factor," and it gives an idea about the capacity of the flowmeter. The flowmeter is only used to check the offset vs. flowrate calibration in steady measurements due to the low k-factor of the flowmeter. A low k-factor is not an obstacle for steady measurements because the accuracy of the total pulse/time can be improved by increasing the measured time interval, but a similar interpretation cannot be made for physiological (time-varying) flow. Even in steady flow at the flowrate values studied in the laboratory, the acquirement of consistent data begins with a time interval of approximately 4 seconds. Thus, it is not possible to capture a physiological flow varying between 1-3 seconds. Being enabled to read only the steady flow rate can be tolerated by pressure measurements and the velocity values obtained from the PIV data. The calibration data of the flowmeter with the working fluid is summarized in Table 5.

Table 5 Calibration table of flowmeter

Offset	Empty Weight of the Bottle (gr)	Total Weight Measured (gr)	Net Weight (gr)	Time (sec)	Volume (m^3)	Flowrate (ml/s)	Frequency Measured (Flowmeter) (Hz)
10	154.4	1196.3	1041.9	173.18	0.0008	4.5926	1
20	158.8	2648.1	2489.3	94.93	0.0019	20.0172	9.5
30	161.2	3475.5	3314.3	74.26	0.0025	34.0695	16.8
40	161.2	4040.3	3879.1	61.58	0.0030	48.0861	24
60	161.5	4980.1	4818.6	48.59	0.0037	75.7012	36.5
80	160.6	4585.3	4424.7	32.71	0.0034	103.2600	46.5
100	162.2	2910.4	2748.2	16	0.0021	131.1164	57.3
Measured Working Fluid's Density = 1310 kg/m^3							

3.6   Input Parameters

Two non-dimensionless input parameters exist in this study; these are Reynolds Number (Re) and Womersley Number (α).

Formulae of the Reynolds number can be seen in Equation (3.1):

$$Re = \frac{\rho\, u\, d}{\mu} \qquad\qquad (3.1)$$

Where:

ρ : density of the working fluid (kg/m^3)

u : average velocity inside the circular pipe before the aneurysm (m/s)

d : diameter of the circular pipe (m)

μ : dynamic viscosity of the working fluid (Pa.s)

In this study, the characteristic length is taken as the diameter of the aorta, not bulge diameter, to match with the normal human body, the Reynolds number calculating accordingly. As the characteristic velocity magnitude, averaged velocity at the inlet of the aneurysm is calculated and accepted. Dynamic viscosity and fluid density are taken from the blood, mimicking fluid's properties measured in the laboratory. ($\rho = 1310$ kg/m^3, $\mu = 1.2314$ x 10^{-2} kg/m.s)

In biofluid studies, in order to define the oscillatory or pulsatile flow, Womersley Number (α) is used. It presents the ratio between unsteady inertial forces to viscous forces. High Womersley numbers mean high oscillator behavior in the flow. It is observed that disturbance in fluid path highly correlated with the increase in Womersley number [77]. Equation of the Womersley number is written below in Equation (3.2):

$$\alpha = R \sqrt{\frac{\omega \rho}{\mu}} \qquad\qquad (3.2)$$

Where:

ρ : density of the working fluid (kg/m^3)

R : radius of the circular pipe (m)

μ : dynamic viscosity of the working fluid (Pa.s)

ω : frequency of periodicity (rad/s)

In the present study, a single Womersley number is used in experiments. Physiological pattern time in the experiment is 1.1 seconds, and frequency is calculated accordingly. Other parameters are accepted as in the Reynold Number calculations.

3.7   Experimental Matrices

During the study, two different flow patterns are examined: steady and physiological flows. To obtain the velocity field, particle image velocimetry (PIV) equipment is employed in this experiment. Measurements are conducted by flowmeter and pressure transducers to check the flow rate and flow pattern. In addition to the flowmeter and pressure transducer, PIV is also used to check the flow rate. For the steady flow, measurements are taken for Re=300 and Re=900. Close-up measurements are conducted for steady flow to observe whether the spatial resolution increase changes the WSS results. After the inferences made from the steady measurements, phase averaged data are taken from 10 different physiological points in a single physiological flow type. The details of the flow pattern are presented in Flow Pattern Determination with PIV and Pressure Measurement section, and it has $Re_{mean} \approx 300$ and Womersley=7.17 values. For the whole

experiment process, the same AAA model and blood-mimicking fluid are used. The only variable is the flow pattern. The summary of the experimental matrices is given in Table 6 below.

Table 6 The table of experimental matrices

Flow Type	Whole Field PIV	Close – up PIV
Steady	Re=300	Re=300
Steady	Re=900	Re=900
Physiological	$Re_{mean} \approx 300$ Womersley=7.17 (for 10 different phase)	-

CHAPTER 4

RESULTS AND DISCUSSIONS

In this chapter, PIV results are detailed. First, steady flow circular pipe results of the whole field and close-up studies are compared with the analytical results. In that comparison, different initial data points and different velocity profile fits are considered in order to understand the best approach for the calculation. Secondly, the bulge region is examined using the circular pipe PIV–analytical comparison results. (Vel fit profile, data points, etc.) Thirdly, close-up studies at the distal neck where negative and positive peaks are observed are compared with the whole field studies. Finally, flow fields in the aneurysm region are detailed in order to connect the WSS and WSS parameter variations with those characteristics.

Spatial resolution is one of the most important criteria while measuring the WSS. To check whether the spatial resolution is adequate for the whole field image experiments, the equipment (diopter and macro extension tube) mentioned in the PIV section for close-up images is used to increase spatial resolution. Employing the combination of diopter and macro extension tube, pixel/mm value has improved ten times. Since the close-up studies are conducted with 64x64 pixel interrogation area instead of 32x32 pixels, grid sizes approximately change five times. In other words, while the distance between the grids is around 0.7 mm in whole field experiments, it is around 0.15 mm in close-up studies. Since the working logic of using this equipment is to reduce the focal length, it is necessary to physically approach the place where the image is taken with the camera. In close-up experiments, the camera sees an area of 9.3 mm x 9.37 mm, so the whole bulge field that requires approximately 90 mm x 90.7 mm cannot be examined in a single frame. As presented in Figure 4.1, it is necessary to proceed step by step, conduct separate experiments

for each region, and combine them. From inlet to outlet, 10 images should be taken and merged in total. This process prolongs the total experiment time considerably.
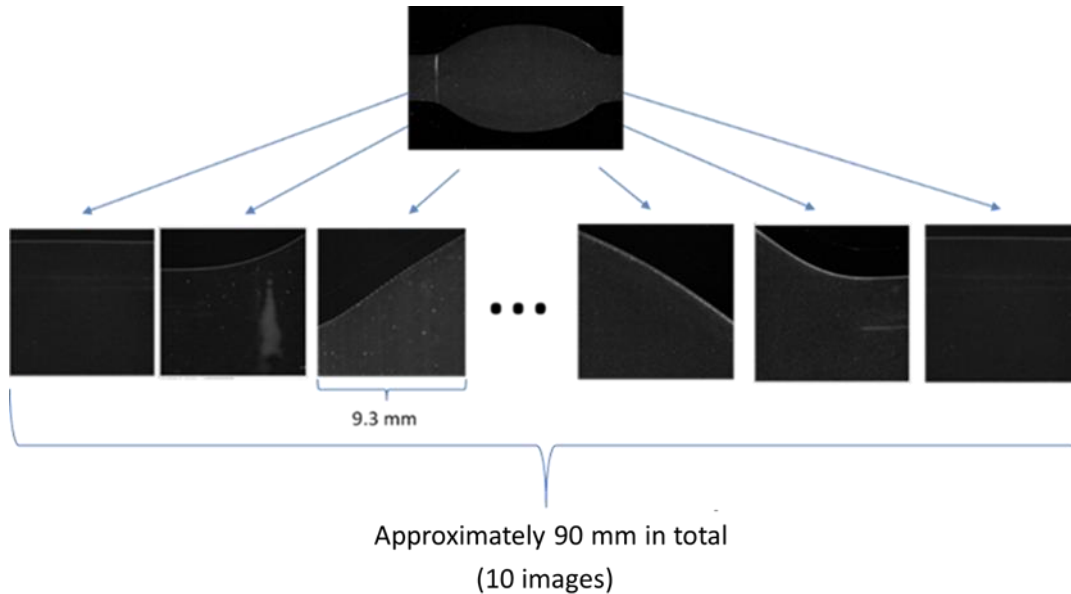
Figure 4.1: Close-up images of the bulge for the whole field

4.1 Analytical Calculations for Steady Flow

For laminar, fully developed and steady flow (constant cross-section circular pipe flow) types are generally called Hagen-Poiseuille flow, or shortly Poiseuille flow. The schematic presentation of the Poiseuille flow is provided in Figure 4.2 [78]. The analytical solution is available for the velocity profile of these flows; in other words, WSS can be calculated with the help of an analytical solution. The analytical solutions are used to understand which PIV velocity data overestimates or which velocity fit model best approximates the WSS, and the results are compared with each other. The comparison needs to be done on a straight, circular pipe with optical access. For this reason, the straight portion just before the aneurysm is examined.

70
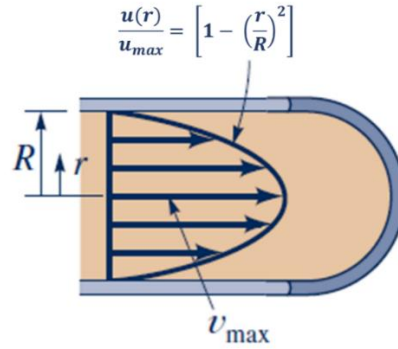
Figure 4.2: Schematic of Hagen-Poiseuille flow [78]

The velocity profile equations of the abovementioned flow conditions (steady, laminar, circular pipe) are given in Equation (4.1):

$$u(r) = u_{max} \left[1 - \left(\frac{r}{R}\right)^2\right] \text{ and } u_{max} = 2\, u_{mean} \tag{4.1}$$

Where :

* $u(r)$ = u velocity with respect to radial direction (m/s)

* r = variable for radial direction

$(r = 0\,/\,c$enter of the circular pipe, $\;r = 9.2\,mm\,/$ maximum$)$

* R = radius of the circular pipe = $9.2\,mm$

* Re = Reynolds number = $\dfrac{u\,(2\,R)\,\rho}{\mu}$

* $u_{mean} = \dfrac{Re\,\mu}{(2\,R)\,\rho}$

Blood Mimicking Fluid Properties: (are measured at $T = 22 \pm 2\,°C$)

- ρ = density of the fluid = $1310\,\dfrac{kg}{m^3}$

- μ = dynamic viscosity of the fluid = $1.2314\,x\,10^{-2}\,\dfrac{kg}{m\,s}$

As a final step, Equation (4.2) is applied:

$$\tau_w = \mu \ \frac{d(u(r))}{d(r)} \ \text{where} \ \frac{d(u(r))}{d(r)} = \ -2 \ u_{max} \ \frac{r}{R^2} \qquad (4.2)$$

When the calculations are completed, analytical results can be seen in Table 7 :

Table 7 The table of analytical results of WSS for Re=300 and Re=900

Re Number	Wall Shear Stress (Pa)
Re = 300	0.82
Re = 900	2.46

4.2 Steady Flow

4.2.1 Straight Pipe

Before moving on to the "Bulge" portion, calculations are conducted to examine the results of the velocity fit methods as mentioned in the Calculation Parameters section and compare them with the analytical WSS result. Figure 4.3 shows the examined parts for the parameter comparison for both Re=300 and Re=900 cases. The difference and the advantage of the straight pipe portion compared to the bulge part is that obtained discrete velocity vectors can be used directly. Since the velocity vectors are aligned with respect to the wall-normal, interpolated velocity vectors are not needed. While calculating the WSS, the data column in the pipe presented in Figure 4.3 is taken for both whole field and close-up studies. There is a small contraction zone due to the manufacturing method and seeding particle accumulation on the side of the straight pipe close to the bulge, as shown in Figure 4.3; by taking the column presented, that part is avoided. As a wall location, the middle of the beam is taken, and as grid size, since discrete data are used, PIV grid size is applied. Table 8 includes WSS results and their deviations from the analytical solution with different initial data points and velocity profiles for the straight, circular pipe at

Re=300 and Re=900. Also, Table 8 includes grid size and distance of initial data points information for the whole field and close-up studies.
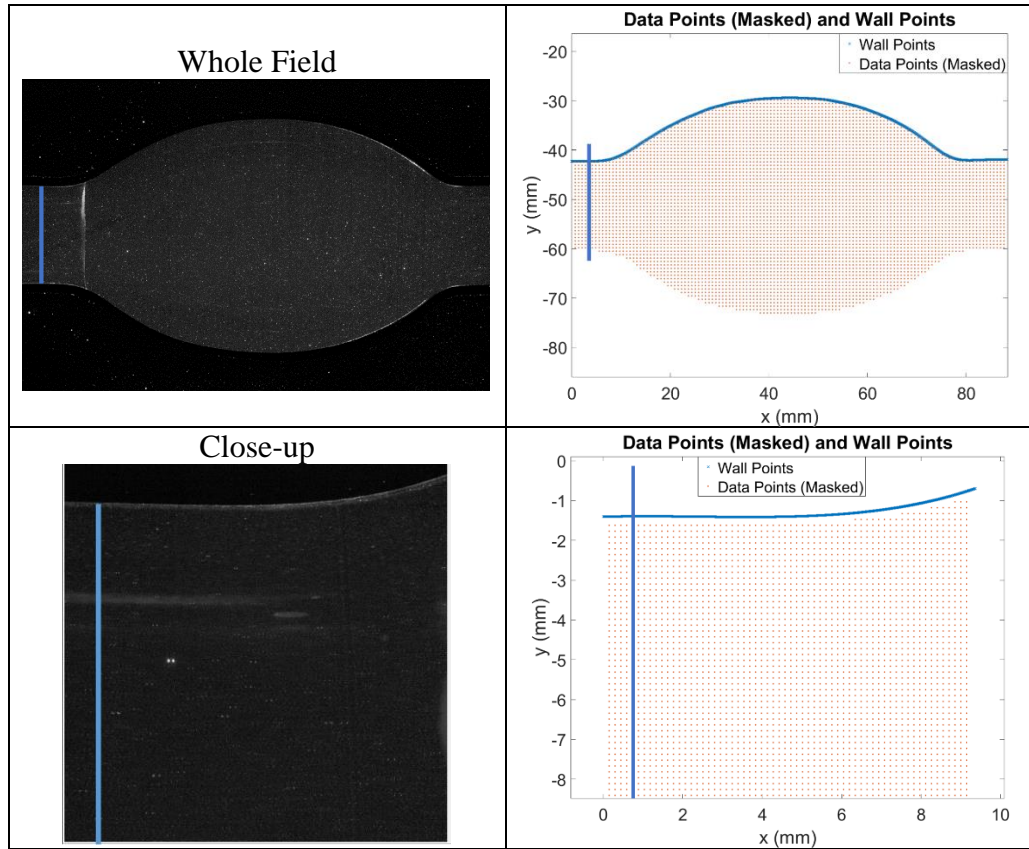
Figure 4.3: Straight portion of the bulge where data is taken

Table 8 Table of WSS values for different initial points and velocity fit models

Initial data vs. Vel. profiles (Mag. in 'Pa')	Re=300, Close-up (grid size = 0.15 mm)						Re=900, Close-up (grid size = 0.15 mm)				
	1st data	2nd data	3rd data	4th data	5th data		1st data	2nd data	3rd data	4th data	5th data
Linear (Deviation from analytical solution)	0.96	0.84	0.85	0.88	0.88		4.30	3.20	2.74	2.73	2.70
	17%	2%	4%	7%	7%		75%	30%	11%	11%	10%
2nd order poly. (Deviation from analytical solution)	1.09	0.81	0.76	0.9	0.92		5.89	4.35	2.76	2.85	2.97
	33%	-1%	-7%	10%	12%		139%	77%	12%	16%	21%
3rd order poly. (Deviation from analytical solution)	1.24	0.87	0.55	0.84	0.96		7.00	6.30	2.60	2.57	3.10
	51%	6%	-33%	2%	17%		185%	156%	6%	4%	26%
Point to point (Deviation from analytical solution)	0.71	0.87	0.97	0.86	0.82		1.62	1.59	2.71	2.58	2.38
	-13%	6%	18%	5%	0%		-34%	-35%	10%	5%	-3%
Spline (Deviation from analytical solution)	1.28	0.92	0.88	0.82	0.96		7.09	6.88	2.60	2.48	3.07
	56%	12%	7%	0%	17%		188%	180%	6%	1%	25%
Distance from the wall (mm)	**0.16**	**0.30**	**0.45**	**0.60**	**0.75**		**0.22**	**0.36**	**0.51**	**0.66**	**0.81**

Initial data vs. Vel. profiles (Mag. in 'Pa')	Re=300, Whole Field (grid size = 0.7 mm)						Re=900, Whole Field (grid size = 0.7 mm)				
	1st data	2nd data	3rd data	4th data	5th data		1st data	2nd data	3rd data	4th data	5th data
Linear (Deviation from analytical solution)	1.44	0.93	0.87	0.83	0.81		4.12	2.62	2.32	1.96	2.00
	76%	13%	6%	1%	-1%		67%	7%	-6%	-20%	-19%
2nd order poly. (Deviation from analytical solution)	1.70	1.02	0.99	0.90	0.95		5.81	3.24	2.94	2.39	2.61
	107%	24%	21%	10%	16%		136%	32%	20%	-3%	6%
3rd order poly. (Deviation from analytical solution)	1.88	1.05	1.10	0.81	0.71		7.26	3.56	3.34	2.39	2.34
	129%	28%	34%	-1%	-13%		195%	45%	36%	-3%	-5%
Point to point (Deviation from analytical solution)	0.67	0.78	0.71	0.73	0.63		0.92	1.70	1.52	1.44	1.26
	-18%	-5%	-13%	-11%	-23%		-63%	-31%	-38%	-41%	-49%
Spline (Deviation from analytical solution)	1.94	1.04	1.15	0.82	0.63		7.70	3.59	3.42	2.47	2.22
	137%	27%	40%	0%	-23%		213%	46%	39%	1%	-10%
Distance from the wall (mm)	**0.36**	**1.05**	**1.75**	**2.45**	**3.15**		**0.77**	**1.46**	**2.15**	**2.83**	**3.51**

The closest result to the analytical solution (Re=300 – WSS =0.82 Pa / Re=900 – WSS=2.46 Pa) can be selected as 3rd order polynomial or spline fit (4-point) by taking 4th closest data point as an initial data point when both Re=300 and Re=900 cases are interpreted. After it is determined that the 4th initial data is appropriate, the 5th data is also examined. Since the 5th data deviates more from the analytical solution and is further away from the wall, the 4th initial data selection is supported. Moving away from the wall is not preferable, which is discussed in WSS Result section. Although their grid sizes are different, both approach (close-up and whole field) gives the same initial data point number, that is, the accurate results are obtained at the different distances according to the wall. For close-up, the average initial point distance of 0.63 mm, and for whole-field, an average distance of 2.64 mm gives an accurate result. Therefore, this difference between the two methods cannot be explained directly with spatial resolution. It can be explained by the overestimated and bias data occurrence, especially near the non-constant high velocity gradient region in PIV calculations [50],[51]. The velocity profile result is consistent with the thesis study of DiCarlo et al. (2018), who used a 4-point spline fit in the PIV WSS study for the vessel [31], and with Van Ooij et al. (2015) who stated that spline fit provides more robust fitting [55]. WSS distribution in the bulge section is presented by utilizing spline fit. Still, initial data point selection can be different caused by the gradient change at the bulge portion because bias data occurrence near the wall is related to the non-constant, high velocity gradient [51]. That is checked by comparing different initial point approaches for both close-up and whole fields studies.

4.2.2   Bulge

PIV is applied to the region seen in Figure 4.4 below. For steady flow, the experiment is conducted for two different Reynold Number (Re) values. It is examined that how the increase in Re affects the WSS distribution. Firstly, the flow field is analyzed and interpreted with contours like "u velocity," "v velocity," "Velocity Magnitude

(Vel_Mag)," and "Vorticity" for Re=300 case. Secondly, the WSS distribution on the bulge is extracted with the specified parameters, and it is examined how it connects to the flow characteristics inside. Lastly, with the WSS results, the Wall Shear Stress Gradient (WSSG) metric associated with aneurysm growth and rupture is calculated, and their distribution on the aneurysm is interpreted.
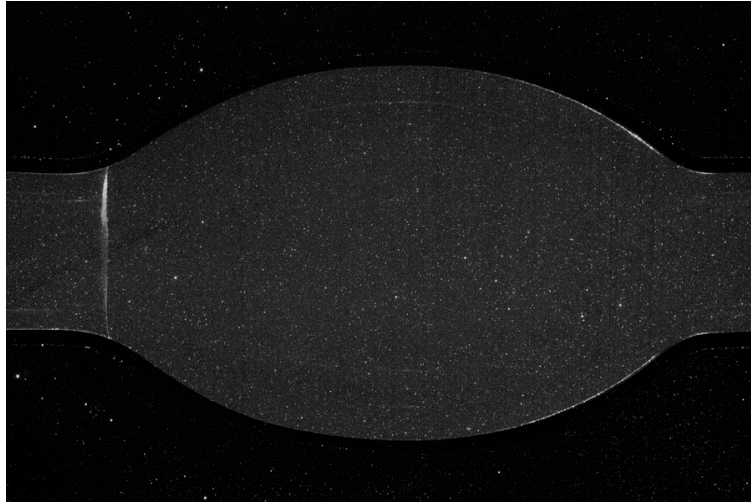
Figure 4.4: Whole field image taken from PIV

4.2.3 Flow Field

The typical flow characteristic of the abdominal aortic aneurysm is jet flow in the middle and weak recirculation part surrounding the jet flow. Flow recirculation bases on the separation created by adverse pressure gradient occurring due to the sudden increase in the cross-sectional area of the aneurysm [79]. The reattachment region is formed at the distal edge of the recirculation zone, which begins with the separation at the proximal edge. As shown in Figure 4.5, this basic characteristic is observed in the Re=300 case. Figure 4.5 presents the "u vel," "v vel," "velocity magnitude (vel_mag)," "vorticity magnitude" contour and streamline for the Re=300 case.
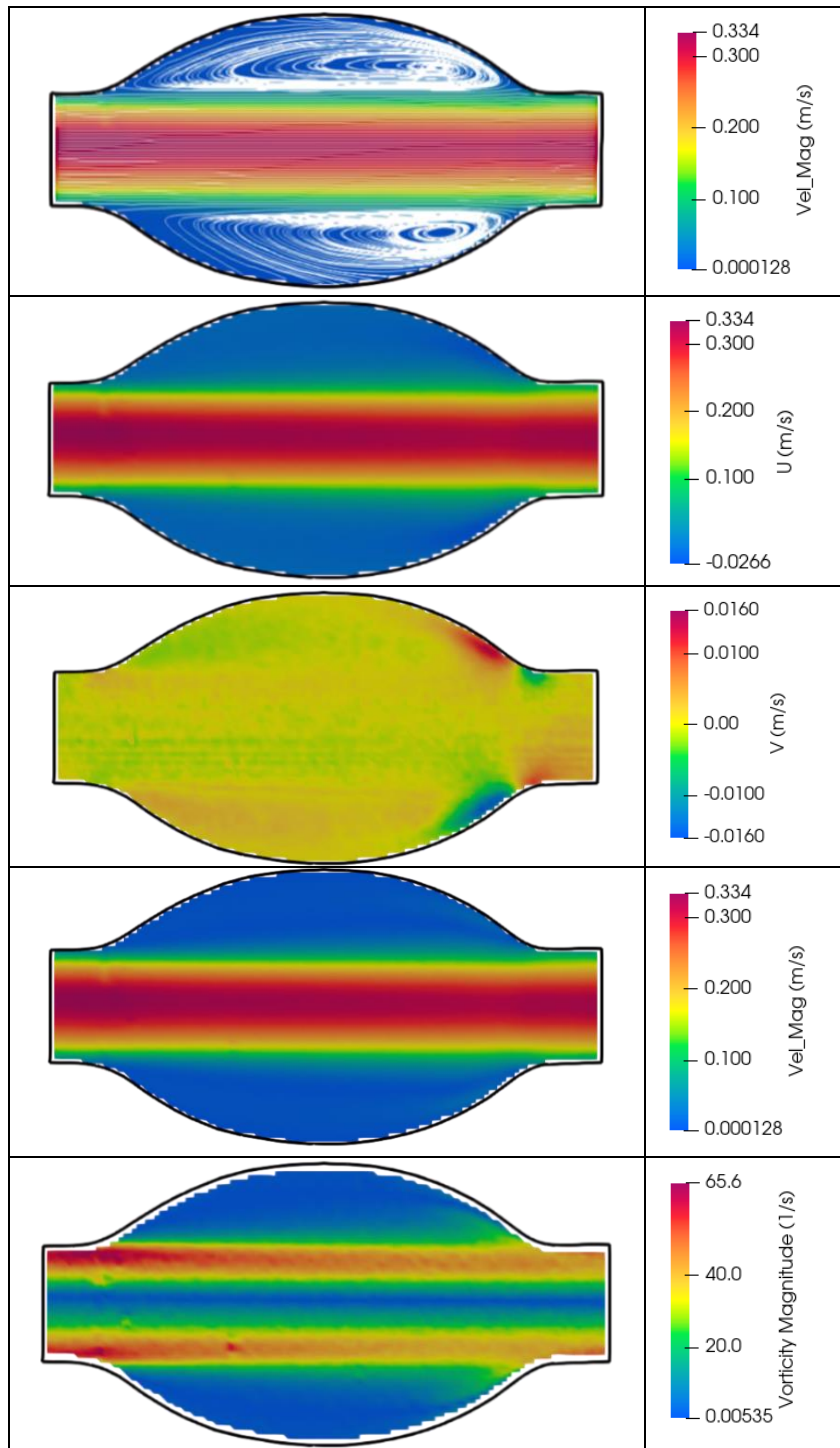
Figure 4.5: Streamline and contours of "u," "v," "vel_mag," and "vorticity
magnitude" for Re=300, Steady case

4.2.4   WSS Result

As mentioned in the circular pipe calculations, initial data point selection is reevaluated for the bulge portion because geometry and velocity gradient characteristics are different. Comparisons are carried out with spline fit velocity profile since it gives an accurate result in the circular pipe, and it is known as a robust method in the regions with complex flow [55]. Firstly, discussion is focused on the close-up studies that are advantageous in spatial resolution compared to whole field studies. Two plots containing WSS results for different initial data selection for both Re=300 and Re=900 cases are shown in Figure 4.6.
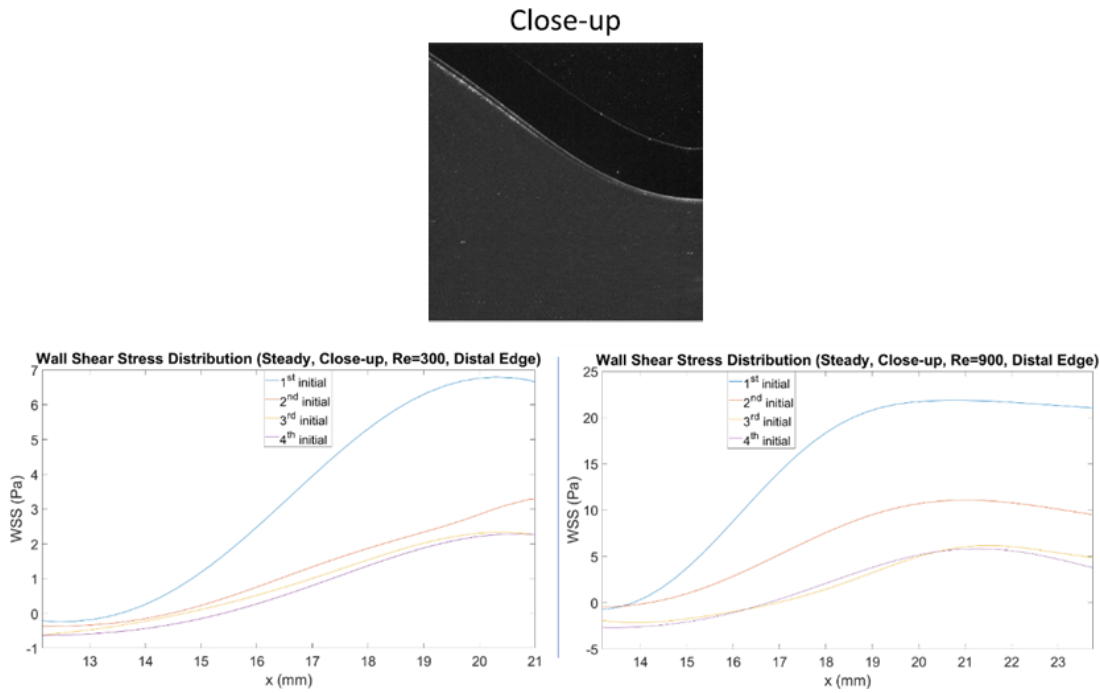
Figure 4.6: WSS distributions for close-up at distal edge (Re=300, Re=900, Different initial data points)

In the literature, the negative peak value ratio to the Poiseuille value at the distal edge is sensitive to geometry (dilation ratio, elongation ratio) and Re number. On the other hand, the ratio of positive peak value to the Poiseuille value disperse on a smaller interval which ranges from 1.7 to 2.9. Although this range includes various Reynolds numbers and aneurysm geometries, it is important for developing foresight to

understand the data in general [65],[67],[68],[80]. Table 9 below contains the positive peak values at the distal edge and their ratios to circular pipe WSS values for Re=300 and Re=900. When considering Table 10, the peaks of the 1st and 2nd initial data point methods give overestimated results while the 3rd and 4th initial data point methods highlighted in the table are in the expected range. The observation is coherent with the results obtained from the circular pipe that is the 4th initial data closest to the wall gives accurate results in the close-up studies.

Table 9 Distal edge positive peak results for different initial data points (Re=300, Re=900)

Close-up Results	Re300 WSS Peak (Pa)	Re300 Peak Ratio	Re900 WSS Peak (Pa)	Re900 Peak Ratio
Circular Pipe (WSS Value)	0.82	1	2.46	1
1st initial point (Positive Peak) (Distal Edge)	6.79	8.29	21.82	8.87
2nd initial point (Positive Peak) (Distal Edge)	3.29	4.01	11.10	4.51
3rd initial point (Positive Peak) (Distal Edge)	2.33	**2.84**	6.13	**2.49**
4th initial point (Positive Peak) (Distal Edge)	2.28	**2.78**	5.86	**2.38**

Since the results obtained using the 4th initial data point are validated by analytical solution in the circular pipe of the close-up study, 4th initial data usage is also selected for the WSS calculations in the bulge region, together with the discussions in Table

9. The whole field WSS results obtained by spline fit implementation at the distal edge for Re=300 and Re=900 are provided in Figure 4.7.
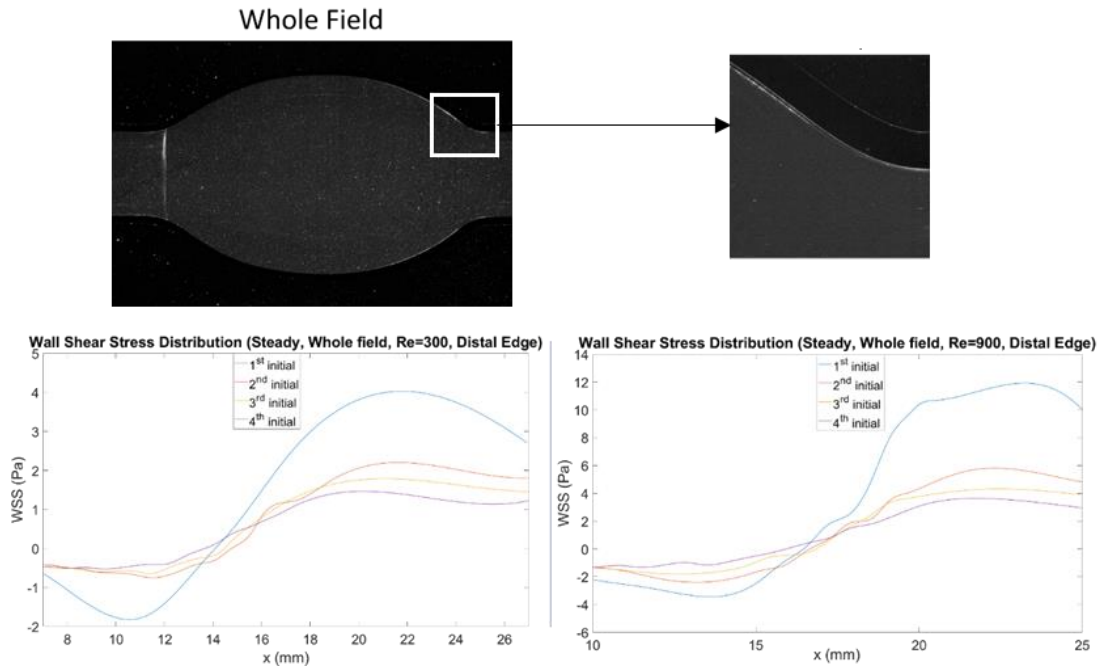
Figure 4.7: WSS distributions for the whole field at the distal edge (Re=300, Re=900, Different initial data points)

When Figure 4.6 and Figure 4.7 are compared, it can be concluded that the 4th initial point approach in the close-up study that validated for both straight pipe and bulge region is consistent with the 2nd initial data point approach in the whole field study. For comparison purposes, WSS distributions of the whole field (2nd closest data point) and close-up (4th closest data point) are presented in Figure 4.8.
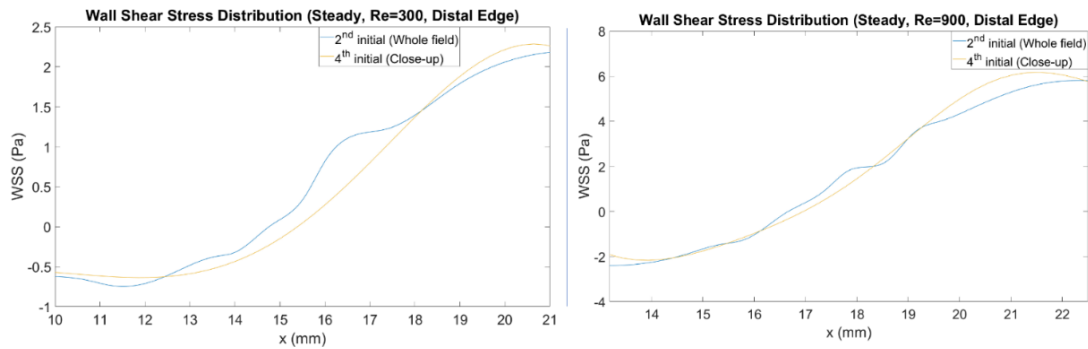
Figure 4.8: WSS distributions for close-up (4th initial) and whole field (2nd initial) at the distal edge (Re=300, Re=900)

Taking the 3rd or 4th data for the WSS calculations at the transition region from the bulge to the straight pipe can result in misleading calculations for whole field studies. As selected data moves away from the wall, the probability of observing misleading data increases for the highlighted region below in Figure 4.9, which is located in the recirculation zone but not far away from the main flow. For the current case, since the recirculation flow direction and main flow direction are opposite, a misleading situation may result in underestimated WSS calculation. Moreover, moving away from the wall results in an underestimation in general. As shown in the above part of Figure 4.9, the total distance used for the calculation is 3.1mm for the second initial data approach. This distance contains all the data points used for the spline fit; otherwise, only the first data distance to the wall is 1mm. On the other hand, the total distance used for the fourth initial point approach is 4.5 mm, and the initial data distance is 2.4 mm.
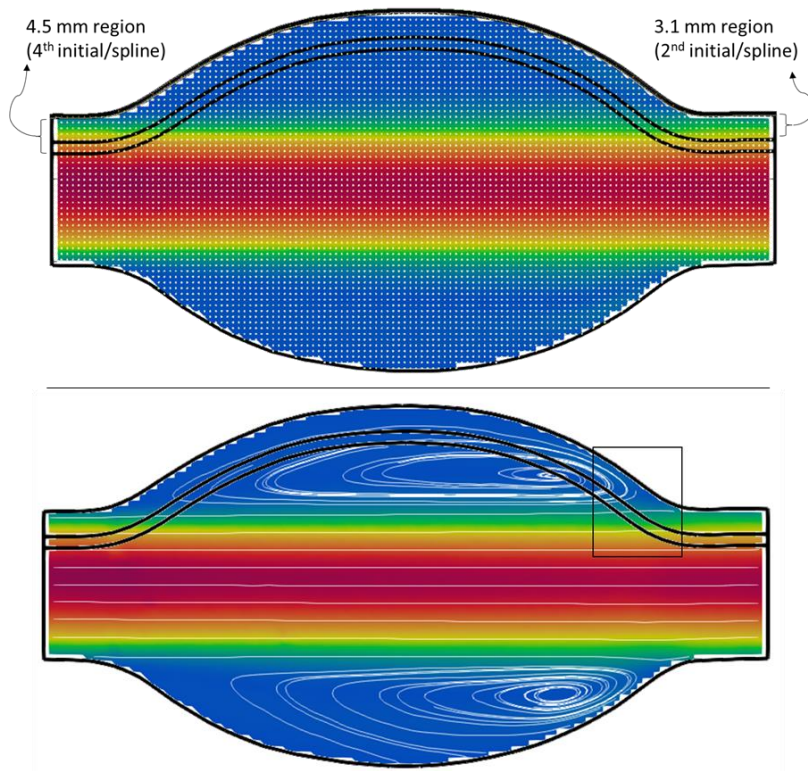
Figure 4.9: Presentation of data regions for different initial data points (Above: Data points, Below: Streamlines)

Figure 4.10 contains the WSS distributions for the whole field study with the 2nd and 4th initial point approach with spline fit model for the Re=300 and Re=900 cases.
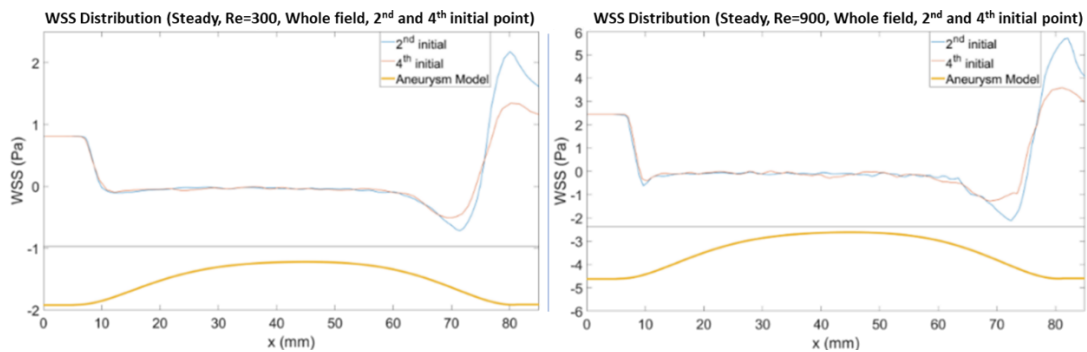
Figure 4.10: WSS distributions for the whole field with 2nd and 4th initial data points (Re=300, Re 900)

As shown in Figure 4.10, the 4th initial data point method gives underestimated results compared to the 2nd initial data point method for the whole field approach. While close-up (4th initial data point) gives similar results with the whole field (2nd initial data point), close-up studies require tremendous effort to conduct. Hence, further discussions are reported with the whole field (2nd initial data point, spline fit) approach rather than close-up (4th initial data point, spline fit). Figure 4.11 provides WSS distribution calculated by 2nd initial data point and spline fit for Re=300 and Re=900 steady cases.
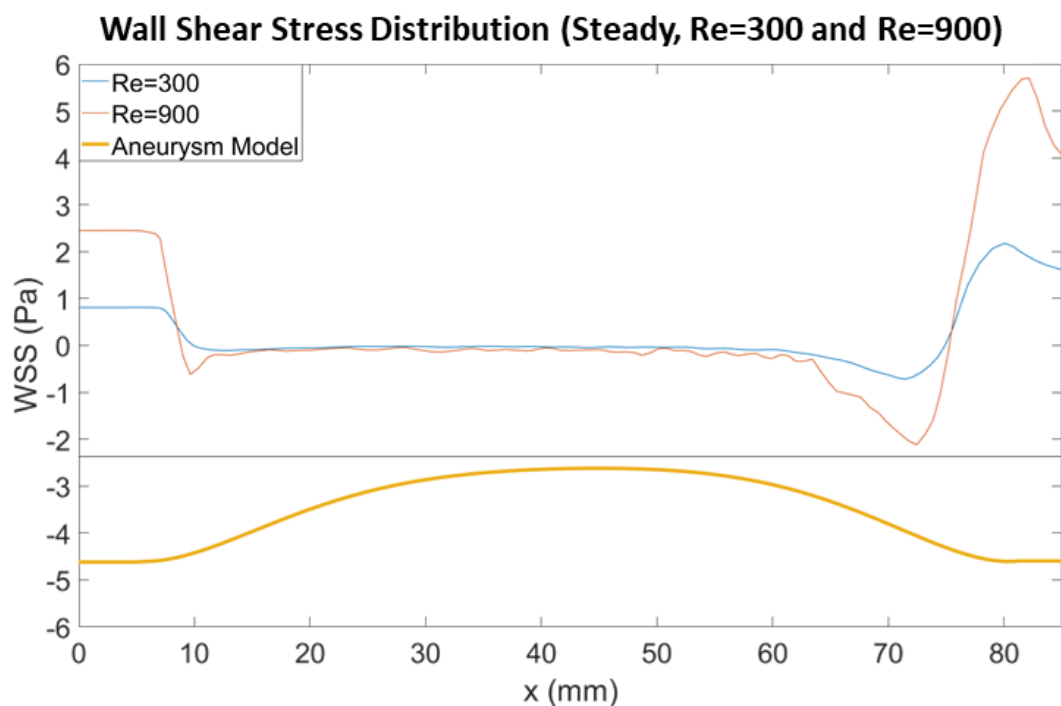
Figure 4.11: WSS distribution for Re=300 and Re=900 under the steady flow

Considering the general characteristics of abdominal aortic aneurysm, a negative peak at separation region, WSS values close to "0" in the recirculation region, and a negative and subsequently a positive peak are observed in the reattachment region for the case of steady flow. The important points in the WSS distribution are listed below:

- When the WSS graph is analyzed, it is realized that the wall shear stress value in the inlet tube is the same as the Hagen- Poiseuille flow [68].

- The WSS value rapidly declines to a negative value by passing through the "0" WSS at the separation point.

- After the separation point, WSS converges to close to zero value less than 20% of the entrance tube WSS magnitude.

- By passing the "0" value at the reattachment point, WSS experiences a negative and positive peak at the distal edge. The positive peak value at the distal edge is approximately 2.5 times the entrance tube value. This result is similar to the findings of Bluestein et al. (1996) and Budwig et al. (1993) studies [80],[68]

- After the positive peak, it proceeds to converge towards the Hagen-Poiseuille flow value.

- The peak values can be examined as a first step to analyze the WSS distribution with changing Re numbers. The negative peak value at the proximal edge is observed as "-0.1 Pa" in the case of Re=300 and "-0.62 Pa" in the case of Re=900. The WSS values in the recirculating region are difficult to see on the plot; they are around "-0.024 Pa" for Re=300 case and "-0.12 Pa" for Re=900 case. Finally, the negative and positive peaks at the distal edge are "-0.72 Pa" and "2.18 Pa" for Re=300, and "-2.12 Pa" and "5.7 Pa" for Re=900.

As a result, with the increasing Re, the proximal edge peak increased by 6.2 times, the recirculation zone value increased by five times, the distal edge negative peak increased 2.94 times, and the proximal edge positive peak increased 2.62 times. The rate of increase at the distal edge is half that of the proximal edge.

4.2.5   WSS Parameter

The steady flow does not have a time parameter; therefore, the metric that should be examined is Wall Shear Stress Gradient (WSSG), which is first proposed as a

hemodynamic indicator by Lei et al. (1995) [57]. It measures the spatial changes in surface forces/unit area, which has a high impact on the endothelial cells [64].

WSSG value is calculated with the central differencing approach, as stated in Equation (4.3). For the two points at the ends, the forward and backward difference approach is used.

$$WSSG = \left.\frac{\partial \tau_w}{\partial x}\right|_{x=x_i} = \frac{\tau_w(x_i + \Delta x) - \tau_w(x_i - \Delta x)}{2\Delta x} \tag{4.3}$$

When Figure 4.11 and Figure 4.12 are examined, peak WSSG values are encountered where the sign of the shear stress has changed. These locations are where the separation and reattachment occur, namely the proximal and distal edge of the aneurysm. In the middle of the bulge, WSSG values close to "0" are encountered due to nearly constant WSS values. When the effect of the Re number on the WSSG distribution is examined, there is a change in the WSSG peak values with an increase of more than two times in the peak value. Additionally, considering the WSSG graph individually, hemodynamic abnormality occurs mostly in the proximal and distal end of the aneurysm. Yet, the distal end is exposed to abnormality more.
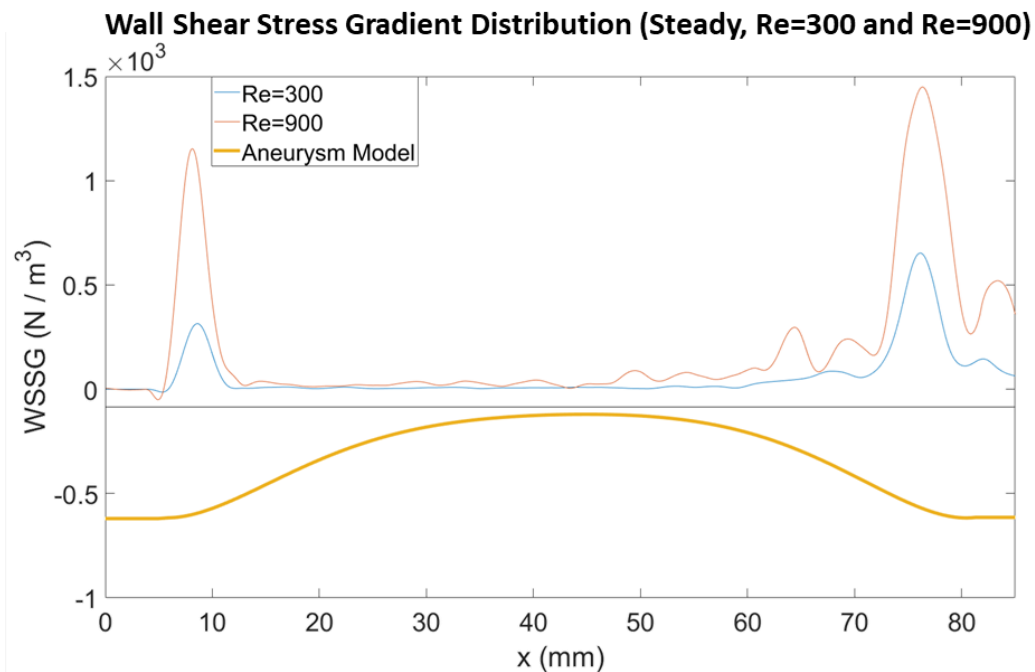
Figure 4.12: WSSG distribution for Re=300 and Re=900 under the steady flow (Absolute)

4.3   Physiological Flow

4.3.1   Flow Pattern Determination with PIV and Pressure Measurement

As described in the experimental set-up section, three measurement methods are used for flow rate measurement in the system. A plastic turbine flowmeter is used for steady flowrate measurement and pump calibration. Pressure transducer and PIV data are used to measure the flow rate in a time-varying pattern. PIV flowrate results are available in Figure 4.13. When the pressure patterns in Figure 4.14 are examined, it has been observed that they show similar behavior at the vessel inlet (PT2) and outlet (PT3) with flow rate measurements taken from the PIV. Considering all these factors, the pattern indicated by the PIV flow rate measurements is based on from now on. Experiments continue with this pattern since this pattern contains multiple accelerations/decelerations and peak points, allowing to discuss the characteristics observed in physiological flow.
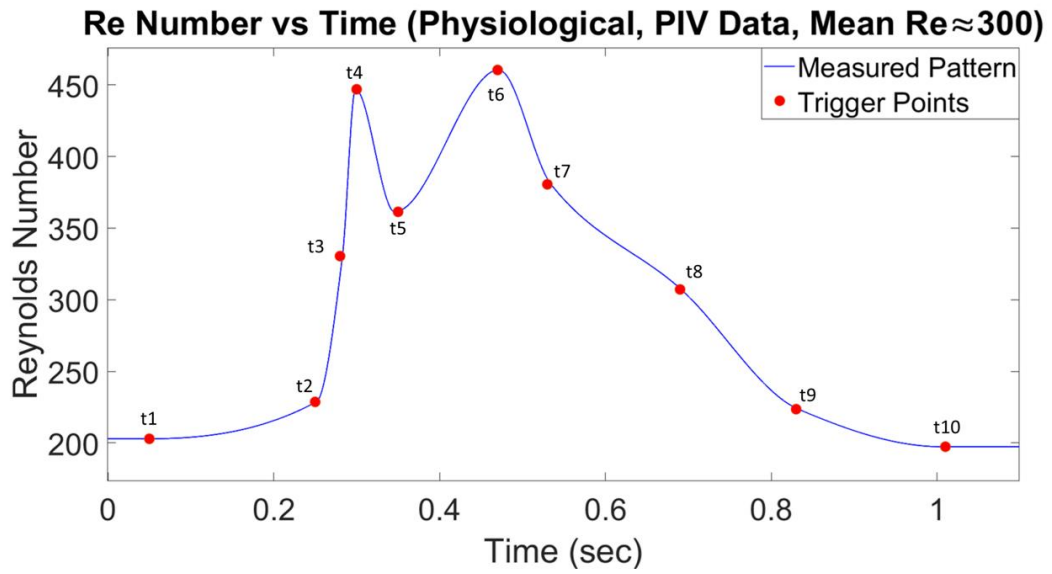
Figure 4.13: Physiological pattern obtained from PIV measurements ($Re_{mean} \approx 300$)
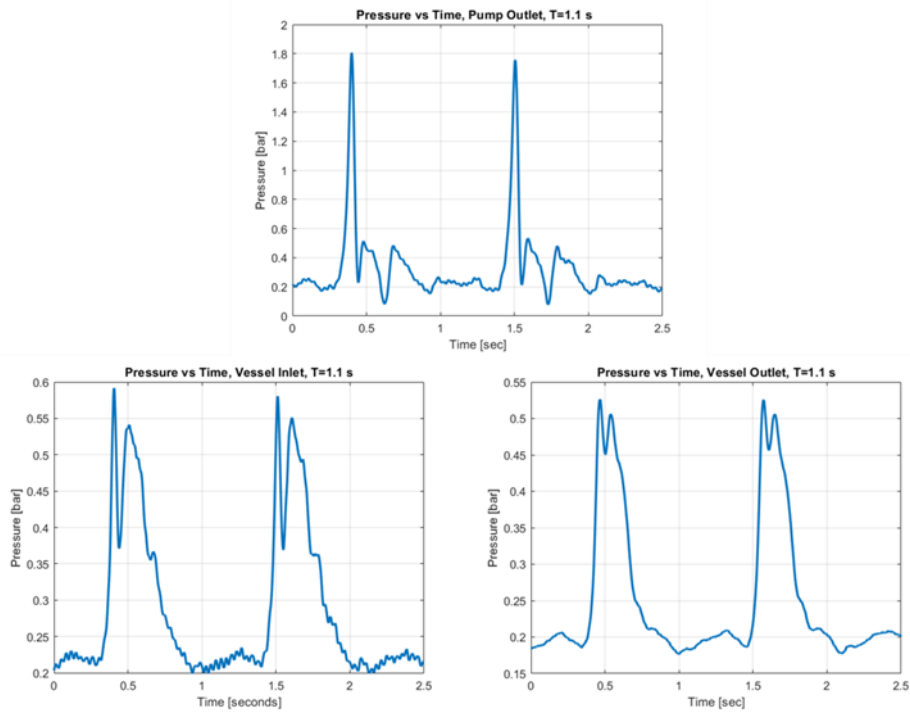
Figure 4.14: Pressure vs. time graph (Up: PT1, Left: PT2, Right: PT3)

4.3.2   Flow Field

Before moving onto the flow characteristics, it should be noted that the used geometry is not axisymmetric completely. Although a slight difference is observed in the steady flow, the difference is observed more clearly in a complex flow such as physiological flow. While interpreting the flow physics, both sides are interpreted considering cumulatively. Figure 4.15 includes streamlines colored by velocity magnitude/vector fields, and Appendix A. 1 includes "u" velocity / "v" velocity contours for the whole physiological phases examined. All of the discussions below about the flow mechanism are based on Figure 4.15 and Appendix A. 1.

When discussing the flow physics in physiological pattern, t2 is discussed first instead of t1 because the flow physics in t1 is the aftermath of the mechanism in t10. Thus, t1 is mentioned together with t10. Below, there is an investigation of the flow mechanism at time-varying pattern time by time:

- t2

While passing from t1 to t2, a slight acceleration occurs. Temporal acceleration defeats the negative pressure gradient caused by diverging the wall for the local proximal edge region and creates a flow attached to the bulge wall. Thus, the attached regular flow collapse with the counter-clockwise rotating circulation zone. However, since the acceleration level is low, it could not overcome the circulation zone.

- t3

As the acceleration increases dramatically, the volume of the attached flow in the bulge increases, and the vortex structure weakens.

- t4

For the case of the fourth-time instant, the flow on the top of the bulge becomes fully attached. Since this point is a peak, local acceleration already has changed into the negative rate and becomes "0", and the proximal edge of the flow is beginning to be disturbed.

- t5

The disturbance at the proximal edge, which starts with the local acceleration being "0", together with the deceleration (increase in the adverse pressure gradient), creates a counter-clockwise rotating vortex. The vortex region in the middle of the bulge, which is about to fade in t4, shows presence again. In addition, the attached regular region between the mentioned vortex region and the proximal edge is disturbed and loses its regularity.

- t6

Because of the acceleration, the counter-clockwise rotating vortex structure is convected to the distal edge with increase in volume. Moreover, it prevents the inlet flow from attaching to the wall. Still, the region in the bulge without circulation becomes regular and attached again to the bulge wall because of the convective acceleration.

- t7 - t8 - t9 - t10 - t1

Since the 2nd deceleration rate is not as high as the 1st deceleration, a second vortex structure has not been encountered. Instead, with the continuation of the deceleration rate in t8 and t9, it is observed that the aforementioned circulation region completely dominated the attached region and spread throughout the bulge. Furthermore, the pattern encountered in steady flow is observed, especially in t8. Although deceleration occurs, the circulation center is moved to the distal edge between t7-t9 since the flow moves forward. Simultaneously, the attachment point is moved forward and hits the distal neck at the t10, causing a small secondary, counter-rotating (clockwise) vortex region to form. This situation progresses further in t1 and takes on a structure with multiple attachment points and three vortexes. The pattern is repeated throughout the physiological flow. Moreover, attached regular flows caused by acceleration are at low speed in the bulge region like the circulation regions. Yet, as they are not clearly separated from the jet flow like the circulation regions, these regular flows cover a larger area and compress the high-velocity

region in the jet flow. To illustrate, the jet flow region is flat despite the complex multi-vortex structures in time t1, but the attached flow structures in t4 compress the high-velocity zone in the jet flow from the middle of the bulge. In addition, the attached region, which collides at the distal edge in t6, compresses the jet flow on the distal edge.
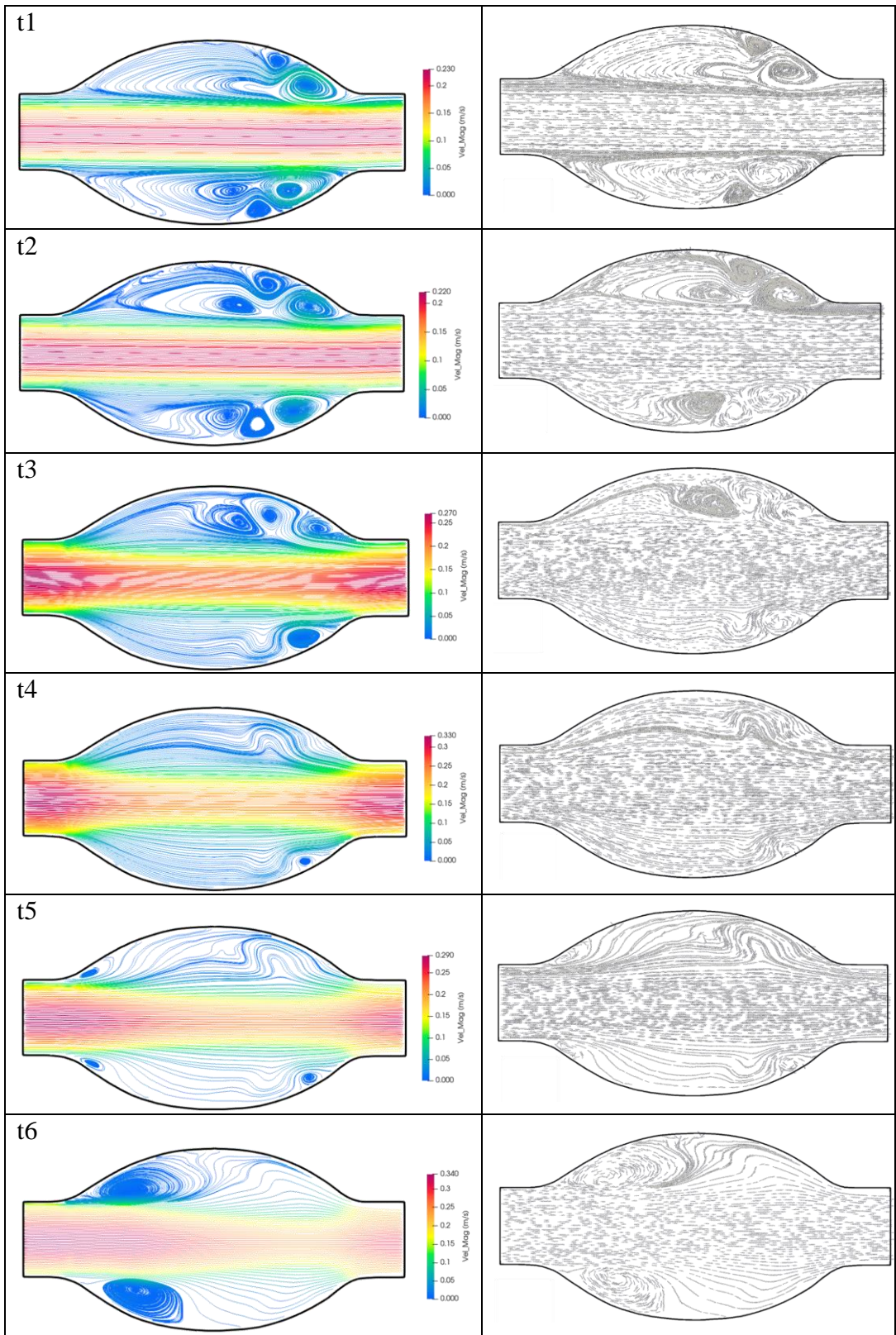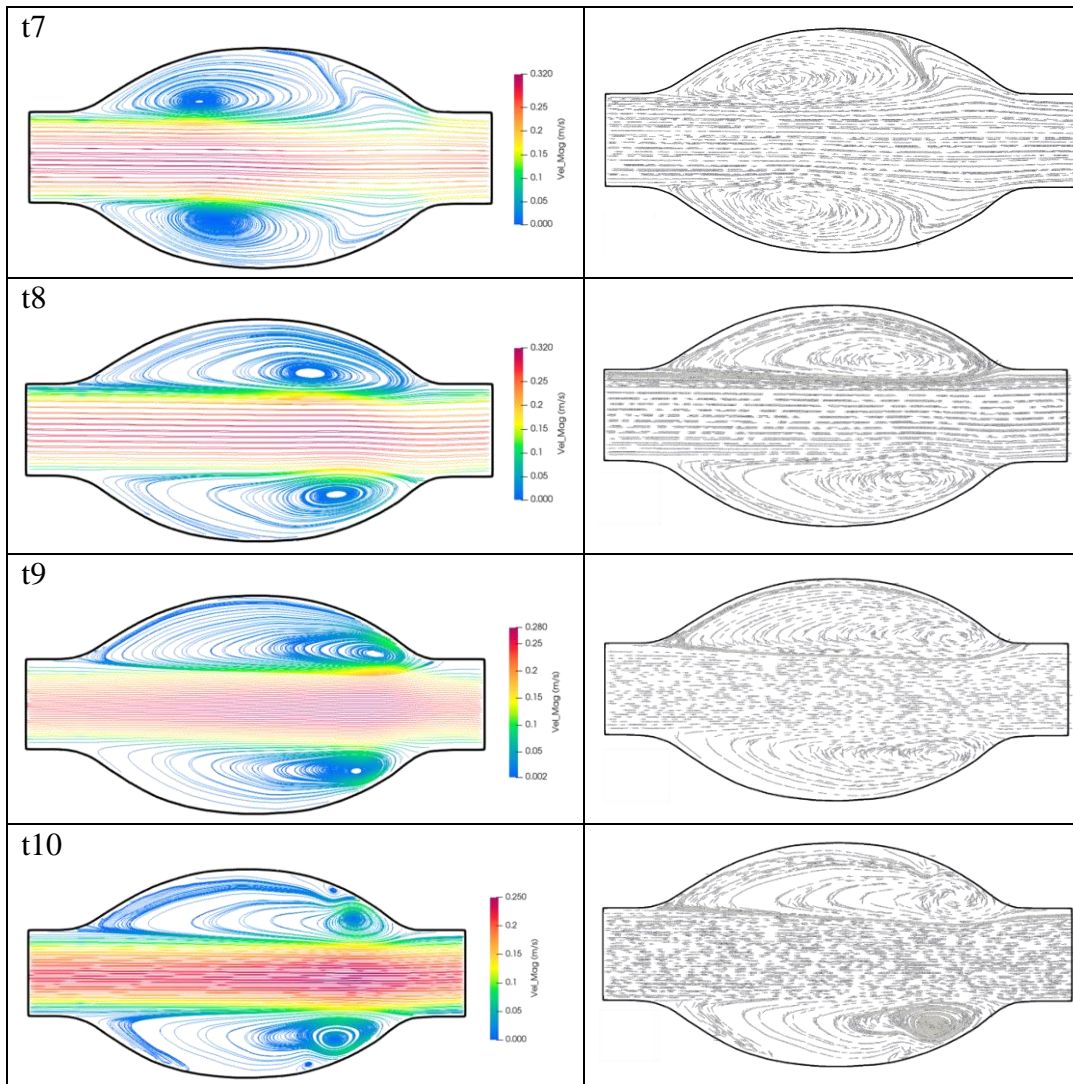
Figure 4.15: Streamlines (vel_mag colored) and vector fields for 10 different time increments (Time-varying pattern) / (Above to below: t1 to t10)

4.3.3   WSS Result

Calculation parameters of WSS are kept the same as the method mentioned in the steady WSS section. Due to the asymmetry on the wall, WSS distribution is calculated only for the upper side of the bulge. Thus, the WSS distribution and flow characteristics are correlated with the upper side of the aneurysm. WSS distributions from t1 to t10 are separately available in Figure 4.16, and all of the WSS distributions are given together in Figure 4.17.

When the WSS distribution for t1 is examined, firstly, a negative WSS caused by the primary vortex rotating in the counter-clockwise direction on the distal edge is observed. Secondly, a smaller magnitude positive WSS caused by the clockwise rotating secondary vortex located is encountered. There are two attachment points from the secondary vortex to the primary vortex and from the primary vortex to the jet flow, which are also two points with "0" in the distal edge of the WSS distribution. In t2, in addition to the t1, positive WSS values are started to be observed in the proximal edge due to the attached regular flow that occurs because of the acceleration. The WSS created by the secondary vortex seems to be unaffected by the acceleration, yet the WSS created by the primary vortex decreases. At time t3, positive wall shear stresses are encountered throughout the bulge due to increased acceleration. Since the primary vortex in the distal neck still shows a presence but is weakened, much lower negative wall shear stress values are encountered in the distal neck before the outlet than the t2 and t1 moments. These values are spread over a smaller length due to the area occupied by the vortex is reduced. Since the temporal acceleration dominates the adverse pressure gradient, in the t4, a fully attached flow is observed in the bulge part. It causes positive WSS values in the entire aneurysm region, including the inlet and outlet. Although the WSS values encountered in the bulge are smaller than the inlet and outlet part at t4, they are even higher in magnitude than the values in the bulge of steady flow in the case of Re=900.

Negative peak WSS values created by the primary vortex, which started to occur at the proximal edge due to deceleration at t5 time, are observed. After the vortex

region, positive WSS values are observed after the attachment point where the regular flow is presence. With the second acceleration, it is observed that the area of the vortex structure formed at the proximal edge at the time of t5 widens, but the WSS effect weakens. This change is consistent with the system experiencing acceleration at that moment. Starting from the second deceleration, at t7, t8, and t9, the power of the recirculating zone increases gradually, and the center is localized at the distal neck side. Compared to the moderate values spread over the entire bulge, an increase in the magnitude of the WSS is observed that is localized to the distal neck side. The collision of the circulation center to the distal neck results in creating another counter-rotating (clockwise) vortex structure. That is why, at t10, small positive WSS values are observed just before the distal edge negative peak.

When the WSS distributions are considered as a whole, the highest positive and negative peaks in magnitude are observed in the distal neck. The highest positive peaks are encountered caused by the attached flow structure in t4 and t6 (acceleration peaks.) In terms of magnitude, the highest negative peaks in the distal end are obtained from the primary vortex structures being stuck in the distal neck at the t9 and t10 moments. This observation is consistent with the deduction of Finol et al. (2002) [66]. The negative peak in the proximal neck is seen at t5 due to the localized primary vortex formed in the proximal neck because of the high deceleration rate.
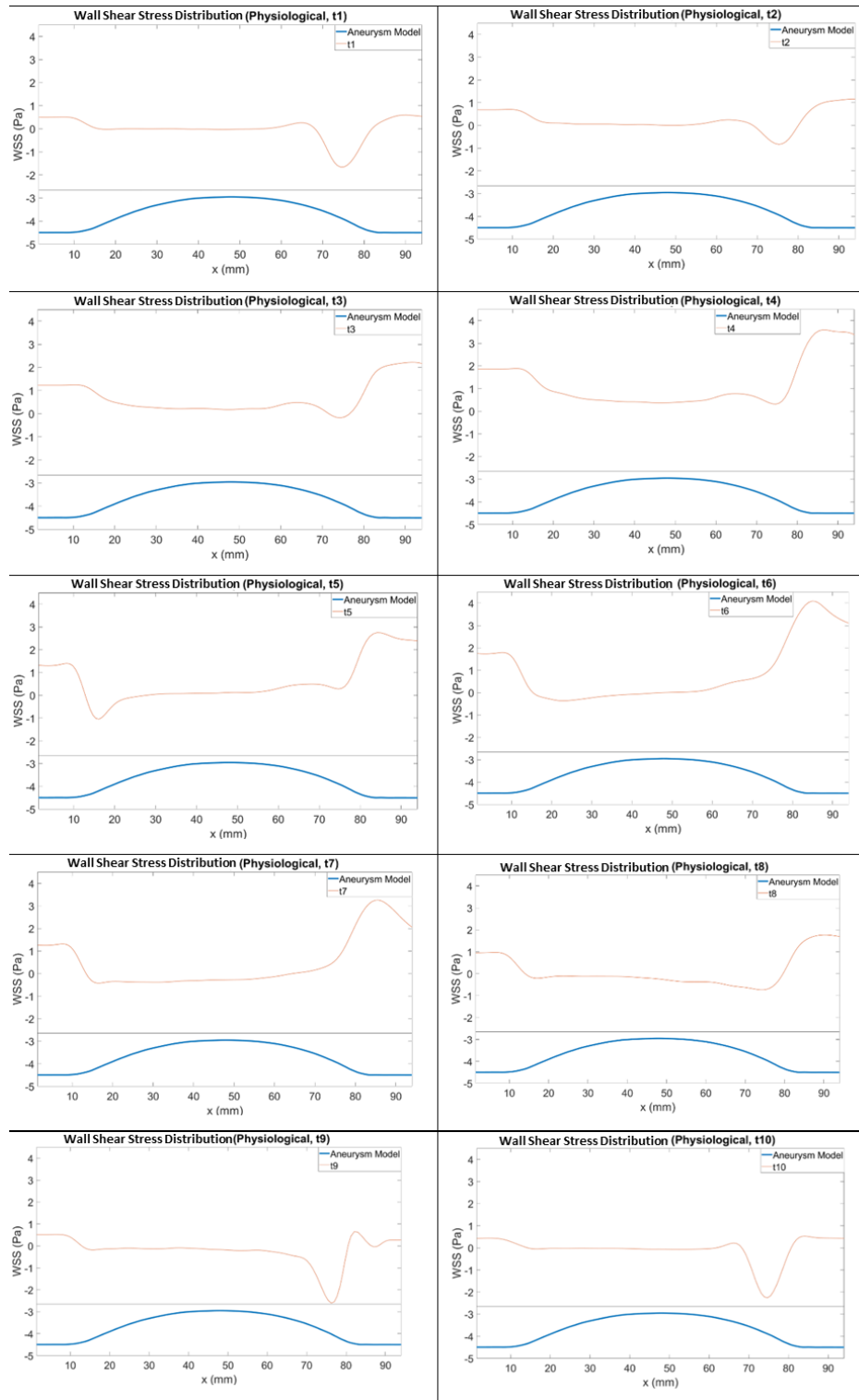
Figure 4.16: WSS distributions from t1 to t10 for physiological pattern
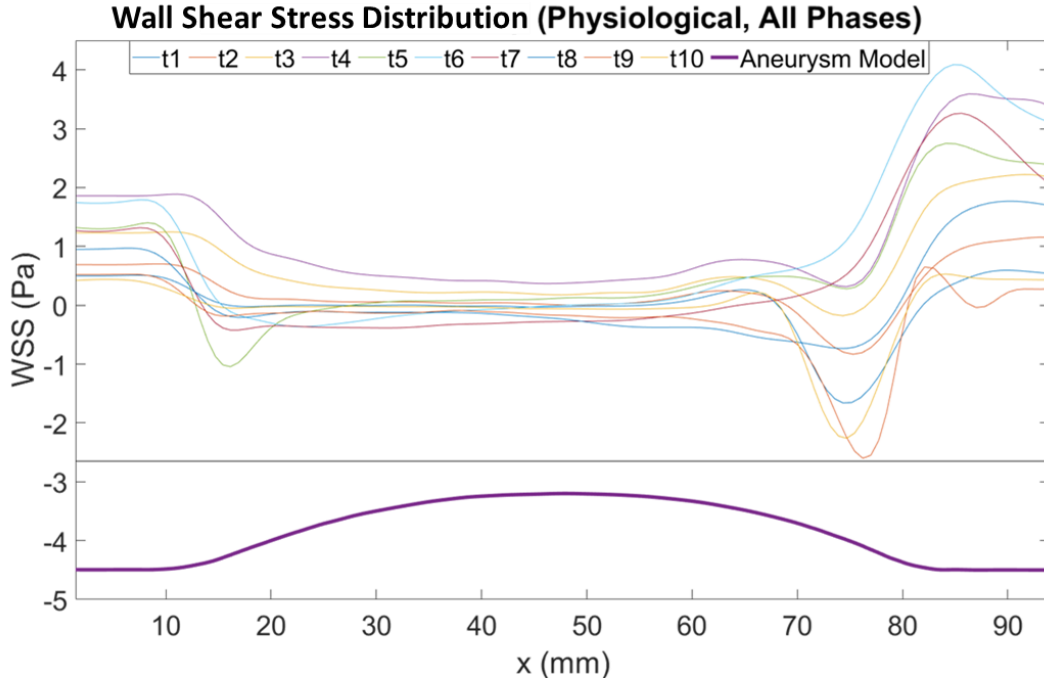
Figure 4.17: WSS distribution for all phases of the physiological pattern

4.3.4   WSS Parameters

Time-average or time related metric calculations are achieved by linearly interpolating the discrete time data.

➢ TAWSS and TAWSSG

Equation (4.4) and Equation (4.5) presents the equations of the time average wall shear stress (TAWSS) and time average wall shear stress gradient (TAWSSG), respectively.

$$TAWSS = \frac{1}{T}\int_0^T |\tau_w|\, dt \tag{4.4}$$

$$TAWSSG = \left.\frac{\partial \overline{\tau_w}}{\partial x}\right|_{x=x_i} = \frac{\overline{\tau_w}(x_i + \Delta x) - \overline{\tau_w}(x_i - \Delta x)}{2\Delta x} \tag{4.5}$$

Figure 4.18 includes the time average WSS distribution taken for ten different times in the physiological pattern ($Re_{mean} \approx 300$) in which the experiments are carried out and steady WSS distribution (Re=300). Considering below plot, the results of the physiological pattern are very similar to the steady Re=300 case in terms of both pattern and value. A negative and smaller peak on the proximal edge compared to the distal edge is observed due to the separation. On the bulge side, WSS values close to "0" are observed. Finally, a negative and subsequent positive peak is observed due to the reattachment zone and jet flow. This situation shows how reasonable the stable flow assumption is when considered as the average time characteristic.

Positive WSS values encountered before the negative peak at the distal edge due to the secondary clockwise rotating vortex structure occurred in some parts of the physiological pattern creates a difference between steady and physiological cases. Likewise, the TAWSSG distribution in Figure 4.19 is similar to the WSSG distribution in the steady Re=300. As in TAWSS, a generally observed difference is an additional gradient is created by the secondary vortex in the distal neck. Thus, the difference is the gradient peak close to the distal end towards the upstream, which is smaller than the proximal and distal end gradient. The region with the most hemodynamic abnormality appears to be the distal neck for physiological average.
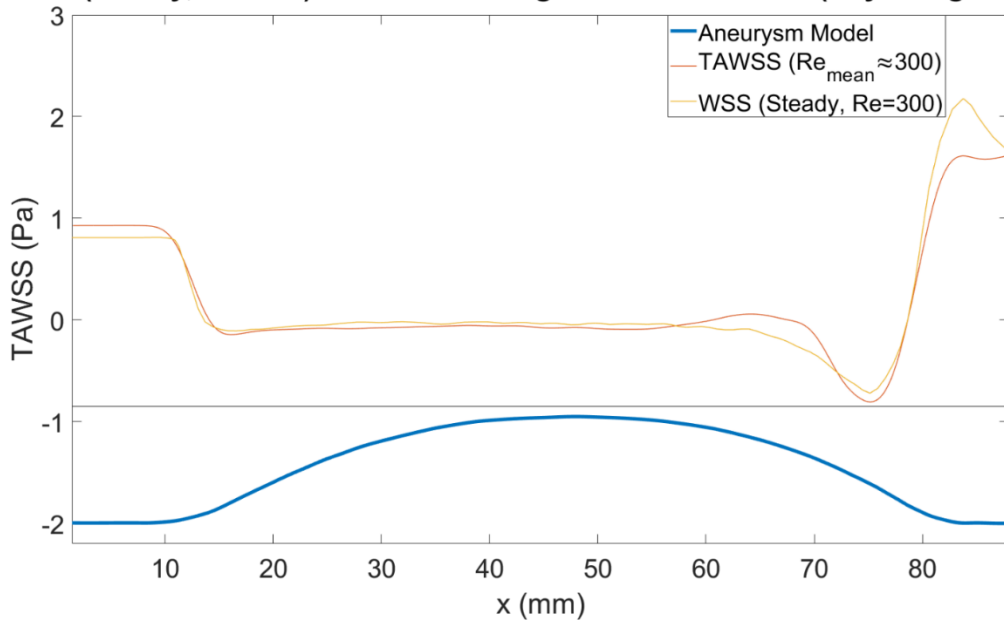
Figure 4.18: Time-average WSS distribution for all phases of the physiological pattern and steady WSS (Re=300) distribution
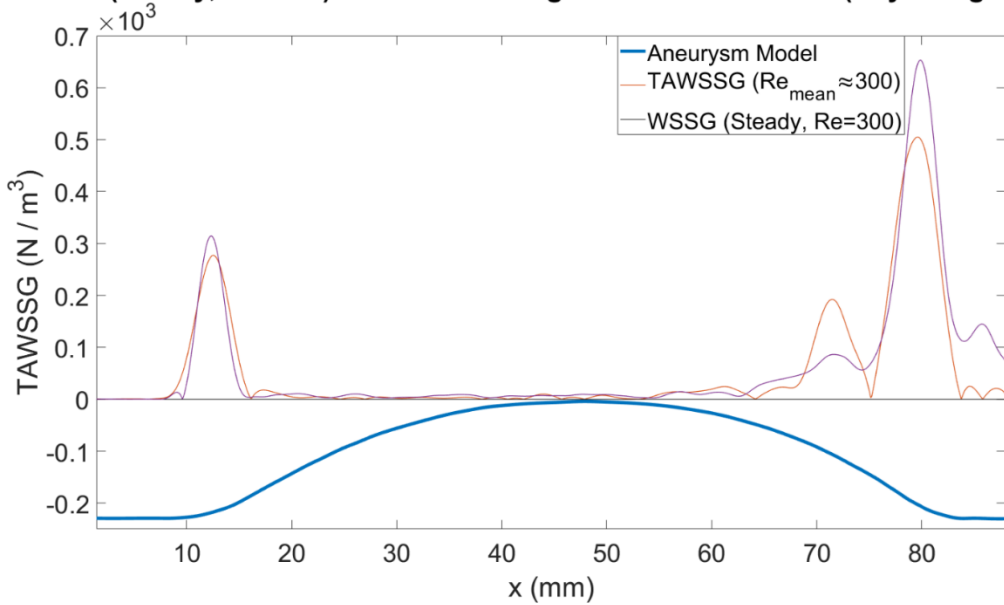
Figure 4.19: Time-average WSSG distribution for all phases of the physiological pattern and steady WSSG (Re=300) distribution (Absolute)

➢ WSSG

The equation used in the calculation of WSSG is given in Equation (4.6):

$$WSSG = \left.\frac{\partial \tau_w}{\partial x}\right|_{x=x_i} = \frac{\tau_w(x_i + \Delta x) - \tau_w(x_i - \Delta x)}{2\Delta x} \qquad (4.6)$$

Gradients are calculated by making central differencing, as mentioned in the steady part. Forward and backward differencing is applied for the data at the beginning and the end. After interpreting the TAWSSG, it is important to examine the PIV data separately for each time point since it brings time variability to the hemodynamic discussion. Below is the WSSG distribution calculated for each time moment from t1 to t10 in Figure 4.20.
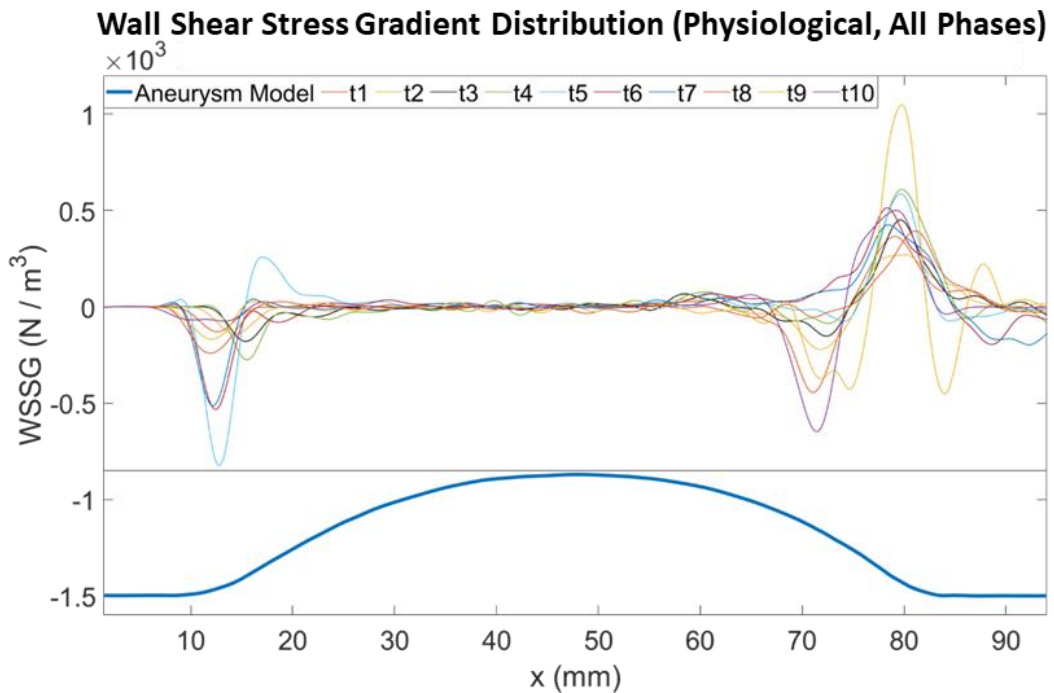
Figure 4.20: WSSG distribution for all phases of the physiological pattern

When Figure 4.20 is examined, the highest peak is encountered in the proximal edge part due to the vortex structure formed by the deceleration-induced separation at the t5 moment. The second highest peaks are seen at the proximal edge with the spread of the primary vortex to a wider area, formed at the t6 and t7 moments. In t9, a high-speed vortex structure is observed moving in a counter-clockwise direction at the wall edge, as the center of the vortex is being compressed to the distal edge. Thus, the highest peak for the distal edge in terms of WSSG is observed at that time since there is a transition from a high negative magnitude value to a positive peak.

The secondary vortex structure formed by the collision of the recirculation center to the distal edge at the time of t10 caused an additional and high magnitude gradient to be observed a little more upstream than the usually expected location at the distal edge. When more than one vortex structure is seen, more than one WSSG peak is also encountered. To summarize, when the steady flow condition is considered with the physiological moments like more than one vortex structure exist, it has been found that there are high gradient values in places where usually "0" WSS is observed. In addition, the highest proximal edge peak is found at t5, and the highest distal edge peak is at t10, which means that the highest hemodynamic abnormality is observed at downstream as always.

➢ OSI

The OSI is calculated to present the oscillatory nature of vascular flows. The OSI number ranges from "0" to "0.5". "0" means unidirectional flow, while "0.5" means fully oscillatory flow. The calculated OSI distribution can be seen in Figure 4.21. The importance of the OSI parameter can be better understood together with the low shear stress – high OSI theory mentioned in the literature discussions. As mentioned in the literature, the atherosclerotic disease is likely to be observed in areas where low WSS - high OSI is observed, and the general opinion in the literature supports this. For this reason, while examining OSI, places with high OSI magnitude are focused, and low WSS - high OSI regions are mainly reported together with the TAWSS values.
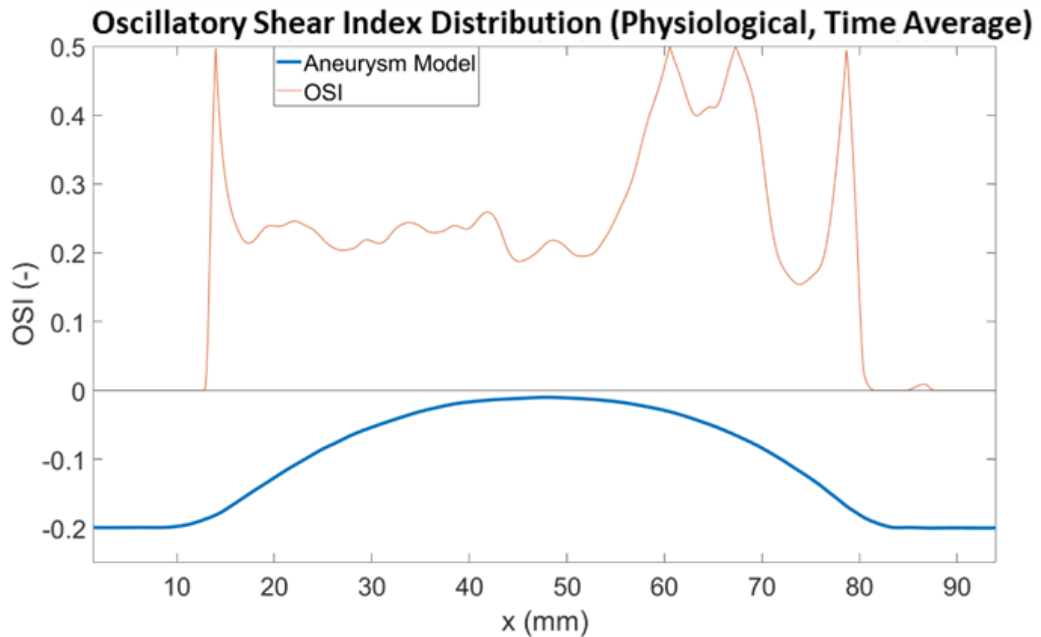
Figure 4.21: OSI distribution of the physiological pattern

OSI values are seen throughout the bulge around 0.25 due to the fact that the bulge is sometimes exposed to attached flow and sometimes to recirculation flow. Values close to 0.5 in OSI value are observed in 4 points. These are "x = 14 mm", "x = 60 mm", "x = 67 mm" and "x = 78 mm". The high OSI values observed in "x=14 mm" and "x=78mm" are related to several factors. These are the separation point formed in proximal edge, reattachment point formed in distal edge, and the forward attached flow occasionally observed in physiological flow. High OSI values at "x = 60 mm" and "x=67 mm" are observed due to secondary vortices formed by the collision of the recirculation center at the distal edge.

The point "x=78 mm" does not fit the low WSS – high OSI theory due to its high WSS value compared to others. The remaining three points are subject to severely low WSS and high OSI. Thus, according to the theory, "x=14 mm, x= 60 mm, and x=67 mm" points and their surroundings can be considered as a sensitive region to localization of atherosclerotic.

➢ TWSSG

The Temporal Wall Shear Stress Gradient (TWSSG) allows the WSS gradient to be investigated in terms of change in time rather than spatial change. According to the study of White et al. (2001), it is observed that temporal changes disrupt the vessel structure by stimulating endothelial cell proliferation [8]. This situation causes being prone to possible vascular enlargement or rupture. The equation using in the TWSSG metric calculation is provided in Equation (4.7). The calculated TWSSG distribution can be seen in Figure 4.22.

$$TWSSG = \frac{\partial \tau_w}{\partial t}\bigg|_{t=t_i} = \frac{\tau_w(t_i + \Delta t) - \tau_w(t_i - \Delta t)}{2\Delta t} \tag{4.7}$$
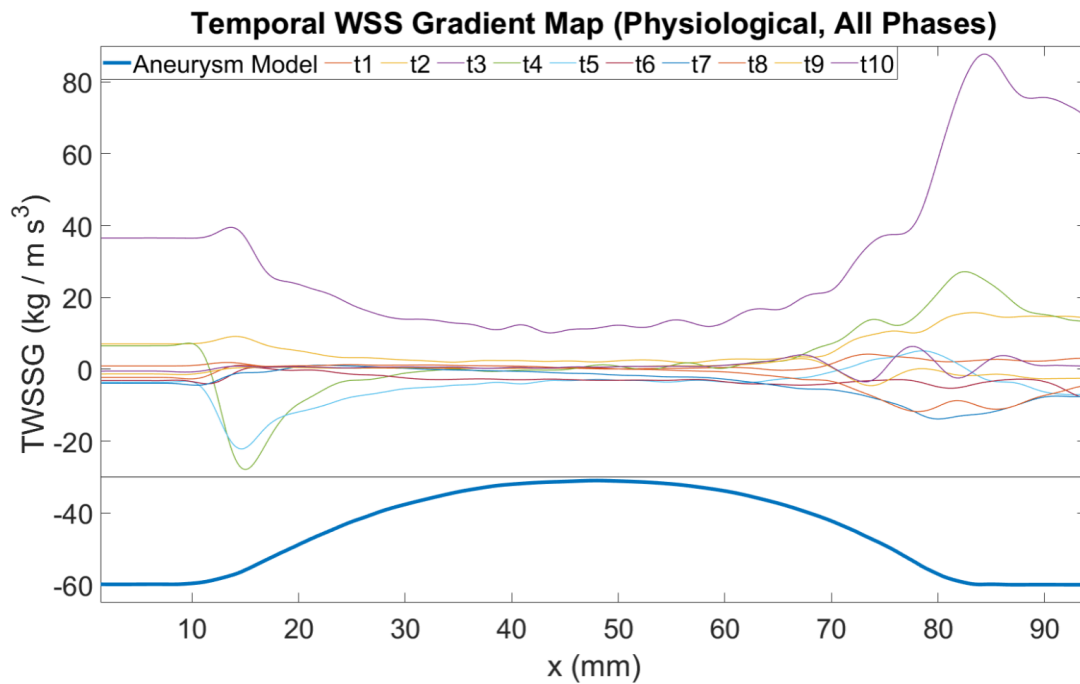
Figure 4.22: TWSSG distribution of all phases in physiological pattern

For ten different time points, TWSSG results are examined. Due to the sudden acceleration, the temporal gradients are high for t3 and t4 moments, especially for t3. However, it has been observed that the distal end, which always has a high gradient characteristic in spatial examinations, is more stable in terms of peaks from the time perspective. In the proximal edge, this stability is disrupted by the primary vortex caused by deceleration. In terms of time instability, high gradients can be seen in the proximal edge at t4 and t5 moments and the distal edge at t3 and t4 moments. Thus, these regions become more exposed to endothelial cell proliferation at these times.

CHAPTER 5

CONCLUSIONS

This study aims to investigate the flow characteristics inside the abdominal aortic aneurysm and construct its wall shear stress distribution by developing methods for WSS measurement for PIV. Simplified and rigid aneurysm geometry is used to reach the aim. The experiments were conducted at steady flow cases (Re=300 and Re=900) to understand Re number's effects and develop a methodology for WSS measurement. In addition, experiments also were conducted at the physiological pattern ($Re_{mean} \approx 300$ and α=7.17) to investigate the time-varying characteristics of the flow inside the aneurysm. During the experiments, the measurements were taken by the turbine flowmeter, pressure transducers, and PIV. Moreover, to examine the spatial resolution effect, close-up studies were conducted for steady cases. The conclusions inferred from the experimental results discussed in the previous chapter are listed below.

Conclusions about WSS measurement:

- Some portions of the PIV data gave overestimated velocity and WSS results. The cross-correlation algorithm of PIV overestimates the velocity magnitudes where the high velocity gradient and seeding particle-wall interaction exists. Thus, the overestimation of velocity was observed, especially near the wall.

- Initial data point selection is quite critical since taking velocity data close to and away from the wall may result in misguided WSS magnitudes. If data is taken too close to the wall, overestimated velocity data mislead the results. On the other hand, if initial data is away from the wall, the WSS results will be misdirected with the change of flow physics. To determine the accurate

WSS for both whole field and close-up studies, 1st closest to 5th closest initial data points at the straight, circular pipe were compared. Together with the initial data points, different velocity profiles (linear, 2nd order polynomial, 3rd order polynomial, point to point (wall-independent), and spline velocity) were compared for obtaining accurate WSS estimation.

- The comparison was based on the analytical solution to determine a methodology. For this reason, results of different initial point and velocity profile combinations were compared on the circular pipe in steady cases where analytical solution exists. It was observed that the 4th initial data to the wall gave the closest result to the analytical solutions for close-up and whole field studies. However, since the spatial resolution of the close-up was superior to the whole field, the initial data used in close-up studies was closer to the wall than the whole field. Among the velocity profiles, it was observed that 3rd order and cubic spline velocity profile methods gave reliable results when all cases (Re=300/900 (steady) and whole field/close-up) were considered. As a result, spline fit was used by also evaluating the inference in the literature that spline fit gives more robust results, especially in complex flows.

- Similar discussions were made in the bulge part with the findings obtained from the comparison in the circular pipe. In the interpretation of the results in the bulge portion, the WSS results in the literature together with the whole field and close-up results were evaluated. At the bulge part, close-up studies gave the same accuracy in terms of initial data number with the straight pipe portion, which is the 4th initial data point with spline fit velocity profile. On the other hand, whole field results with 2nd initial data point and close-up results with 4th initial data point gave similar output in terms of WSS. Since close-up (4th data) and whole field (2nd data) gave similar results, and close-up studies took tremendous time to conduct, physiological WSS distributions are reported with whole field experiments (2nd closest data, cubic spline profile.)

Conclusions about flow field and WSS:

- For the steady case, the jet flow was observed in the continuation of the circular pipe area. Low velocity recirculation zones were observed in the bulge part due to the separation caused by the adverse pressure gradient. Negative and close to "0" WSS values were observed in low velocity zones at the bulge portion. However, negative and positive WSS peaks were encountered in the reattachment region towards the distal edge. An increase in the WSS peak magnitudes was observed in the distal edge due to a rise in the Re number. The highest spatial gradients were seen at the proximal and distal edges. Yet, the distal edge gradient values were higher, and the gradient values increased with the increase in Re number. Therefore, the highest hemodynamic abnormalities were located to the distal edge at Re=900.

- The determining factors of the internal characteristics in time-varying ($Re_{mean} \approx 300$ and $\alpha = 7.17$) flow were acceleration and deceleration and their rate. In general, the weakening of the vortex structures and attached flow was observed during acceleration. On the other hand, the strengthening of separation and vortex structures occurred in the regions during deceleration. Since the flow moves forward, multiple/multi-directional vortex structures were encountered in the bulge portion as the recirculation region hits the distal neck. During the physiological flow, the WSS patterns very close to steady flows' were occasionally encountered. Yet, sometimes positive WSS values that were not observed in steady flows were seen, especially in the bulge portion, due to structures such as attached flow and clockwise rotating vortex.

- The time average WSS distribution of physiological pattern had close values and patterns to the Re=300 steady flow. The difference was observed between the two cases where the attached forward flow and clockwise rotating vortex induced positive WSS. The same held for the time average

WSS gradient. When the wall shear stress gradient of each phase was examined separately, the highest spatial gradient was encountered in the distal edge region at t10 (t=1.01 sec).

- Generally, moderate OSI values close to "0.25" were observed in the bulge. However, values close to the maximum OSI, "0.5," were encountered in three regions. These were the separation region, the region where the collision occurs, and the reattachment region at the distal edge. Considering the low WSS – high OSI theory, only the distal edge region between these three regions did not comply with this theory. The remaining regions were regarded as risky in terms of localization of atherosclerotic (thickening or hardening of the arteries) and intimal hyperplasia. In addition, these regions were sensitive to rupture and growth.

- When the WSS distribution was examined in terms of time gradient, due to the high acceleration rate at t3, the time gradient seemed highest among the other nine time instants. The distal edge region, which was interpreted as sensitive to hemodynamic abnormalities because of the WSS and WSSG, appeared to be stable in terms of time. It was also observed that time gradients were high at the t3, t4, and t5 moments where high acceleration and deceleration rates were encountered at the distal and proximal edge of the vessel. These regions were interpreted as where endothelial cell proliferation was likely to be observed.

5.1 Future Extensions to the Study

The present study can be further improved for future work with the items listed below:

- By using stereoscopic PIV, third velocity data can be obtained for the plane under investigation. With 2D and stereoscopic (3D) multiplane PIV measurements, the WSS contour of the investigated geometry can be deduced. However, in 2D PIV measurements, it is necessary to conduct experiments with both cross and axial planes, while in 3D PIV experiments, it is sufficient to perform multiplane studies in one direction. For this reason, the amount of experimentation with stereoscopic PIV decreases considerably. General flow physics can be investigated with single-plane experiments in axisymmetric geometries. On the other hand, the multi-plane experiment approach is critical in complex geometries because the physics of flow in each plane is different, and each region should be examined separately. Multiplane experiment presentation can be seen in Figure 5.1.
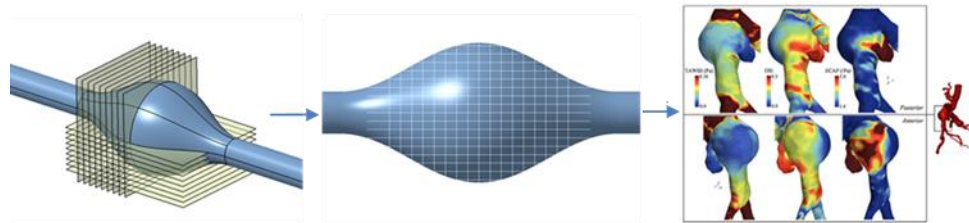
Figure 5.1: Presentation of multi-plane study [81]

- The wall location determination is important in stress calculations. In the 2D single-plane and 2D multi-plane experiments, wall location can be extracted by using the PIV camera image. However, in stereoscopic PIV, since a third (in-plane) velocity component exists; also in-plane geometry information is needed, and it cannot be extracted from PIV camera image. So geometry information should be obtained from an additional method such as using an

existing CAD model or extracting geometry of the model by using different camera angles, etc.

- Non-Newtonian blood–mimicking fluid can be used in order to see the importance of the shear-thinning effect on an Abdominal Aortic Aneurysm geometry.

- PDMS phantom material can be used to improve the precision of geometry used. In addition, the use of PDMS material, if preferred, also enables the use of patient-specific geometry and compliance models.

- Experimental set-up can be built on a rigid structure in order to prevent unwanted and uncontrolled compliance effects.

REFERENCES

[1] Silverberg, E., Boring, C. C., & Squires, T. S. (1990). Cancer statistics, 1990. CA: A Cancer Journal for Clinicians, 40(1), 9–26. https://doi.org/10.3322/canjclin.40.1.9

[2] Norman, P. E., & Curci, J. A. (2013). Understanding the effects of tobacco smoke on the pathogenesis of aortic aneurysm. Arteriosclerosis, Thrombosis, and Vascular Biology, 33(7), 1473–1477. https://doi.org/10.1161/atvbaha.112.300158

[3] Noel, A. A., Gloviczki, P., Cherry, K. J., Bower, T. C., Panneton, J. M., Mozes, G. I., Harmsen, W. S., Jenkins, G. D., & Hallett, J. W. (2001). Ruptured abdominal aortic aneurysms: The excessive mortality rate of conventional repair. Journal of Vascular Surgery, 34(1), 41–46. https://doi.org/10.1067/mva.2001.115604

[4] Davis M, Harris M, Earnshaw JJ (2013) Implementation of the national health service abdominal aortic aneurysm screening program in England. J Vasc Surg 57:1440–1445

[5] Brewster, D. C., Cronenwett, J. L., Hallett, J. W., Johnston, K. W., Krupski, W. C., & Matsumura, J. S. (2003). Guidelines for the treatment of abdominal aortic aneurysms: Report of a subcommittee of the Joint Council of the American Association for vascular surgery and society for vascular surgery. Journal of Vascular Surgery, 37(5), 1106–1117. https://doi.org/10.1067/mva.2003.363

[6] Fu, B. M., & Wright, N. T. (Eds.). (2019). Molecular, cellular, and tissue engineering of the vascular system. SPRINGER.

[7] Chatzizisis, Y.S., Baker, A.B., Sukhova, G.K., Koskinas, K.C., Papafaklis, M.I., Beigel, R., Jonas, M., Coskun, A.U., Stone, B.V., Maynard, C., Shi, G.P., Libby, P., Feldman, C.L., Edelman, E.R., Stone, P.H., 2011. Augmented expression and activity of extracellular matrix-degrading enzymes in regions of low endothelial shear stress colocalize with coronary atheromata with thin fibrous caps in pigs. Circulation 123, 621–630.

[8] White CR, Haidekker M, Bao X, Frangos JA (2001) Temporal gradients in shear, but not spatial gradients, stimulate endothelial cell proliferation. Circulation 103(20):2508–2513

[9] Salsac, A.-V., Sparks, S. R., Chomaz, J.-M., & Lasheras, J. C. (2006). Evolution of the wall shear stresses during the progressive enlargement of symmetric abdominal aortic aneurysms. Journal of Fluid Mechanics, 560, 19. https://doi.org/10.1017/s002211200600036x

[10] DiCarlo, A. L., Holdsworth, D. W., & Poepping, T. L. (2019). Study of the effect of stenosis severity and non-Newtonian viscosity on multidirectional wall shear stress and flow disturbances in the carotid artery using particle image velocimetry. Medical Engineering & Physics, 65, 8–23. https://doi.org/10.1016/j.medengphy.2018.12.023

[11] Klabunde, R. E. (2012). Cardiovascular physiology concepts (2nd ed.). Wolters Kluwer.

[12] Tortora, G. J., Derrickson, B., Tortora, G. J., & Tortora, G. J. (2017). Tortora's principles of Anatomy & physiology. Wiley.

[13] Iaizzo, P. A. (2015). Handbook of cardiac anatomy, physiology, and devices. Springer.

[14] McPhee, J. T., Hill, J. S., & Eslami, M. H. (2007). The impact of gender on presentation, therapy, and mortality of abdominal aortic aneurysm in the United States, 2001-2004. Journal of Vascular Surgery, 45(5), 891–899. https://doi.org/10.1016/j.jvs.2007.01.043

[15] Ashton HA, Buxton MJ, Day NE, Kim LG, Marteau TM, Scott RA, Thompson SG, Walker NM (2002) The multicentre aneurysm screening study (mass) into the effect of abdominal aortic aneurysm screening on mortality in men: a randomized control trial. Lancet 360:1531–1539

[16] Lederle FA, Johnson GR, Wilson SE, Ballard DJ, Jordan WD Jr, Blebea J, Littooy FN, Freischlag JA, Bandyk D, Rapp JH, Salam AA, Veterans Affairs Cooperative Study, I (2002) Rupture rate of large abdominal aortic aneurysms in patients refusing or unfit for elective repair. JAMA 287:2968–2972

[17] Aggarwal, S., Qamar, A., Sharma, V., & Sharma, A. (2011). Abdominal aortic aneurysm: A comprehensive review.

[18] Howard DP, Banerjee A, Fairhead JF et al (2015) Population-based study of incidence of acute abdominal aortic aneurysms with projected impact of screening strategy. J Am Heart Assoc 4:e001926

[19] Teufelsbauer, H., Polterauer, P., Lammer, J., Huk, I., Nanobachvili, J., & Kretschmer, G. (2006). Repair of abdominal aortic aneurysms: The benefits of offering both endovascular and open surgical techniques. Perspectives in Vascular Surgery and Endovascular Therapy, 18(3), 238–246. https://doi.org/10.1177/1531003506296861

[20] Schermerhorn, M. (2009). A 66-year-old man with an abdominal aortic aneurysm. JAMA, 302(18), 2015. https://doi.org/10.1001/jama.2009.1502

[21] Wanhainen, A., Verzini, F., Van Herzeele, I., Allaire, E., Bown, M., Cohnert, T., Dick, F., van Herwaarden, J., Karkos, C., Koelemay, M., Kölbel, T., Loftus, I., Mani, K., Melissano, G., Powell, J., Szeberin, Z., ESVS Guidelines Committee, de Borst, G. J., Chakfe, N., … Verhagen, H. (2019). Editor's choice – European society for vascular Surgery (esvs) 2019 clinical practice guidelines on the management of abdominal aorto-iliac artery aneurysms. European Journal of Vascular and Endovascular Surgery, 57(1), 8–93. https://doi.org/10.1016/j.ejvs.2018.09.020

[22] Endovascular versus Open Repair of Abdominal Aortic Aneurysm. (2010). The New England Journal of Medicine, 362(20).

[23] Patel, R., Sweeting, M. J., Powell, J. T., & Greenhalgh, R. M. (2016). Endovascular versus open repair of abdominal aortic aneurysm in 15-years' follow-up of the UK endovascular aneurysm repair trial 1 (EVAR Trial 1): A randomized controlled trial. The Lancet, 388(10058), 2366–2374. https://doi.org/10.1016/s0140-6736(16)31135-7

[24] Miranda, S. de, Miranda, P. C., Volpato, M. G., Folino, M. C., Kambara, A. M., Rossi, F. H., & Izukawa, N. M. (2014). Open vs. endovascular repair of abdominal aortic aneurysm: A comparative analysis. Jornal Vascular Brasileiro, 13(4), 276–284. https://doi.org/10.1590/1677-5449.0118

[25] ACC/AHA 2005 practice guidelines for the management of patients with peripheral arterial disease (Lower extremity, RENAL, MESENTERIC, and Abdominal Aortic): Executive summary. (2006). Circulation, 113(11), 1474–1547. https://doi.org/10.1161/circulationaha.106.173994

[26] Chervu, A., Clagett, G. P., Valentine, R. J., Myers, S. I., & Rossi, P. J. (1995). Role of physical examination in detection of abdominal aortic aneurysms. Surgery, 117(4), 454–457. https://doi.org/10.1016/s0039-6060(05)80067-4

[27] Miranda, S. de, Miranda, P. C., Volpato, M. G., Folino, M. C., Kambara, A. M., Rossi, F. H., & Izukawa, N. M. (2014). Open vs. endovascular repair of abdominal aortic aneurysm: A comparative analysis. Jornal Vascular Brasileiro, 13(4), 276–284. https://doi.org/10.1590/1677-5449.0118

[28] Holzapfel GA, Ogden RW (eds) (2017) Biomechanics: trends in modeling and simulation. Springer-Verlag Inc, New York

[29] T. V. Kruchten, "CFD modeling of abdominal aortic aneurysms," Master's thesis, Delft University of Technology, Delft, Netherland, 2015.

[30] Simmonds, M.J., Meiselman, H.J., Baskurt, O.K., 2013. Blood rheology and aging. Journal of Geriatric Cardiology 10:291-301.

[31] A. L. DiCarlo, "Investigation of Flow Disturbances and Multi-Directional Wall Shear Stress in the Stenosed Carotid Artery Bifurcation Using Particle Image Velocimetry," Doctoral thesis, The University of Western Ontario, Ontario, Canada, 2018.

[32] L.Waite and J. Fine, Applied Biofluid Mechanics (McGraw-Hill Education, 2007).

[33] Morbiducci, U., Gallo, D., Massai, D., et al., 2011. On the importance of blood rheology for bulk flow in hemodynamic models of the carotid bifurcation. Journal of Biomechanics 44:2427-2438.

[34] Johnston, B.M., Johnston, P.R., Corney, S., et al., 2006. Non-Newtonian blood flow in human right coronary arteries: Transient simulations. Journal of Biomechanics 39:1116-1128.

[35] Geoghegan, P. H., Jermy, M. C., & Nobes, D. S. (2016). A PIV comparison of the flow field and wall shear stress in rigid and compliant models of healthy carotid arteries. Journal of Mechanics in Medicine and Biology, 17(03), 1750041. https://doi.org/10.1142/s0219519417500415

[36] Yazdi, S. G., Geoghegan, P. H., Docherty, P. D., Jermy, M., & Khanafer, A. (2018). A review of arterial phantom fabrication methods for flow measurement using PIV techniques. Annals of Biomedical Engineering, 46(11), 1697–1721. https://doi.org/10.1007/s10439-018-2085-8

[37] Kefayati, S., Holdsworth, D. W., & Poepping, T. L. (2014). Turbulence intensity measurements using particle image velocimetry in diseased carotid artery models: Effect of stenosis severity, plaque eccentricity, and ulceration. Journal of Biomechanics, 47(1), 253–263. https://doi.org/10.1016/j.jbiomech.2013.09.007

[38] Minakawa, M., Fukuda, I., Igarashi, T., Fukui, K., Yanaoka, H., & Inamura, T. (2010). Hydrodynamics of aortic cannulae during extracorporeal circulation in a Mock aortic arch aneurysm model. Artificial Organs, 34(2), 105–112. https://doi.org/10.1111/j.1525-1594.2009.00764.x

[39] Yousif, M. Y., Holdsworth, D. W., & Poepping, T. L. (2010). A blood-mimicking fluid for particle image velocimetry with silicone vascular models. Experiments in Fluids, 50(3), 769–774. https://doi.org/10.1007/s00348-010-0958-1

[40] Najjari, M. R., Hinke, J. A., Bulusu, K. V., & Plesniak, M. W. (2016). On the rheology of refractive-index-matched, non-Newtonian blood-analog fluids for PIV experiments. Experiments in Fluids, 57(6). https://doi.org/10.1007/s00348-016-2185-x

[41] Stamatopoulos, C., Papaharilaou, Y., Mathioulakis, D. S., & Katsamouris, A. (2010). Steady and unsteady flow within an axisymmetric tube dilatation. Experimental Thermal and Fluid Science, 34(7), 915–927. https://doi.org/10.1016/j.expthermflusci.2010.02.008

[42] Bai, K., & Katz, J. (2014). On the refractive index of sodium iodide solutions for index matching in PIV. Experiments in Fluids, 55(4). https://doi.org/10.1007/s00348-014-1704-x

[43] Lewin, S. A., & Wagner, R. S. (1953). The nature of iron thiocyanate in solution. Journal of Chemical Education, 30(9), 445. https://doi.org/10.1021/ed030p445

[44] Brindise, M. C., Busse, M. M., & Vlachos, P. P. (2018). Density- and viscosity-matched Newtonian and non-Newtonian blood-analog solutions with PDMS refractive index. Experiments in Fluids, 59(11). https://doi.org/10.1007/s00348-018-2629-6

[45] Walker, A. M., Johnston, C. R., & Rival, D. E. (2013). On the characterization of a non-Newtonian blood analog and its response to pulsatile flow downstream of a simplified stenosis. Annals of Biomedical Engineering, 42(1), 97–109. https://doi.org/10.1007/s10439-013-0893-4

[46] Mann DE, Tarbell JM (1990) Flow of non-Newtonian blood analog fluids in rigid curved and straight artery models. Biorheology 27:711–733

[47] Long JA, Undar A, Manning KB, Deutsch S (2005) Viscoelasticity of pediatric blood and its implications for the testing of a pulsatile pediatric blood pump. ASAIO J 51:563–566. doi:10.1097/01.mat.0000180353.12963.f2

[48] Smith, C. R. (2020). Introduction to Graduate Fluid Mechanics (3rd ed.).

[49] Potters, W. V., van Ooij, P., Marquering, H., vanBavel, E., & Nederveen, A. J. (2014). Volumetric arterial Wall shear stress calculation based on cine phase contrast MRI. Journal of Magnetic Resonance Imaging, 41(2), 505–516. https://doi.org/10.1002/jmri.24560

[50] Kefayati, S., Milner, J. S., Holdsworth, D. W., & Poepping, T. L. (2014). In vitro shear stress measurements using Particle Image Velocimetry in a family of carotid artery models: Effect of stenosis Severity, Plaque eccentricity, And ulceration. PLoS ONE, 9(7). https://doi.org/10.1371/journal.pone.0098209

[51] Kähler, C. J., Scharnowski, S., & Cierpka, C. (2012). On the uncertainty of digital PIV and PTV Near walls. Experiments in Fluids, 52(6), 1641–1656. https://doi.org/10.1007/s00348-012-1307-3

[52] Petersson, S., Dyverfeldt, P., & Ebbers, T. (2012). Assessment of the accuracy of MRI wall shear stress estimation using numerical simulations. Journal of Magnetic Resonance Imaging, 36(1), 128–138. https://doi.org/10.1002/jmri.23610

[53] Fatemi, R.S., Rittgers, S.E., 1994. Derivation of sheer rates from near-wall LDA measurements under steady and pulsatile flow conditions. Journal of Biomechanical Engineering-Transactions of the Asme 116:361-368.

[54] van Ooij P, Potters WV, Guedon A, Schneiders JJ, Marquering HA, Majoie CB, et al. Wall shear stress estimated with phase contrast MRI in an in vitro and in vivo intracranial aneurysm. J Magn Reson Imaging 2013;38:876–884.

[55] van Ooij, P., Potters, W.V., Nederveen, A.J., et al., 2015. A methodology to detect abnormal relative wall shear stress on the full surface of the thoracic aorta using four-dimensional flow mri. Magnetic Resonance in Medicine 73:1216-1227.

[56] Morbiducci, U., Gallo, D., Massai, D., Consolo, F., Ponzini, R., Antiga, L., Bignardi, C., Deriu, M. A., & Redaelli, A. (2010). Outflow conditions for image-based hemodynamic models of the carotid bifurcation: Implications for indicators of abnormal flow. Journal of Biomechanical Engineering, 132(9). https://doi.org/10.1115/1.4001886

[57] Lei, M., Kleinstreuer, C., Truskey, G.A., 1995. Numerical investigation and prediction of atherogenic sites in branching arteries. Journal of Biomechanical Engineering 117, 350–357.

[58] Ohja, M., 1994. Wall Shear stress temporal gradient and anastomotic intimal hyperplasia. Circulation Research 7, 1227–1231.

[59] Himburg, H.A., Friedman, M.H., 2006. Correspondence of low mean shear and high harmonic content in the porcine iliac arteries. Journal of Biomechanical Engineering 128, 852–856.

[60] Peiffer, V., Sherwin, S. J., & Weinberg, P. D. (2013). Computation in the rabbit aorta of a new metric – the transverse wall shear stress – to quantify the multidirectional character of disturbed blood flow. Journal of Biomechanics, 46(15), 2651–2658. https://doi.org/10.1016/j.jbiomech.2013.08.003

[61] Ku, D.N., Giddens, D.P., Zarins, C.K., Glagov, S., 1985. Pulsatile flow and atherosclerosis in the human carotid bifurcation. Positive correlation between plaque location and low oscillating shear stress. Arteriosclerosis 5, 293–302.

[62] He, X., and Ku, D. N., 1996, "Pulsatile Flow in the Human Left Coronary Artery Bifurcation: Average Conditions," ASME J. Biomech. Eng., 118(1),pp. 74–82.

[63] Giddens, D. P., Zarins, C. K., and Glagov, S., 1993, "The Role of Fluid Mechanics in the Localization and Detection of Atherosclerosis," ASME J. Biomech. Eng., 115(4B), pp. 588–595.

[64] Buchanan, J. R., Kleinstreuer, C., Truskey, G. A., & Lei, M. (1999). Relation between non-uniform hemodynamics and sites of altered permeability and lesion growth at the rabbit aorto-celiac junction. Atherosclerosis, 143(1), 27–40. https://doi.org/10.1016/s0021-9150(98)00264-0

[65] Finol, E. A., & Amon, C. H. (2002). Flow-induced wall shear stress in abdominal aortic aneurysms: Part i - steady flow hemodynamics. Computer Methods in Biomechanics and Biomedical Engineering, 5(4), 309–318. https://doi.org/10.1080/1025584021000009742

[66] Finol, E. A., & Amon, C. H. (2002). Flow-induced wall shear stress in abdominal aortic aneurysms: Part ii - pulsatile flow hemodynamics. Computer Methods in Biomechanics and Biomedical Engineering, 5(4), 319–328. https://doi.org/10.1080/1025584021000009751

[67] Bauer, A., Wegt, S., Bopp, M., Jakirlic, S., Tropea, C., Krafft, A. J., Shokina, N., Hennig, J., Teschner, G., & Egger, H. (2019). Comparison of wall shear stress estimates obtained by laser doppler velocimetry, magnetic resonance imaging and numerical simulations. Experiments in Fluids, 60(7). https://doi.org/10.1007/s00348-019-2758-6

[68] Budwig, R., Slippy, J., Hooper, H., & Elger, D. (1994). Steady flow in abdominal aortic aneurysm models.

[69] Peattie, R. A., Riehle, T. J., & Bluth, E. I. (2004). Pulsatile flow in fusiform models of abdominal aortic aneurysms: flow fields, velocity patterns and flow-induced wall stresses. Journal of Biomechanical Engineering, 126(4), 438–446. https://doi.org/10.1115/1.1784478

[70] Durst F, Müller R, Jovanovic J (2004) Determination of the measuring position in laser-doppler anemometry. Exp Fluids 6(2):105–110. https://doi.org/10.1007/bf001 96460

[71] Rodríguez-López E, Bruce PJ, Buxton OR (2015) A robust post-processing method to determine skin friction in turbulent boundary layers from the velocity profile. Exp Fluids 56(4):68. https://doi.org/10.1007/s0034 8-015-1935-5

[72] Musker A (1979) Explicit expression for the smooth wall velocity distribution in a turbulent boundary layer. AIAA J 17(6):655–657. https://doi.org/10.2514/3.61193

[73] El Khoury GK, Schlatter P, Noorani A, Fischer PF, Brethouwer G, Johansson AV (2013) Direct numerical simulation of turbulent pipe flow at moderately high Reynolds numbers. Flow Turbulence Combust 91(3):475–495

[74] Durst F, Kikura H, Lekakis I, Jovanović J, Ye Q (1996b) Wall shear stress determination from near-wall mean velocity data in turbulent pipe and channel flows. Exp Fluids 20(6):417–428. https://doi.org/10.1007/bf001 89380

[75] Bauer, A., Bopp, M., Jakirlic, S., Tropea, C., Krafft, A. J., Shokina, N., & Hennig, J. (2020). Analysis of the wall shear stress in a generic aneurysm under pulsating and transitional flow conditions. Experiments in Fluids, 61(2). https://doi.org/10.1007/s00348-020-2901-4

[76] Nguyen, T. D., Wells, J. C., & Nguyen, C. V. (2010). Wall shear stress measurement of near-wall flow over inclined and curved boundaries by stereo interfacial particle image velocimetry. International Journal of Heat and Fluid Flow, 31(3), 442–449. https://doi.org/10.1016/j.ijheatfluidflow.2009.12.002

[77] Banerjee, M. K., Ganguly, R., & Datta, A. (2012). Effect of pulsatile flow waveform and Womersley number on the flow in stenosed arterial geometry. ISRN Biomathematics, 2012, 1–17. https://doi.org/10.5402/2012/853056

[78] Munson, B. R., Young, D. F., Okiishi, T. H., & Huebsch, W. W. (2009). Fundamentals of fluid Mechanics (6th ed.). Wiley.

[79] Yu, S. C. M. (2000). Steady and pulsatile flow studies in abdominal aortic aneurysm models using Particle Image Velocimetry. International Journal of Heat and Fluid Flow, 21(1), 74–83. https://doi.org/10.1016/s0142-727x(99)00058-2

[80] Bluestein, D., Niu, L., Schoephoerster, R. T., & Dewanjee, M. K. (1996). Steady flow in an aneurysm model: Correlation between fluid dynamics and blood platelet deposition. Journal of Biomechanical Engineering, 118(3), 280–286. https://doi.org/10.1115/1.2796008

[81] Kelsey, L. J., Powell, J. T., Norman, P. E., Miller, K., & Doyle, B. J. (2017). A comparison of hemodynamic metrics and intraluminal thrombus burden in a common iliac artery aneurysm. International journal for numerical methods in biomedical engineering, 33(5), e2821.

APPENDICES

A. Physiological Contours (10 phases)
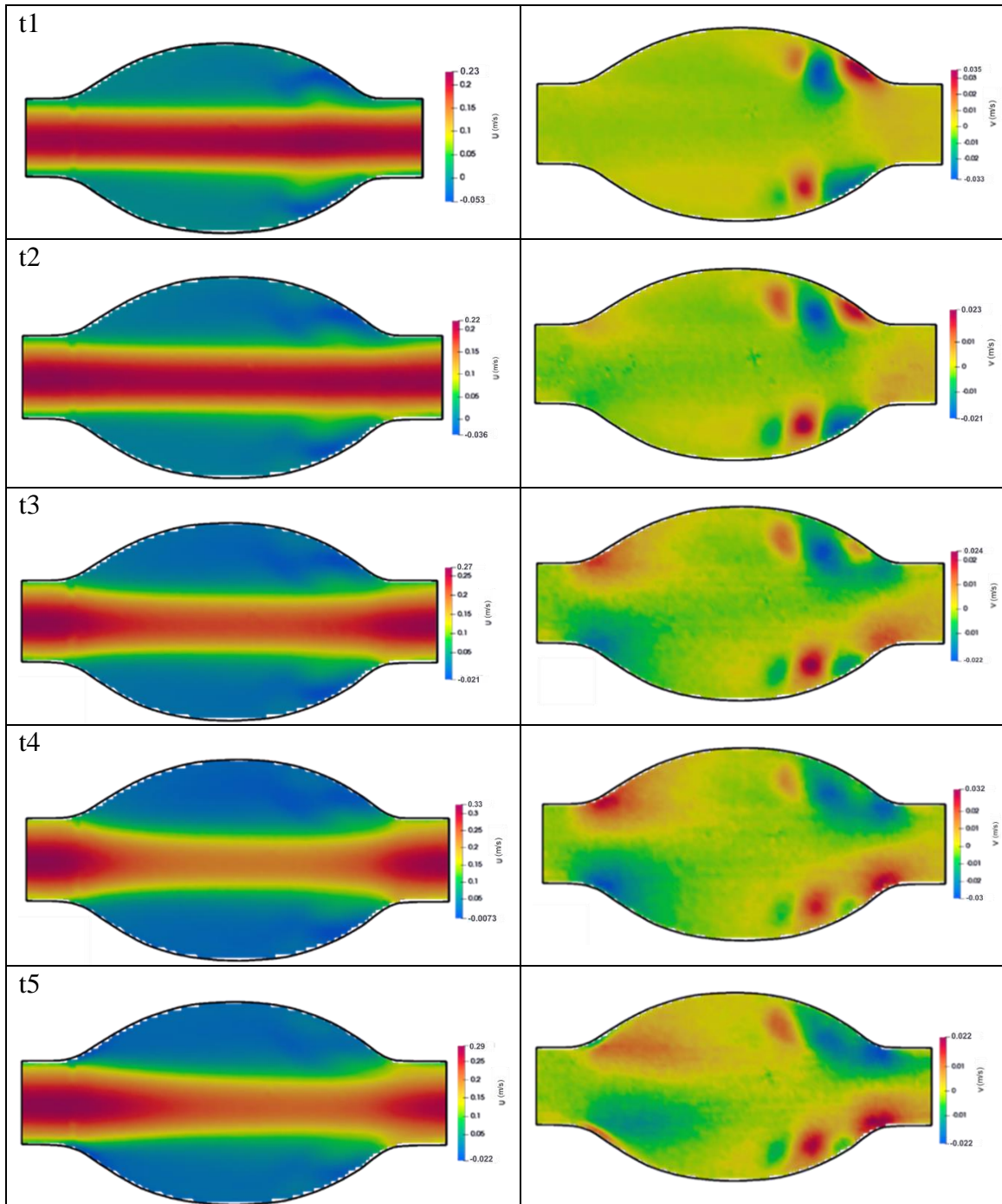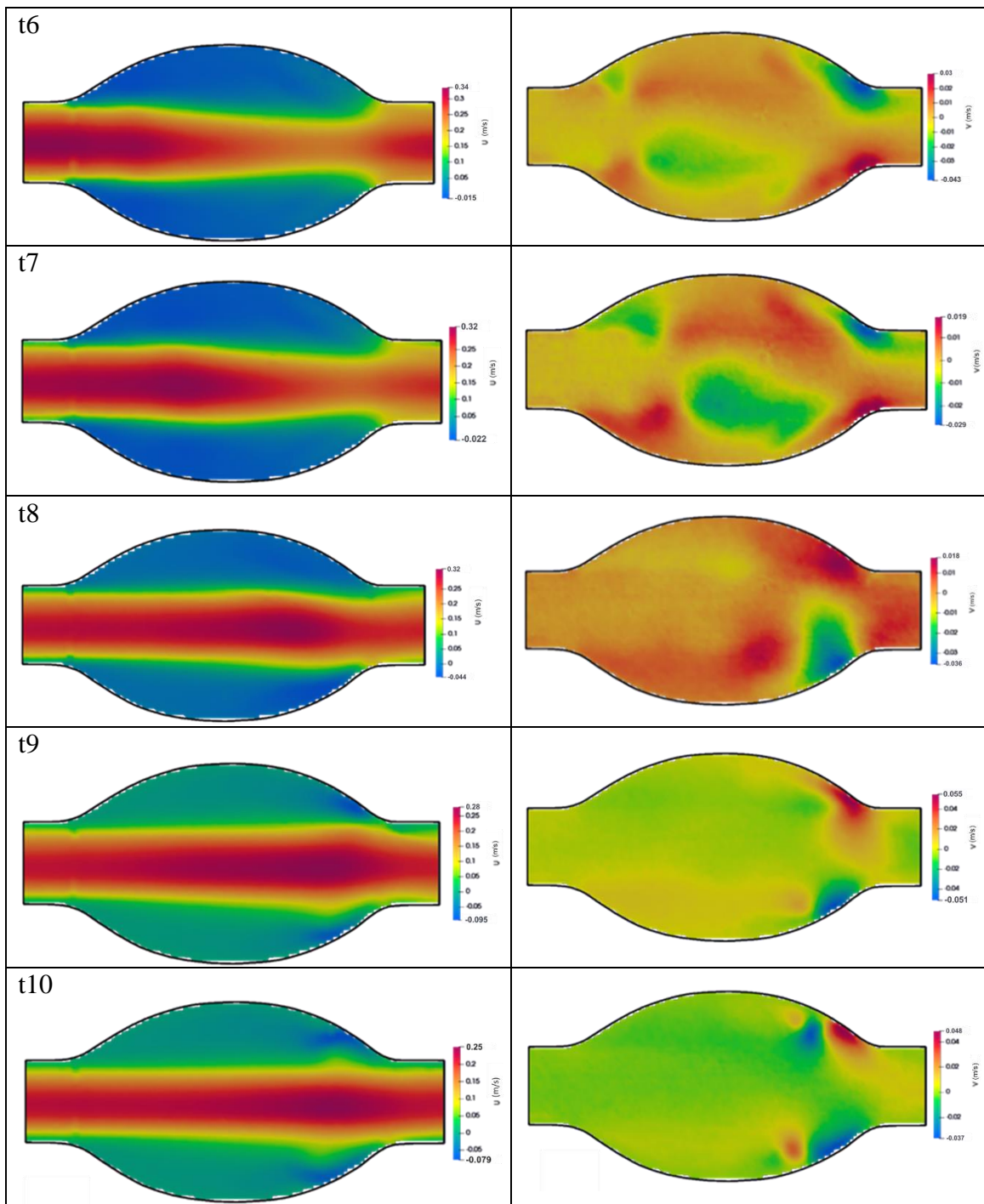
Appendix A. 1: Contours of "u" and "v" for 10 different time increments (Time-varying pattern) / (Above to below: t1 to t10)